Title

Bridging the gap between spectroscopic and magnetic measurements in organocobalt complexes

Permalink

https://escholarship.org/uc/item/0q938708

Author

Mantanona, Alex J

Publication Date

2022

Peer reviewed|Thesis/dissertation

UNIVERSITY OF CALIFORNIA SAN DIEGO

Bridging the gap between spectroscopic and magnetic measurements in organocobalt complexes

A dissertation submitted in partial satisfaction of the
requirements for the degree
Doctor of Philosophy

in
Chemistry
by

Alex Jason Mantanona

Committee in charge:

Professor Jeffrey Rinehart, Chair
Professor Guy Bertrand
Professor Kamil Godula
Professor Olivia Graeve
Professor F. Akif Tezcan

2022

The dissertation of Alex Jason Mantanona is approved, and it is acceptable in quality and form for publication on microfilm and electronically.

University of California San Diego

2022

DEDICATION

To my parents, for their unconditional love and support
To my brother, my partner in crime
And to Nenny, the love of my life

In loving memory of my grandmother
and my friends Chuy and Yvonne.
You will be missed, you will be remembered

EPIGRAPH

“To take a Walk in the Gardens of the Palace of the Tuileries, and describe the statues there, all in marble, in which the ancient Divinities and Heroes are represented with exquisite Art, would be a very pleasant amusement, and instructive entertainment, improving in history, mythology, poetry, as well as in statuary. Another walk in the Gardens of Versailles, would be useful and agreeable. But to observe these objects with taste and describe them so as to be understood, would require more time and thought than I can possibly spare. It is not indeed the fine arts, which our Country requires. The useful, the mechanic arts, are those which we have occasion for in a young Country, as yet simple and not far advanced in Luxury, although perhaps much too far for her Age and Character. I could fill volumes with descriptions of Temples and Palaces, Paintings, Sculptures, Tapestry, Porcelain if I could have time. But I could not do this without neglecting my duty. The science of government it is my duty to study, more than all other sciences; the arts of legislation and administration and negotiation ought to take the place of, indeed exclude, in a manner, all other arts. I must study politics and war, that our sons may have liberty to study mathematics and philosophy. Our sons ought to study mathematics and philosophy, geography, natural history and naval architecture, navigation, commerce, and agriculture in order to give their children a right to study painting, poetry, music, architecture, statuary, tapestry, and porcelain”

John Adams

TABLE OF CONTENTS

LIST OF ABBREVIATIONS

CAAC – cyclic alkyl-amino carbenes

CF – Crystal-field

FIRMS – Far Infrared Magnetospectroscopy

LFT – Ligand-field Theory

MIC – Mesoionic Carbene

MO – Molecular Orbital

NHC – N-heterocyclic carbene

O_h – Octahedral

SMM – Single-Molecule Magnet

SOC – Spin-Orbit Coupling

SQUID – Superconducting Quantum Interference Device

TIP – Temperature Independent Paramagnetism

ZFS – Zero-field splitting

LIST OF FIGURES

LIST OF TABLES

ACKNOWLEDGEMENTS

This is the second time in my life that I have written an acknowledgement section for the culmination of a scientific degree, and I couldn't help but return to that first document and reflect on the difference of circumstances. This section will be more emotional than the one that came before it, and I hope I can express even a fraction of the gratitude I feel for all of the people that have helped me through the years. I will try to make this as comprehensive as possible, and I apologize to anyone I happen to miss in this acknowledgement section.

First and foremost, I want to thank my parents and the confluence of unlikely events that led to their union. Any accomplishment I have ever achieved is the product of their love. With obvious bias, I can say that these are two of the strongest people you could ever meet. My mother is an immigrant from Mexico who, as a child, worked in the fields, escaped her hometown by joining the army, patrolled the Berlin wall before it fell, and spent her post-military career raising two crazy boys while helping people every day as a social worker. It's only fitting that she married someone as amazing as she is. My dad, a man who grew up in poverty on the island of Guam foraging in the jungles and setting up traps to catch seafood at 3 am before school. He escaped poverty through a twenty-year career in the military including a tour in the first Gulf war and during this time of service he met my mom in Germany of all places. After his military service, he spent years using the technical experience he gained in the military working in industry on various electronic components from fiberoptics to fire-safety systems in airplanes, all while showing me and my brother the love only a father can give. He worked up until 2017, when he was diagnosed with cancer after he was in a car accident on the day I proposed to Nenny, and through some incredible chance they caught the cancer early while screening for trauma related to the accident. He has spent a lot of the past few years struggling with the treatments and other health issues, but his strength is palpable, and there has been nothing better than seeing his face light up when playing with his grandsons. He has mostly recovered now, but I can’t help but think how fortunate we are to have him with us still. Any accomplishment of mine is just a reflection of who these two people are. I love you both, and I hope to make you as proud as I am to have you as my parents.

The next person I’d like to acknowledge is my older brother, Robert. We have had our fights like any siblings have, but since we were kids, he has always looked out for me (when he wasn’t eating my food). He has this selfless streak in him that is so damn admirable, always checking in on people, willing to have the tough conversations, making sure to talk through problems and giving advice to those who need it. He felt the call just like our parents and served in an airborne infantry unit with two tours in Afghanistan. Those years weren’t kind to him or his friends. And yet going through the things he has, he still finds a way to be a good person, to empathize and be kind, and most importantly, to be a great father to his own two rambunctious sons. I can’t recall a week where we didn’t speak to each other, and his strength through his struggles has been a fountain of inspiration. The past few years we hit some awful emotional lows and amazing emotional highs, we leaned on each other and got through them. I could not have gotten through this in one piece without him.

To the family of my better half: Robert, Maria, Adriana, Veronica, and Luis, thank you for welcoming me into the family. The moments we have had together, watching the kids play, eating tamales, spending time over the holidays, and many countless moments in between, have been some of the happiest moments in my life. Thank you for enriching my life with your love.

To my nephews and nieces: RJ, Raquel, Aaron, and now little Aurora, you shine so bright with nothing but potential. I can’t wait to see you grow under the sunshine of your parent’s love.

Your tío Alex and tía Nenny will always be there for you, and we will do our best to make the world a better place for you.

The next person to thank is my current advisor, Dr. Jeffrey Rinehart, a kind person with a great heart and a pure unadulterated love of science. He has shown nothing but patience and compassion for his students, and it has been a privilege to watch him grow into his position as a tenured professor. He has been understanding with me as a mentor when I have been stubborn and lazy, was a good sport about our ridiculous pranks and jokes, gave me slack when I needed it, and treated me with fairness and kindness. I learned an incredible amount from him and I'm a better person and scientist for having met him. He also put together a group of great individuals that have enriched my life. Jeremy Hilgar, thank you for teaching me and mentoring me. I've always appreciated your friendship and love of science, even when we butted heads. Yijun Xie and Ben Zhao, thank you for always treating me with respect and helping whenever needed. Kyle Kirkpatrick and Phil Bunting, thank you for always taking time to joke around in and out of lab, may you always find a scooter you can share together. Tara Zand thank you for friendship, kindness, and warmth you brought into the lab. You made us all better by being around you. Angelica Orlova, thank you for being your weird authentic self and bringing a burst of color and life into the lab when it sorely needed it. Max Bernbeck, thank you for being the annoying little brother, my life has been enriched by our friendship. Sorry if I wasn't always patient with you. To our undergrads, Alexandre Vincent, Chang Haeun, Yiyao Jin, Brandon Flores, Lee Elmont, Jonathan Bussing, Hayley Fong, Catherine Arceo, Ningkai Zheng, and Mckenna Kennedy, thank you all for your love of science and for reminding us how to be patient with those that are learning. And lastly, to my three mentees, Sam Cay, Jerry Li, and Zachary Chavez. The three of you started out as mentees and became lifelong friends. We bonded over our love of science and the personal and larger struggles we were going through together, and I'm not sure I would have finished without the three of you around. Thank you for your synthetic help, for giving me purpose, for the laughter we shared together, the frustrations we fought together, and the friendships we formed. I hope I enriched your lives as much as you did mine.

It is now 3 pages deep into this acknowledgment section and I have so many people still to thank, so forgive me for my brevity moving forward. Thank you to my committee members, Guy Bertrand, Akif Tezcan, Kamil Godula, and Olivia Grave for their mentorship and help navigating this journey. Thank you to Stacey Brydges for her incredible mentorship and guidance in both pedagogy and life. Thank you to Joshua Figueroa for convincing me to attend UCSD and fighting for me to receive scholarships. Thank you to the X-Ray Crystallography Facility and its members Milan Gembicky, Curtis Moore, Jake Bailey, Han Nguyen, and Arnie Rheingold, who have put together a world-class operation that made so much of my research possible. Thank you to Anthony Mrse for assisting in all NMR endeavors. I would not have been able to get to this point without the support of my first PI, Simon Garrett, as well as my co-advisor, Yann Schrodi. Thank you both for getting me into chemistry and allowing me to explore the intricacies of the universe.

Next, to our collaborators and those that helped me along the way. Thank you to the Bertrand group, in particular Rodolphe Jazzar, Jesse Peltier, and Daniel Tolentino. Much of this research would not have been possible without them. Dan has been my best friend the past five years, and it was amazing collaborating on science, playing video games, binging Marvel shows, and getting through life together, he has been an irreplaceable presence in our lives. To Alina Schimpf and the Schimpf group, Alec Rachkov, Jessica Geissenhoff, Hankyeol Jung, Asel Karunaratne, Mike Turo, Bruce Thmopson, Haley Palm, Khin San, Carl Lemmon, Liana Alves, and Linfeng Chen, thank you all for the wonderful memories of our joint group parties and the help on spectroscopy. Next I’d like to thank the Figueroa Lab for always being willing to help on synthetic issues or reagent scarcity and are generally just a bunch of good friends: Krista Balto, Ritchie Hernandez, Myles Drance, Michael Neville, Alejandre Arroyave, Adam Grippo, Joanne Chan, thanks for everything. To the Cohen lab, particularly Joey Palomba, Jessie Moreton, Sergio Ayala, Conor O’Herin, Alysia Kohlbrand, Cy Credille, and Michael Denny, thank you for all of the assistance in measurements and sharing the lab space with us and putting up with our loud music. Thanks also to Dr. Mykhalo Ozerov, our collaborator in the National Magnet Lab who assisted on all FIRMS data.

Thank you to my fellow officers of ChemPAL, Christian Seitz, Madison Edwards, Austen Michalak, Matthew Du, Conor O’Herin, and Liana Alves. We may have been derailed by Covid, but I’d like to think we did some good along the way. Thank you for picking up the slack when I couldn’t keep up anymore.

Thank you to the Sloan Foundation and everyone in the graduate division that provided me with so much support. Sinai Cota, Shana Slebioda, and April Bjornsen, thank you for trying to make something special for our fellows. I also have to thank the extended staff of the Chem Department: Steve George, Rick Thomas, Doug Starkey, Randy Phair, Jeff Rances, Jeanine Kolinko, Amy Tran, Erica Lennard, Kristen Itahara, Asmaa Khatib, Robyn Swanland, Sofia Clemente, Thomas Joyce, and Aaron Watkins. You keep everything running so well and help so many graduate students. Thank you for your help. I’d also like to thank the Teaching and Learning Commons, with particular thanks to Erilynn Heinrichson for helping me become a better instructor and mentor.

Lastly, I need to thank my wife, Yunnuen Oliveros. “There’s no combination of words I could put on the back of the postcard, no song that I could sing, but I can try for your heart.” We’re always better together, Nenny. I love you more and more every single day. We have gone through so much these past few years, and even in our darkest days, we kept each other afloat. Your strength, your happiness, your fieriness, your sweetness, everything about you shines so strongly. Every morning I wake up to the field of sunflowers that is your smile, and as I write this on the 9th anniversary of our first date, I see how lucky I am to have you. Thank you for continuing to go through this journey with me. If I've learned anything outside of chemistry and Dota these past few years, it is that we're going to get through every crest and trough life throws at us, together. I can't wait to see where we will be in another nine, nineteen, and hopefully ninety more years together.

The material in Chapter 2 of this dissertation was adapted from: Mantanona, A.J, Tolentino D.R., Cay, K.S., Gembicky, Jazzar, R., M., Bertrand, G., and Rinehart, J. D "Tuning electronic structure through halide modulation of mesoionic carbene cobalt complexes". *Dalton Trans.,* 2020, 49, 2426-2430. The dissertation author is the primary author of this publication. Reproduced by permission of The Royal Society of Chemistry

The material in Chapter 3 of this dissertation is currently in preparation: Mantanona, A.J, Li, J., Gembicky, M., and Rinehart, J. D "Modeling the molecular magnetism of near-perfect octahedral Co(II) complexes with physically intuitive parameterization". The dissertation author is the primary author of this publication.

VITA

2013	B.S. in Biochemistry, California State University, Northridge
2013-2016	Lab Instructor, California State University, Northridge
2016	M.S. in Chemistry, California State University, Northridge
2016-2022	Teaching Assistant, University of California San Diego
2020	Instructor of Record, Summer Graduate Teaching Scholar, University of California San Diego
2022	Ph.D. in Chemistry, University of California San Diego

PUBLICATIONS

Alex J. Mantanona, Katelyn Wood, Yann Schrodi, and Simon J. Garrett, *Activating Ru Nanoparticles on oxide supports for ring-opening metathesis polymerization*, Dalton Transactions., **2018**, 47, 7754-7760

Alex J. Mantanona, Daniel R. Tolentino, Kristine S. Cay, Milan Gembicky, Rodolphe Jazzar, Guy Bertrand, and Jeffrey D. Rinehart, *Tuning electronic structure through halide modulation of mesoionic carbene cobalt complexes*, Dalton Transactions, **2020**, 49, 2426-2430

Wei Cao, Alex J. Mantanona, Haochuan Mao, Naneki C. McCallum, Yang Jiao, Claudia Battistella, Valeria Caponetti, Nanzhi Zang, Matthew P. Thompson, Marco Montalti, J. Fraser Stoddart, Michael R. Wasielewski, Jeffrey D. Rinehart*, and Nathan C. Gianneschi, *Radical-Enriched Artificial Melanin*, Chemistry of Materials, **2020**, 32, 13, 5759-5767

Wei Cao, Xuhao Zhou, Naneki C. McCallum, Ziying Hu, Qing Zhe Ni, Utkarsh Kapoor, Christian M. Heil, Kristine S. Cay, Tara Zand, Alex J. Mantanona, Arthi Jayaraman, Ali Dhinojwala, Dimitri D. Deheyn, Matthew D. Shawkey, Michael D. Burkart, Jeffrey D. Rinehart, and Nathan C. Giannesch, *Unraveling the Structure and Function of Melanin through Synthesis*, Journal of the American Chemical Society, **2021**, 143, 7, 2622-2637

ABSTRACT OF THE DISSERTATION

Bridging the gap between spectroscopic and magnetic measurements in organocobalt complexes

By

Alex Jason Mantanona

Doctor of Philosophy in Chemistry

University of California San Diego, 2022

Professor Jeffrey Rinehart, Chair

Molecular magnetism is a field highly reliant on understanding the electronic structure of the molecule in question. In *Chapter 1* of this dissertation, we review the connection of state structure to bonding of ligands and review contemporary understanding of energy state manifolds, with a focus on cobalt complexes and transition metals. These complexes are used to demonstrate the growth of the study of molecular magnetism, and we discuss the growth of theory with the

application of spectroscopic and magnetic techniques for their use in probing state structure. In *Chapter 2*, we explore the use of ligand coordination to fine-tune the electronic structure of transition metals and characterize a series of molecules through spectroscopy and magnetometry. This is done by synthesizing the first reported Co(II) and Co(I) mesoionic carbene complexes. In *Chapter 3*, we explore the connection of spectroscopy and magnetometry through the study of highly symmetric octahedral Co(II) complexes and propose a new method of modelling magnetic data in systems with highly complex electronic structures in order to address current problems in modelling systems with complex state structures.

Chapter 1: An introduction of molecular magnetism at the crossroads of symmetry, crystal field approximations, and Ligand Field Theory

1.1 Molecular Magnetism

Magnetic materials have long been a fascinating subject to mankind. From the early days of civilization and our obsession with the magical properties of lodestone, to modern day optimization and tuning of magnetic materials for a variety of technologies, our understanding of one of nature's forces has paralleled our growth as a society, particularly since the dawn of the industrial age. Any discussion of this field inevitably leads to questions of size limitation, as control over magnetism at the smallest level would lead to breakthroughs in a variety of technologies. These lines of thought always boil down to the barrier of classical physics and quantum mechanics and it was this exploration of size limitation that led to the discovery of Mn_{12},[1-2] a molecule that spawned the field of Single-Molecule Magnetism (SMM). No overview of molecular magnetism would be complete without a discussion of this ground-breaking molecule; however, such reviews as introductions are ubiquitous in the field. To avoid this inevitable trope in magnetic literature, we start a few decades earlier on the seminal quantum mechanical descriptions of magnetism, explore the growth and use of symmetry, Crystal Field Theory, and Ligand Field Theory as they pertain to magnetic behavior, and eventually return to the inexorable Mn_{12} cluster at the crossroads of these elegant models to set the stage for the research presented herein.

We start with the basis of magnetic parameterization; the response of a given substance measured in molar magnetization (M), to an external magnetic field (H), is defined as the magnetic susceptibility (χ).[3] In mathematical terms we express this using Equation 1.1:

$$\chi = \frac{\partial M}{\partial H} \tag{1.1}$$

Equation 1 is generalizable for all magnetic measurements; however, there tends to be two limiting regimes of magnetic response when measuring the effects of an external field on the magnetization. This arises from the fact that there are a finite number of spins that can act as a source of magnetic moment and at high field the magnetization can reach saturation as all unpaired electrons in the system orient along the field's axis. This effect usually manifests itself as a curve approaching some limit in a plot of *M* vs *H*. At low enough fields, varying from sample to sample, the magnetization dependence on the field can be written as a linear response, shown in Equation 1.2:

$$M = \chi H \tag{1.2}$$

It is within this region of linearity that the seminal equation, the Curie Law,[3] asserts its influence on the field of magnetism. The Curie Law is directly related to Equation 1.2 and takes the form:

$$\chi = \frac{C}{T} \tag{1.3}$$

This equation was originally proposed before the discovery of quantum mechanics and was originally formulated to act as a descriptor of what we now call Curie paramagnetism. It is used to describe the inverse relationship between temperature and susceptibility with a material-specific constant, *C*. At the time of its formulation the nature of *C* remained unknown; but deviations from Curie paramagnetism, and the advancements in quantum physics, gave hints about the origin of this constant. This relationship has an inherent quantum mechanical origin and can be found in the molar magnetization, a value which arises from the summation of the magnetic responses of each thermally populated state according to a Boltzmann distribution:

$$M = \frac{N\sum_n \left(\frac{-\partial E_n}{\partial H}\right)\exp\left(-\frac{E_n}{KT}\right)}{\sum_n \exp\left(-\frac{E_n}{KT}\right)} \tag{1.4}$$

It is important to note that Equation 1.4 relies on no assumptions other than being a canonical ensemble and that if one can properly calculate each individual state of a system, it can be treated as an analytical solution and also allows us to rationalize the Curie constant.[3] As energy states should be discrete values within any system on the quantized scale, any physical parameter that attempts to model a behavior that is inherently quantum mechanical in nature will be reliant on those discrete states; thus, many systems having simple energy manifolds obey the Curie Law. However, as anyone that has studied anything on the quantum scale already knows, many systems are more complex than simple Curie paramagnets and state calculations are far from trivial. Those who study in the field often use simplifications in order to rationalize and predict magnetic properties. The most notable of these methods is the Van Vleck formula which, given some rearrangement to put into terms of susceptibility, is provided in Equation 1.5:[4]

$$\chi = \frac{N\sum_n \left(\frac{E_n^{(1)2}}{kT} - 2E_n^{(2)}\right) exp\left(\frac{-E_n^{(0)}}{kT}\right)}{\sum_n exp\left(\frac{-E_n^{(0)}}{kT}\right)} \tag{1.5}$$

The Van Vleck Formula relies on the approximations that *H/kT* is small and that the energies can be expanded based on increasing powers of *H*. This approximation is particularly useful as the Van Vleck Formula allows for comparisons of magnetic systems, provided that any measurement performed on a sample's magnetic properties is done in the region of linear response of *M* vs. *H*. This simplification allow us to return to the Curie Law and provide quantification for the Curie constant.[3] In systems without spin-orbit coupling that are magnetically isotropic, meaning there is no directionality in the magnetic moment, energy states scale based on the *g*-factor which is approximately 2, the moment of the electron also known as the Bohr-Procopiu[5-6] magneton (μ_β), and the spin multiplicity of the ground state. This can be expressed mathematically in the simplified form of the Van Vleck formula given in Equation 1.6:

$$\chi = \frac{Ng^2\beta^2}{3kT} S(S+1) \tag{1.6}$$

This expression often acts as the benchmark in framing our understanding of molecular magnetic behavior. As the expression $Ng^2/3k$ in the cgsemu unit system (the most common unit system used in practice in molecular magnetometry) comes out to 0.12505, or approximately 1/8, the susceptibility of a system acts as the easiest way to determine whether a system is acting as a Curie paramagnet. When the temperature dependence is removed from χ by taking the product of susceptibility and temperature we get χT, a parameter that becomes the same value across all temperatures for Curie paramagnets and can be approximated simply with Equation 1.7:

$$\chi_T = \frac{n(n+1)}{8} \tag{1.7}$$

with n being the number of unpaired electrons. This horizontal response acts as the baseline for our studying of molecular magnetism as deviations in χT allow us to determine whether something is behaving in typical Curie fashion or whether there are influences on the energy manifold on the system which may arise from magnetic anisotropy, coupling between spin centers, or other phenomena.

1.2 Magnetic Anisotropy

Deviations in χT from Curie behavior typically become more pronounced as temperature is lowered and the thermal population of states become more pronounced.[3] One of the most common influences leading to deviation in Curie behavior is magnetic anisotropy, which can be generalized as the propensity of the electron density and magnetic moment to favor a direction due to some electromagnetic interaction. The source of anisotropy can be traced to unquenched orbital angular momentum introduced through spin-orbit coupling. The following three conditions must be met in order for an ion to retain its orbital angular momentum and provide anisotropy: (1) degenerate orbitals, (2) the orbitals that are degenerate must be symmetrically related across a main axis rotation so that their linear combination forms a spherical harmonic, and (3) there is space within the orbitals in question for electrons to freely move between these orbitals without violating the Pauli exclusion rule.[7-8] These conditions manifest commonly in both *d*-block and *f*-block elements, but as the focus of this dissertation will be on primarily first row transition-metals, particularly Co(II), we will frame our examples in the context of the 3*d* elements.

Transition metals have 2 pairs of orbitals that can meet the above criteria as shown in Figure 1A.[7, 9] These sets correspond with the orbitals that can be linearly combined to form spherical harmonics, in this case the m_l = ± 1 and ± 2 orbitals, i.e. the d_{xz}/d_{yz} and $d_{xy}/d_{x^2-y^2}$ orbitals. Any transition metal complex that forms degenerate sets containing these orbitals has the potential to generate magnetic anisotropy, provided that the electron filling is conducive to such a pathway. For example, as shown in Figure 1B, a d^4 ion in an octahedral environment can generate orbital angular momentum in the low-spin state as the electron freely passes between degenerate orbitals that contain the d_{xz}/d_{yz} pair. In the high-spin state, the only electron capable of moving between degenerate orbitals belongs to the e_g set. As this pair of orbitals cannot be combined into a spherical

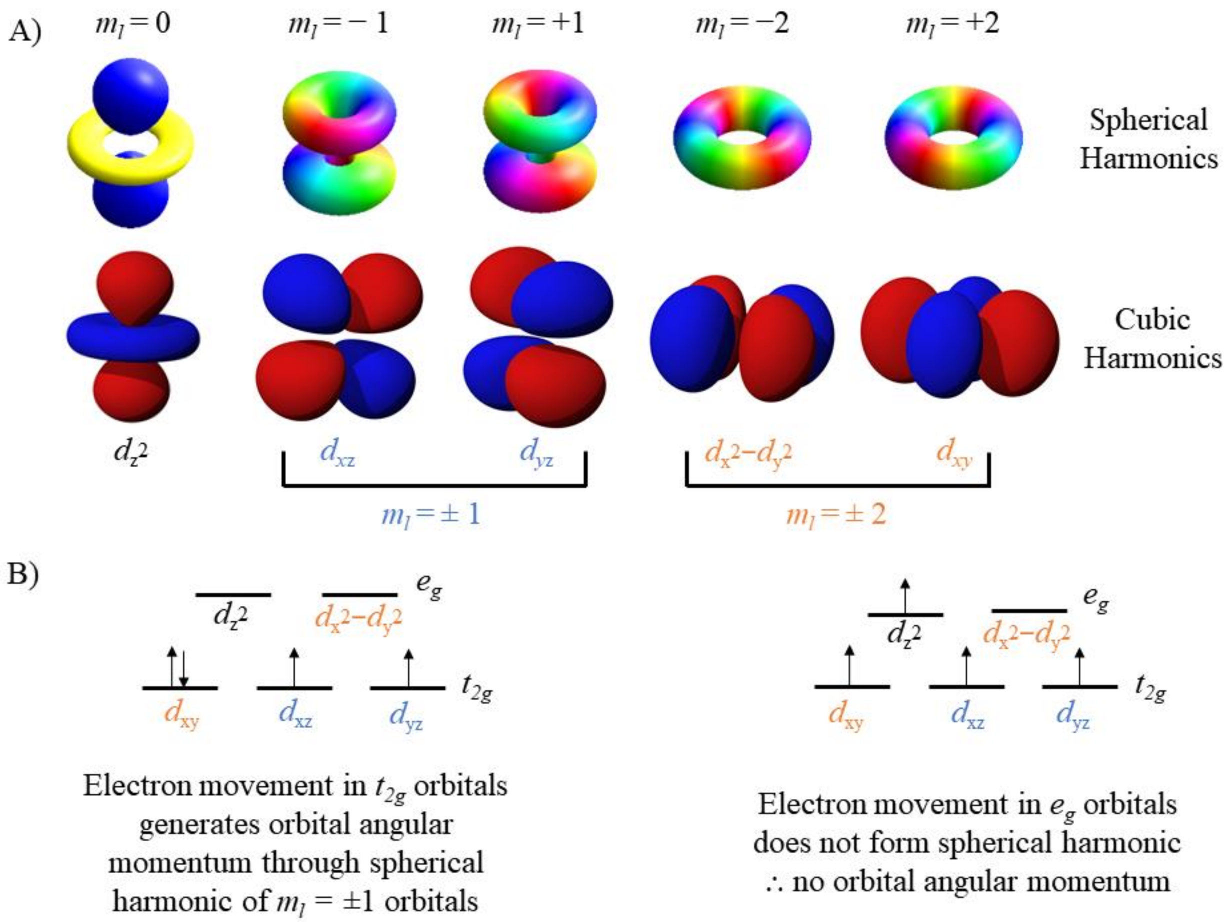

Figure 1: A) Spherical and cubic harmonics of the 3*d* orbitals. Color depicts phase of the eigenfunction. 1B) Two examples of d^4 orbital splitting in an octahedral environment showing a system with first order orbital angular momentum (left) and without (right).

harmonic with orbital angular momentum, anisotropy will not be generated through this electron configuration nor through any that don't meet the requirements above.

The specific mechanism of magnetic anisotropy is also highly dependent on the system that is being studied and the generation of orbital angular momentum is not restricted to the ground state. In fact, it is somewhat rare for transition metals to generate anisotropy in such a manner as ligand-field effects can lift the degeneracy of orbitals in the absence of strict symmetry. Another source of anisotropy can be found in a paramagnetic system which lacks spin-orbit coupling within the ground state but is able to mix with excited states that retain their orbital angular momentum.

This mixing with an excited state with orbital angular momentum may lift degeneracies in the ground state of the spin system by creating a preferred directionality of the electron motion i.e., creating magnetic anisotropy.[10] This effect is similar to the splitting of states caused by the Zeeman effect but notably happens in the absence of a magnetic field, shown in Figure 2. This effect is known as Zero Field Splitting or ZFS.

As the effects of ZFS by definition only take place in the absence of orbital angular momentum in the ground state, it is possible to quantify the anisotropy of the system using simple

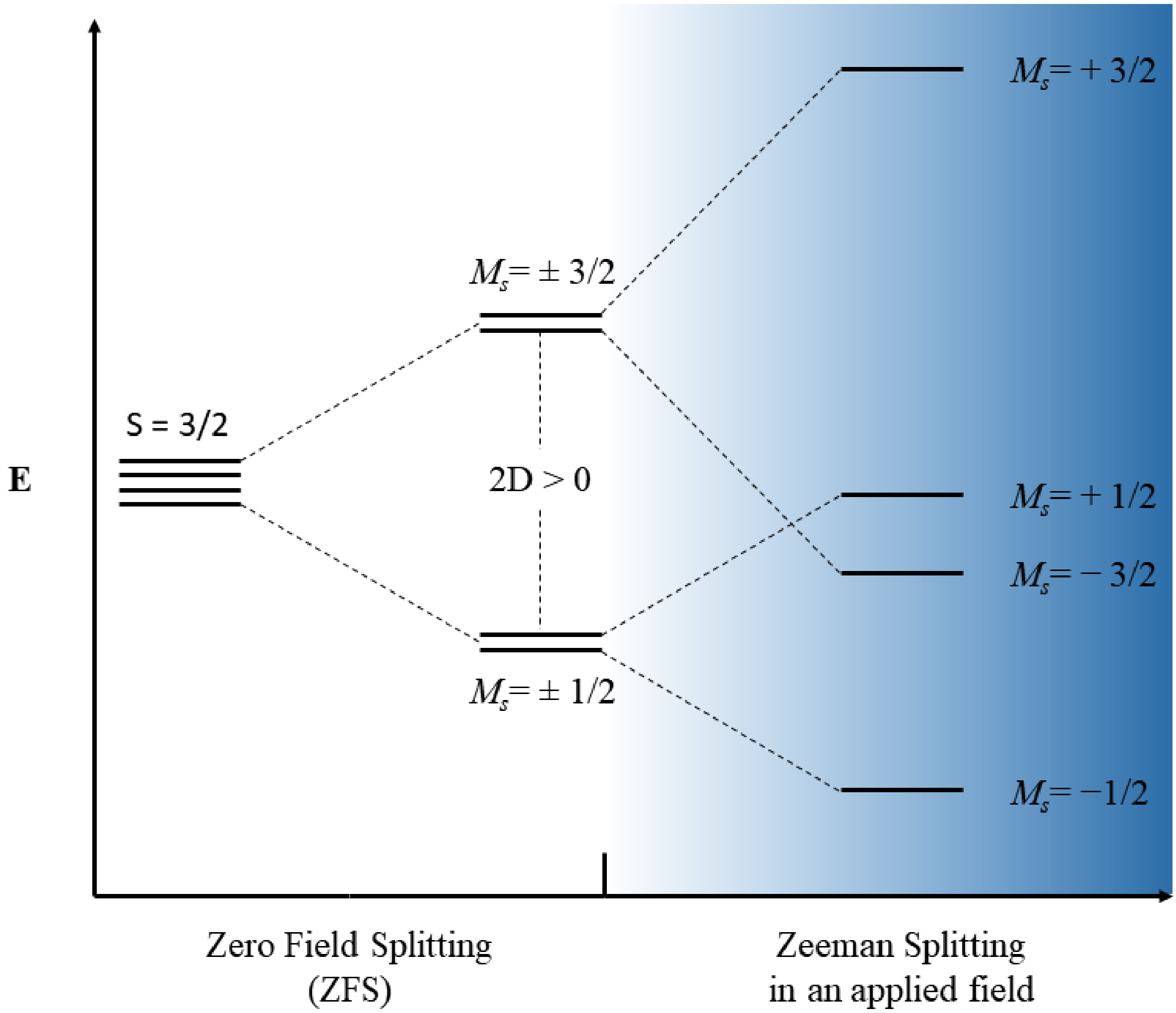

Figure 2: Qualitative look at the M_s states of an S = 3/2 ion showing the effects by Zero Field Splitting as well as Zeeman Splitting in an applied field with blue shading showing field strength

phenomenological spin Hamiltonians.[3] To do so, we introduce the symmetric and traceless tensor, **D**, in Equation 1.8:

$$\widehat{\mathrm{H}}_{ZFS} = \mathbf{S} \cdot \mathbf{D} \cdot \mathbf{S} \tag{1.8}$$

Use of this Hamiltonian has become ubiquitous in the field of molecular magnetism, and it is the most common way of parameterizing transition metal magnetism. It gives a model that easily reconstructs magnetic data by simplifying the anisotropy generated through state mixing into a term that quantifies the splitting in M_s states. As the **D**-tensor has nine components in the form D_{uu} (u = x, y, z) whose experimental determination is no trivial task, the Hamiltonian is often further restricted in terms of the axial component, also known as the easy-axis of magnetization along the z axis, shown in Equation 1.9:[10]

$$\widehat{\mathrm{H}} = D\mathrm{S}_{\mathrm{z}}^{2} \tag{1.9}$$

Positive D values typically correspond to the lower moment states being the ground state as shown in Figure 2, and negative D values are typically indicative of the opposite. D values are usually small energy values, and we will report all values in this manuscript using wavenumbers (cm^{-1}) as our unit of choice. This parameter can be thought of as a measurement of the magnetic anisotropy of the system. Although there are deeper explorations of the math behind this tensor and other parameters that we can use to quantify the non-axial components, for simplicity's sake we will leave them for discussions in other pieces of literature.[10]

1.3 The Evolution of Crystal-Field Approximations into Ligand-Field Theory

Parameterizing the energy manifold and state splittings of paramagnetic systems to quantify the anisotropy has been a continuous challenge in the field.[11] One of the most popular methods to approach this problem has been through the application of the crystal-field (CF) potential and its successor, Ligand-Field Theory (LFT).[12] The CF method simplifies metal-ligand bonding into interactions of point charges using spherical harmonics under the assumption that any ion bound feels its surroundings in the form of a one-electron potential. There have been many approaches at modelling predictive crystal-field parameters including the Superposition,[13] Angular Overlap,[14-15] and Point Charge Models;[16] however, each of these models have issues in their generalizability as the CF potential does not adequately account for interactions such as covalency, polarizability, or mixing of orbitals and states.

With that being said, CF parameters can still be successfully used as a perturbation in effective Hamiltonians allowing for quantification of state-splitting.[17] In this manuscript we will refer to two parameterization schemes starting with the most widely-used, the Wybourne notation,[18] given in Equation 1.10:

$$\hat{H}_{CF} = \sum_{i}\sum_{k,q} B_{kq}\hat{C}_q^{(k)}\left(\nu_{i,}\varphi_i\right) \tag{1.10}$$

with

$$\hat{C}_q^{(k)} = \left(\frac{4\pi}{2k+1}\right)^{\frac{1}{2}}\hat{Y}_q^{(k)} \tag{1.11}$$

In Wybourne notation, B_{kq} are the Wybourne CF parameters, i covers all unpaired electrons in the valence shell, k and q cover all spherical harmonic components allowed by symmetry, and $\hat{C}_q^{(k)}$ are the spherical harmonic operators in the form given in Equation 1.11. The operators consist of twenty-seven terms of spherical harmonics which are used to describe the environment of an ion, but the number of terms may be reduced due to the spatial and time inversion symmetry operations of the ion. For 3*d* ions in axial symmetry (such as the octahedral complexes discussed in this dissertation), the terms can be limited to the cubic terms (B_{20}, B_{40}) and the terms that express non-cubic deviations (B_{44} for tetragonal distortions and B_{43} for trigonal distortions). Wybourne notation is commonly used in spectroscopy and is often used in tandem with Ligand-Field Theory, which we will be discussing later in this section.

The other class of parameterization to review is the Stevens method, which differs slightly from Wybourne notation in the use of operator equivalents, $\hat{O}_k^{(q)}$, for tesseral harmonics rather than the generalized spherical harmonics of Wybourne notation and the radial components included in the $A_k^q \langle r^k \rangle_i$ term.[19] Stevens notation is widely used in computational approaches as tables of matrix elements are widely available[20] and many fitting programs[17] take advantage of their relatively simple mathematical implementation. The Stevens notation in the operator equivalent form are expressed in Equation 1.12 in terms of total angular momentum:

$$\hat{H}_{CF} = \sum_{k\,,q} A_k^q \langle r^k \rangle_i \hat{O}_k^{(q)} \left(\hat{J}_z\,, \hat{J}_\pm \right) \tag{1.12}$$

The Stevens CF parameters are often written in a “B” notation such that $B_k^q = A_k^q \langle r^k \rangle_i$. These parameters can be easily related to Wybourne notation through ratios given in Table 1).[12] Similar to Wybourne notation, k values cover all harmonic oscillators allowed by symmetry but are restricted to even values of k due to the necessity of time-invariance symmetry in the use of the operator equivalents.[12] For most cases, k can be limited to ranks 2, 4, and 6.

Table 1: Ratio of CF parameters of Wybourne notation (B_{kq}) and Stevens notation ($B_k^q = A_k^q \langle r^k \rangle_i$)

k	q	B_{kq}/B_k^q
2	0	2
2	1	$-\sqrt{6}/6$
2	2	$\sqrt{6}/3$
4	0	8
4	1	$-2\sqrt{5}/5$
4	2	$2\sqrt{10}/5$
4	3	$-2\sqrt{35}/35$
4	4	$4\sqrt{70}/35$
6	0	16
6	1	$-4\sqrt{42}/21$
6	2	$16\sqrt{105}/105$
6	3	$-8\sqrt{105}/105$
6	4	$8\sqrt{14}/21$
6	5	$-8\sqrt{77}/231$
6	6	$16\sqrt{231}/231$

The Stevens operator equivalents ($\hat{O}_k^{(q)}$) to the spherical harmonic operators of Wybourne notation ($\hat{C}_k^{(q)}$) offer the distinct advantage of being able to act directly on many-electron states.[12] This advantage stems from the fact that Stevens operator equivalents directly act on the total angular momentum, J (or L), and can be scaled to the spherical harmonics of Wybourne through proportionality factors, θ_k, through the use of the Wigner-Eckart theorem.[21] The operator equivalents can be found in Appendix A.

Combining the change of notation with the operator equivalent method and the proportionality factors gives us our Hamiltonian of choice for modelling CF parameters in this manuscript, Equation 1.13:

$$\hat{H}_{CF} = \sum_{i=1}^{N} \sum_{k=2,4,6} \sum_{q=-k}^{k} \sigma_i^k B_{ki}^q \theta_k \hat{O}_{ki}^q \qquad (1.13)$$

Three of the four terms of this Hamiltonian have already been discussed above, leaving only one term left that needs clarification. The σ term of Equation 1.13 is the orbital reduction factor and is composed of the product of two individual parameters, κ and *A*.[22] The κ parameter is an empirical term that acts as a correction for shifts in orbital moment caused by covalency and loss of symmetry and has a range from 0 to 1, with smaller values accounting for greater covalency and distortions and larger values indicating less covalency or distortions in the bonding scheme. The *A* parameter is a term that accounts for state mixing through symmetry and ranges from 1 to 1.5, with a value of 1 indicating a strong ligand-field causing less mixing as states are split far from each other, and a value of 1.5 indicating a weak ligand-field allowing for more mixing of states leading to an increase in orbital moment.

The definition of the orbital reduction factor relies heavily on understanding what constitutes a strong or weak ligand-field and can serve as our springboard to discuss this key concept which is a staple in many branches of modern-day inorganic chemistry. The evolution of the ligand-field developed out of a necessity to give physical meaning to CF parameters.[11] Although the groundwork for LFT was laid using group theory by Bethe in 1929,[23] LFT's origin in molecular magnetism truly began with Linus Pauling's series on "The nature of the chemical bond."[24] Throughout these papers Pauling attempted to dissociate paramagnetism from the crystal-field theory that had been proposed by Van Vleck,[25] Penney,[26] and Schlapp[27]; however, Van Vleck ended up building upon Pauling's work and combined it with Mulliken's molecular orbital (MO) theory[28] to give the LFT foundation that we still use to this day.[29] Contemporary LFT asserts that the splitting of orbital energies can be qualitatively determined through the use of symmetry. The most well-known and widely taught application of LFT is the study of octahedral transition metal complexes, a topic which happens to coincide with one of the main points of study in this dissertation. It is in the framework of octahedral complexes where we begin our exploration of LFT.

Let us consider Co(II), a d^7 ion. In the absence of bonded ligands, the free-ion *d* orbital energies are degenerate as shown on the left side of Figure 3.[22, 30] Once ligation occurs, the orbital energies split based on the symmetry of coordination. The relative energies of orbitals rise or fall based on the electron repulsion that occurs due to the overlap with bonding axes. In octahedral (O_h) symmetry, this leads to two sets of *d* orbitals: the lower energy t_{2g} set, which is comprised of the d_{xy}, d_{xz}, and d_{yz} orbitals that have no direct overlap with the bonding axes, and the higher energy e_g set, comprised of the $d_{x^2-y^2}$ and d_{z^2} orbitals, located along the bonding axes. The splitting of these sets of orbitals in O_h symmetry is often denoted as Δ_O and is referred to as the crystal-field

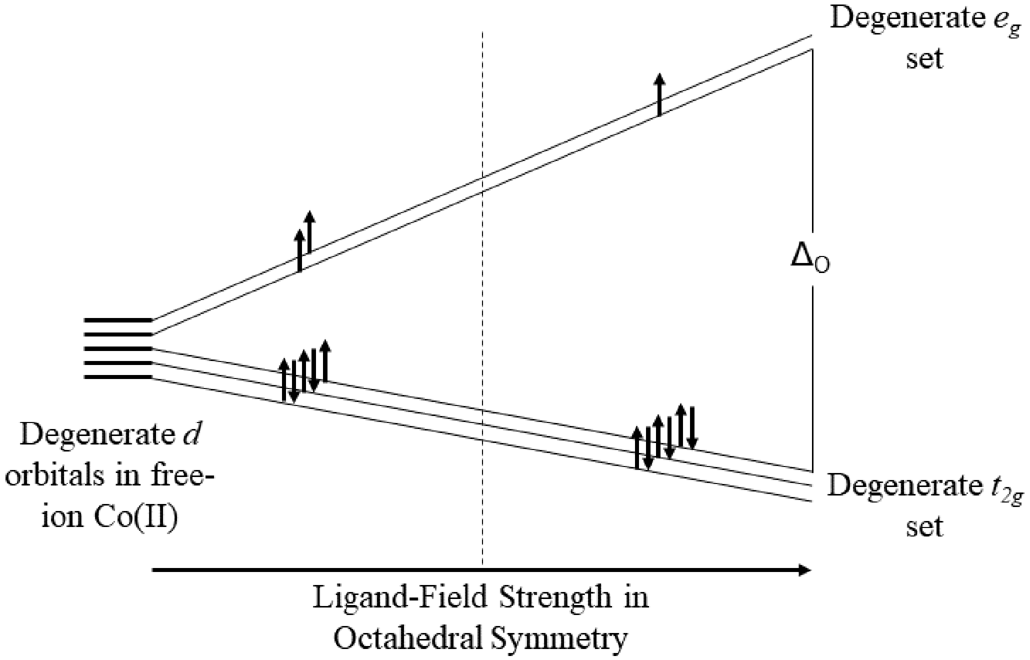

Figure 3: Splitting of *d* orbitals in octahedral symmetry for Co(II). The dashed line indicates the energy threshold where pairing energy is less than the splitting energy, Δ_O.

splitting. Once Δ_O reaches a larger enough energy threshold, the filling of *d* orbitals changes as it becomes more energetically favorable to pair electrons rather than fill the higher energy orbitals.

The concept of Δ_O is the watershed which separated CF approximations into LFT.[30] It was Van Vleck's study[29] of this splitting which revealed one of the key weaknesses of CF approximations: considering ligands as strictly electrostatic potentials fails in predicting the splitting caused by Δ_O. Van Vleck chose to treat this splitting strictly as a semi-empirical parameter of the system and realized the value wasn't determined solely by the electrostatic potential.[30] Over time, the definition of Δ_O evolved to incorporate four contributions: (1) the electrostatic effect, (2) σ donation from ligands to the metal center, (3) π donation from ligands to the metal center, and (4) π backbonding from metal to ligand. In short, stronger electrostatic interactions, stronger σ donation, and stronger π back-bonding leads to larger Δ_O values, while weaker electrostatic interactions and stronger π-donation leads to smaller values. The CF gets a nod in the nomenclature of LFT, as ligands that create large Δ_O values are called strong-field ligands and weak-field ligands produce smaller Δ_O values.

Quantifying Δ_O is usually done by spectroscopic means and is oft defined in terms of the differential of quanta number, *Dq*, with Δ_O equaling 10*Dq*.[31] This relationship only holds true for d^1 ions in the weak-field limit. For transition metal complexes that have more than one electron in their *d* orbitals, the interelectron repulsion must be accounted for. This is done with the Racah parameters, A, B, and C, parameters that are linear combinations of radial repulsion functions, F^k, defined by Condon and Shortley.[32-33] These parameters are presented in Equations 1.14 – 1.16:

$$A = F^0 - \frac{1}{9}F^4 \tag{1.14}$$

$$B = \frac{1}{49}F^2 - \frac{5}{441}F^4 \tag{1.15}$$

$$C = \frac{5}{63}F^4 \tag{1.16}$$

The three parameters above can be condensed into expressions of *B*, as the *A* variable can be set to zero as much of its effect is already accounted for in free-ion approximations, and *C* can be approximated as 4.633 *B*.[34]

With the electron repulsion parameterized with *B*, we are able to correlate spectroscopic measurements with energy splittings. This is done with the use of Tanabe-Sugano diagrams by measuring excitation energies.[35] A Tanabe-Sugano diagram plots the predicted energies of different states of an ion in a plot of Energy/*B* **vs** *Dq*/*B*, as seen in Figure 4 for a d^7 ion.[36] Provided

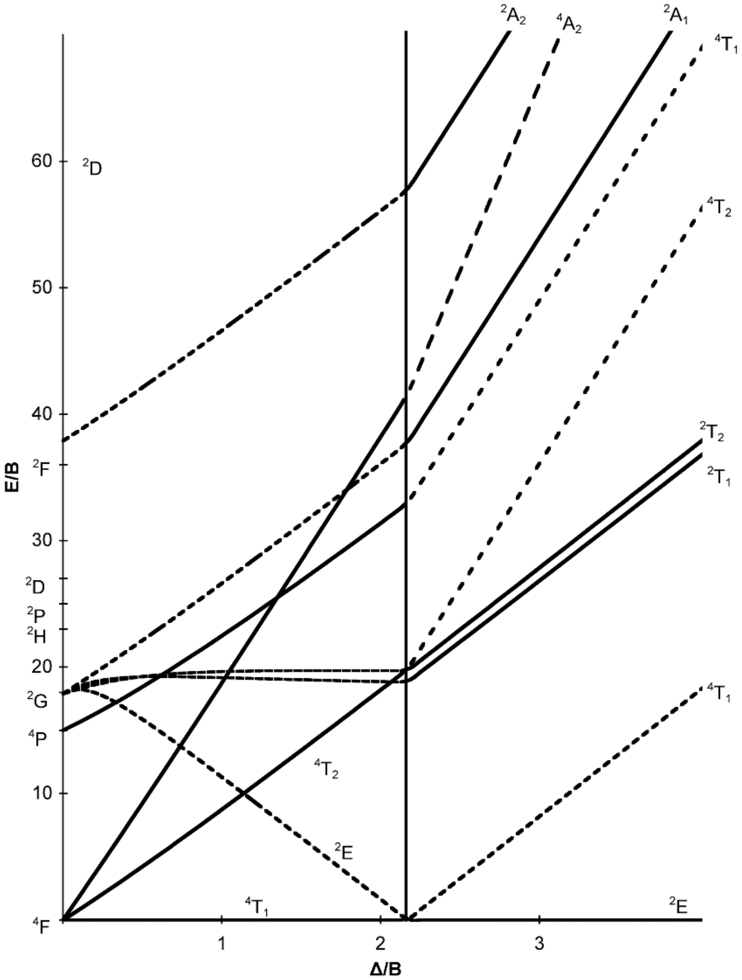

Figure 4: Tanabe-Sugano diagram of a d_7 ion

that you can measure more than one energy excitation, ratios between excitations can be used to approximate the values of *Dq* and *B*.

There are many states calculated and plotted on the Tanabe-Sugano diagram, only some of which are spin-allowed, dictating their relative intensities via standard absorption spectroscopy measurement techniques. For Co(II), the ground state of the free-ion is ^{4}F (using the $^{2S+1}$L formalism) with the first allowed excited state being ^{4}P, as shown on the left side of Figure 5 and in the Tanabe-Sugano diagram above.[22] As discussed, coordinating ligands in an octahedral geometry splits the energy levels of the ground state based on the splitting of the d orbitals. This leads to four quartet states, given here from lowest energy to greatest in the octahedral state (free-ion state) notation: $^4T_{1g}(^4F)$, $^4T_{2g}(^4F)$, $^4A_{2g}(^4F)$, and $^4T_{1g}(^4P)$. The transition $^4T_{1g}(^4F) \rightarrow {}^4T_{2g}(^4F)$ is

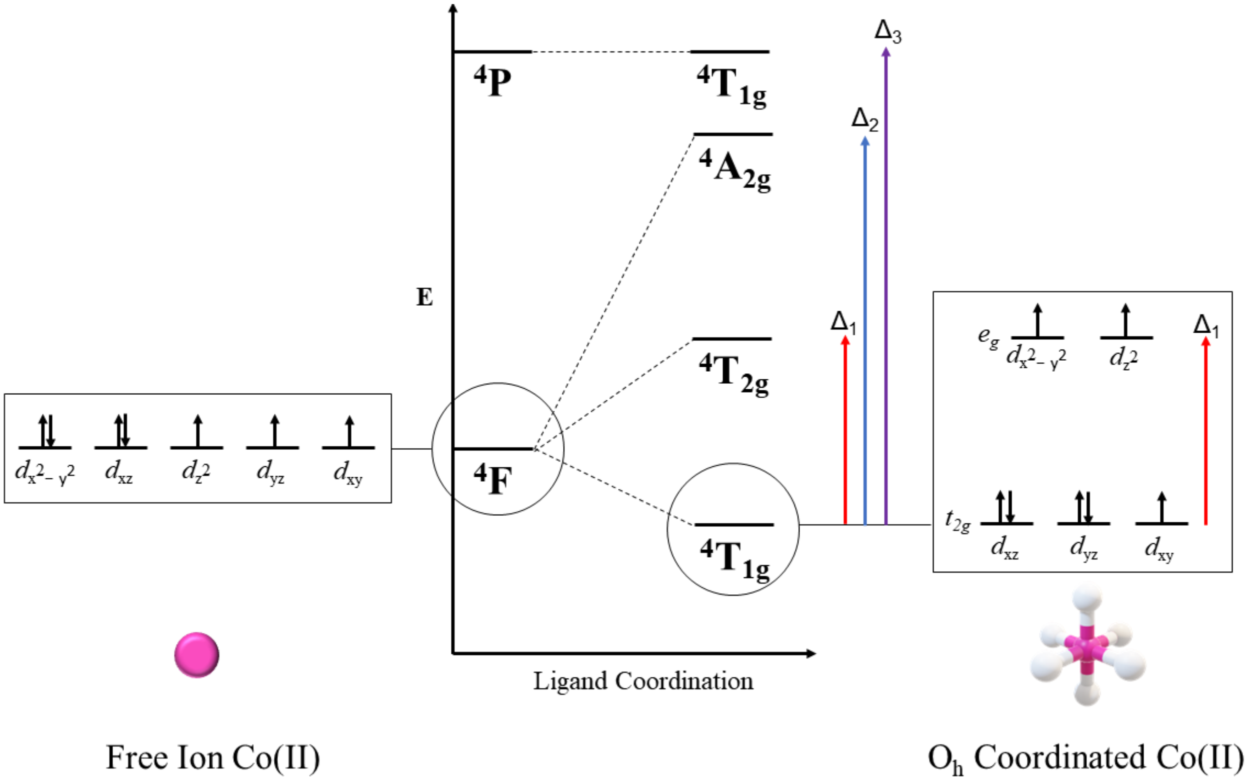

Figure 5: State diagram of Co(II) with free-ion states and *d* orbital splitting on the left with state and orbital splittings caused by octahedral coordination shown on the right. Energy splittings between octahedral states are labeled $\Delta_{1\text{-}3}$ and are defined as electronic excitations. Ligands are presumed to be weak-field.

the first spin-allowed transition (labeled Δ_1 in Figure 5). This excitation is equivalent to $\Delta_{O,}$ and it corresponds to the one-electron excitation from the t_{2g} set to the e_g set. Similar logic can be applied to the other transitions, $^4T_{1g}(^4F) \rightarrow {}^4A_{2g}(^4F)$ and $^4T_{1g}(^4F) \rightarrow {}^4T_{1g}(^4P)$, labeled Δ_2 and Δ_3 respectively. Setting the relative ground state energy of $^4T_{1g}(^4F)$ as 0, the transitions can be approximated in terms of *Dq* and *B* using Equations 1.17-1.20:[22]

$$\Delta_1 = 5\,Dq - 7.5\,B + \frac{1}{2}Q \tag{1.17}$$

$$\Delta_2 = 15\,Dq - 7.5\,B + \frac{1}{2}Q \tag{1.18}$$

$$\Delta_3 = Q \tag{1.19}$$

with

$$Q = (225B^2 + 100Dq^2 + 180DqB)^{\frac{1}{2}} \tag{1.20}$$

These spectroscopic parameters, treated through the lens of LFT, can give physical meaning to CF parameters in more predictive ways than when treated as purely electrostatic potentials. This semi-empirical accounting of covalency in MOs through *Dq* and *B* has led many researchers to quantify their relationship to CF parameters.[37-43] For 3d transition metals in octahedral symmetry, the only term required to model the coordinated ligands is B_{40} in perfect cubic symmetry, with the inclusion of B_{20} and B_{43} or B_{44} (in cases with trigonal or tetragonal distortions respectively).[44] Using the notation developed by Griffith, Morrison, and Ballhausen the perfectly cubic portion of CF parameters can be related to *Dq* with Equations 1.21-1.24:[38, 40, 43]

$$B_{20} = 0 \tag{1.21}$$

$$B_{40} = 21Dq \tag{1.22}$$

$$B_{43} = -2\sqrt{70}Dq \tag{1.23}$$

$$B_{44} = 21\sqrt{\frac{5}{14}}Dq \tag{1.24}$$

Non-cubic portions of these terms from tetragonal and trigonal distortions have been parameterized by Ballhausen. In his formalism he parameterizes the deviations using *Dq*, *Dσ*, and *Dτ* for trigonal symmetry and *Dq*, *Ds*, and *Dt* for tetragonal symmetry.[40] The trigonal terms are defined using Equations 1.25-1.28 and the tetragonal terms are defined with Equations 1.29-1.32:

$$\langle t_{2g}^{\pm}|V_{trig}|t_{2g}^{\pm}\rangle = D\sigma + \frac{2}{3}D\tau \tag{1.25}$$

$$\langle t_{2g}^{0}|V_{trig}|t_{2g}^{0}\rangle = -D\sigma - 6D\tau \tag{1.26}$$

$$\langle t_{2g}^{\pm}|V_{trig}|e_{g}^{\pm}\rangle = \sqrt{2}D\sigma + \frac{5\sqrt{2}}{3}D\tau \tag{1.27}$$

$$\langle e_{2g}^{\pm}|V_{trig}|te_{2g}^{\pm}\rangle = \frac{7}{3}D\sigma \tag{1.28}$$

and

$$\langle d_{x^2-y^2}|V_{tetra}|d_{x^2-y^2}\rangle = 2Ds - 2Dt \tag{1.29}$$

$$\langle d_{z^2}|V_{tetra}|d_{z^2}\rangle = -2Ds - 6Dt \tag{1.30}$$

$$\langle d_{xy}|V_{tetra}|d_{xy}\rangle = 2Ds - Dt \tag{1.31}$$

$$\langle d_{xz}|V_{tetra}|d_{xz}\rangle = -Ds + 4Dt \tag{1.32}$$

With these distortions parameterized, the adjusted conversion factors into Wybourne notation become Equations 1.33-1.35 for trigonal symmetry:

$$B_{20} = -7D\sigma \tag{1.33}$$

$$B_{40} = -14Dq - 21D\tau \tag{1.34}$$

$$B_{43} = -2\sqrt{70}Dq \tag{1.35}$$

and Equations 1.36-1.38 for tetragonal symmetry:

$$B_{20} = -7Ds \tag{1.36}$$

$$B_{40} = 21Dq - 21D\tau \tag{1.34}$$

$$B_{44} = 21\sqrt{\frac{5}{14}}Dq \tag{1.34}$$

Lastly, the CF operators can also be related to the ZFS Hamiltonian, provided that the ion in question does not have any first order angular momentum.[20] This approximation is often used to model magnetic behavior and the relationship is given by:

$$D = 3B_2^0\theta_2 \tag{1.35}$$

1.4 Single-Molecule Magnetism

Let us take a second to review. In Section 1.1, we examined how a Curie paramagnet behaves, and learned that magnetic moment was a result of quantized states with unpaired electrons being thermally populated (Equation 1.4). In Section 1.2, the deviations from Curie paramagnetism as a result of anisotropy were explored, as was the introduction to states being split through perturbation theory. In Section 1.3, we further delved into perturbation theory by reviewing the effects of symmetry in the lens of LFT and parameterized state splittings with CF approximations. With these concepts at hand, we now have most of the tools needed to understand the complete complex electronic structure of a paramagnetic ion. The Hamiltonian to describe the perturbations of a paramagnetic ion's energy manifold is given by Equation 1.36:

$$\widehat{H} = \widehat{H}_{CF} + \widehat{H}_{SOC} + \widehat{H}_{EX} + \widehat{H}_{ZEE} \tag{1.36}$$

This Hamiltonian is composed of the crystal-field approximations (Equation 1.13), spin-orbit coupling, the exchange interaction, and lastly, the Zeeman effect.[17] The CF Hamiltonian can be used to approximate the energy splittings caused by symmetry and can also be used to approximate ZFS contributions when there is no orbital angular momentum through the relationship given in Equation 1.35.

The spin-orbit coupling Hamiltonian for 3d ions is given by:[17]

$$\hat{H}_{SOC} = \sum_{i=1}^{N} \lambda_i \left(\sigma_i \vec{\hat{L}}_i \vec{\hat{S}}_i \right) \tag{1.37}$$

where λ is the spin-orbit coupling constant specific to the ion, σ is the orbital reduction factor discussed in the CF approximations, and $\vec{\hat{L}}_i$ and $\vec{\hat{S}}_i$ are the orbit and spin operators.[3] This term is only used for systems that retain orbital angular momentum, and the orbital reduction factor is used to empirically adjust the amount of splitting caused by SOC in cases where momentum is partially quenched by distortions in geometry. The next term in the full Hamiltonian is given by:

$$\hat{H}_{EX} = -2 \sum_{i \neq j}^{i,j \in N} \left(\vec{S}_i \bar{\bar{J}}_{ij} \vec{\hat{S}}_j \right) \tag{1.38}$$

with *J* being the coupling constant between spin centers which acts as a splitting value of spin-states. This Hamiltonian typically only applies to coupled spin-centers in polynuclear systems. In mononuclear complexes this value can normally be approximated to zero as long-range interactions in the solid-state are very weak. Lastly, the final term in the free-ion Hamiltonian is the Zeeman interaction given by:[3]

$$\hat{H}_{ZEE} = \mu_B \sum_{i=1}^{N} (\sigma \vec{\hat{L}}_i \cdot \bar{\bar{I}} + \vec{\hat{S}}_i \cdot \bar{\bar{g}}_i) \cdot \vec{B} \tag{1.39}$$

where μ_B is the Bohr magneton, $\bar{\bar{I}}$ is the identity matrix of appropriate dimensionality, *g* is the Landé *g*-factor, and $\vec{B}$ is the external magnetic field. The Zeeman effect occurs on any system with magnetic moment and is a function of the field as well as both the spin and orbital moments.

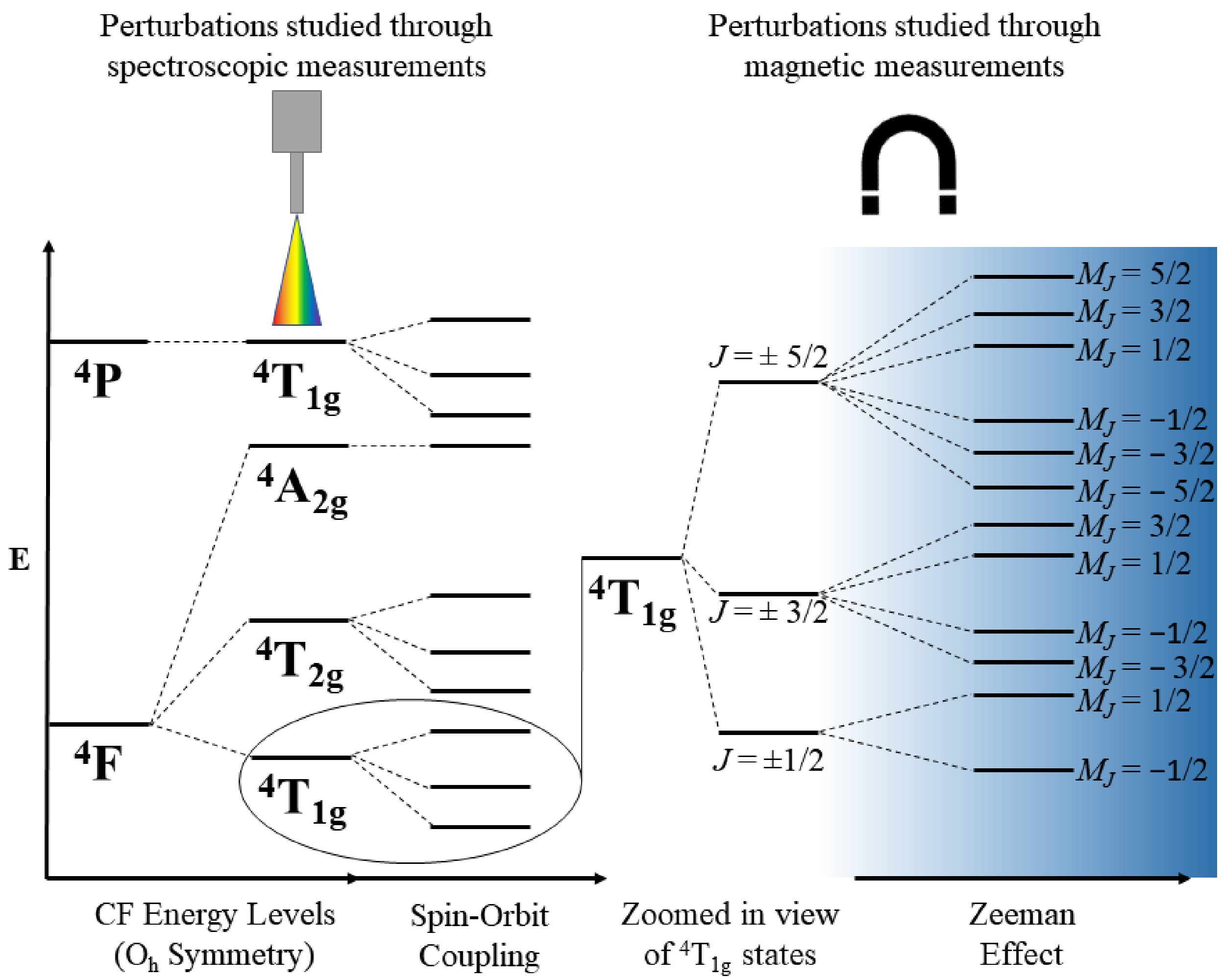

Figure 6: State diagram of a mononuclear octahedral Co(II) ion showing the effects of crystal-field splitting, spin-orbit coupling, with a zoomed in view of the $^4T_{1g}(^4F)$ state to show the Zeeman effect splitting M_J states

These components allow a comprehensive modelling of most magnetic systems by acting as perturbations on the free-ion and this method works whether they are *d*-block or *f*-block, mononuclear or polynuclear. Again, we return to octahedral Co(II) to visualize the effects these perturbations have on a free-ion in Figure 6. As we can see even in our truncated view, the energy manifold of a free-ion can be incredibly complex when under the effect of many perturbations. Even in “simple” systems that do not contain first-order orbital-angular momentum, understanding and measuring this collection of states is no trivial task. Nevertheless, researchers have developed both spectroscopic and magnetic measurements to probe these states.[45-46]

It was the exploration of magnetic states through the use of magnetometers which unearthed an unforeseen effect in certain systems. Studies of nanoparticles showed that there were materials that acted as paramagnets at low temperatures with anomalously large susceptibilities, and more importantly, their magnetic moment could be "blocked" upon the application of an external field for certain amounts of time.[47] This blocking effect would leave remnant magnetic moment upon removal of the field, similar to a ferromagnetic material. Strangely, this remnant magnetization would fade over time and also seemed to have some temperature dependence. This effect would be dubbed superparamagnetism.

With insight of state composition, the mechanism of superparamagnetism could be elucidated.[46-47] Researchers began to posit that this blocked moment may be result of an energy barrier between degenerate magnetic states. Since these nanoparticles were small enough that they were composed of a single magnetic domain acting in concert as a giant-spin, the application of an external field lifted the degeneracy of the ground spin-states through the Zeeman effect. The nanoparticles would then assume the magnetic moment of the lower energy state. Upon removal of the field the degeneracy would be restored, and the nanoparticles would slowly relax to equal populations of the ground magnetic states based on the amount of thermal energy available.[48] Once his behavior became well documented, many began to wonder: was there a size limitation, and was it possible for a well-defined single molecule to exhibit superparamagnetism?

The answer came as an emphatic yes, with the magnetic characterization of a 12-center Mn cluster in 1993, shown in Figure 7. [1-2] This cluster was the first well-defined molecule that exhibited blocking of the magnetization with a time and temperature-dependence, albeit only at

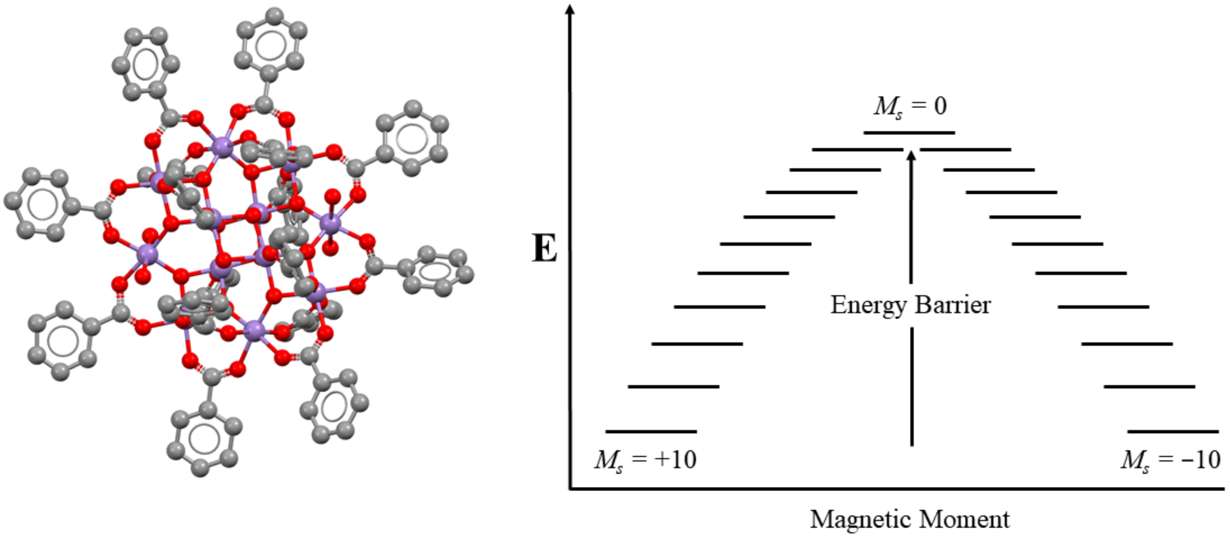

Figure 7: The first characterized single-molecule magnet, colloquially known as the Mn_{12} cluster (left). On the right, a qualitative look at the magnetic states of Mn_{12} providing an energy barrier to relaxation of the magnetic moment

4K. But what was the source of this energy barrier? The researchers determined that due to the lack of symmetry of the ions, the molecule did not retain first order orbital angular momentum. The cluster did, however, have a net ferromagnetic interaction between the ions giving a ground spin-state of $M_s = \pm 10$, and much like the superparamagnetic nanoparticles, this net interaction could be approximated as one "giant" spin as they acted together in unison. This model was proven to be quite effective, and the energy barrier was assigned as the splitting of the degenerate ground M_s state of ±10 (Figure 7 right). This was a succinct explanation of the superparamagnetic behavior of this ion; when a field was applied, the Zeeman effect lifted the degeneracy of the M_s states causing the $M_s = -10$ state to be the most populated (Figure 8). When the field was removed, the barrier blocked the spins from freely relaxing to the degenerate set. As this was based on the model of an effective spin Hamiltonian, the barrier was defined as U_{eff}, and quantification of this barrier relied on the ZFS Hamiltonian by adjusting it for this effective barrier:

$$U_{eff} = DS_z^2 \tag{1.40}$$

Unfortunately, the use of ZFS would cause the initial design principles for the first decade and a half of SMMs to focus on building larger and larger clusters, with the rationale being that the energy barrier would scale exponentially with increased spin and only linearly with D. The benchmark system studied during this period was a Mn_6 cluster with S = 12, blocking temperature of 4.5 K, and U_{eff} measured at 62 cm^{-1} in 2007.[49] Numerous clusters were made in pursuit of increasing spin, but even manyfold increases resulted in ineffective SMMs.[50] The pitfall of this strategy was in the application of the ZFS Hamiltonian in characterizing U_{eff} for a cluster. D values were primarily meant to parameterize the splitting of states caused by mixing. Treating the effective barrier of a spin cluster as a giant spin with the axial anisotropy term, rather than as a function of coupling, proved to be a poor model in predicting magnetic properties. This approach ignored the fact that spin centers in a large cluster can cancel each other's moments out through antiferromagnetic interactions or by simply being pointed opposite of each other based on the symmetry and bonding of the cluster. Many advances in the synthesis and understanding of

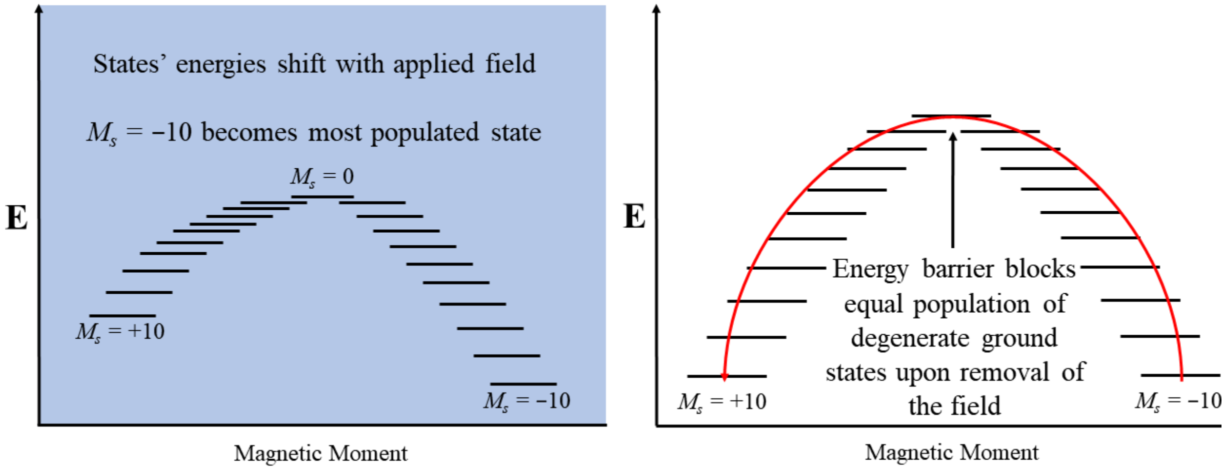

Figure 8: (Left) Qualitative view of M_s states under an external magnetic field (blue shading) causing a lift of degeneracy, triggering the M_s = −10 state to become the ground state (Right) Upon removal of the external field, the degeneracy of the M_s states is returned but equal population is blocked by the energy barrier from $M_s = \pm 10$ to $M_s = 0$

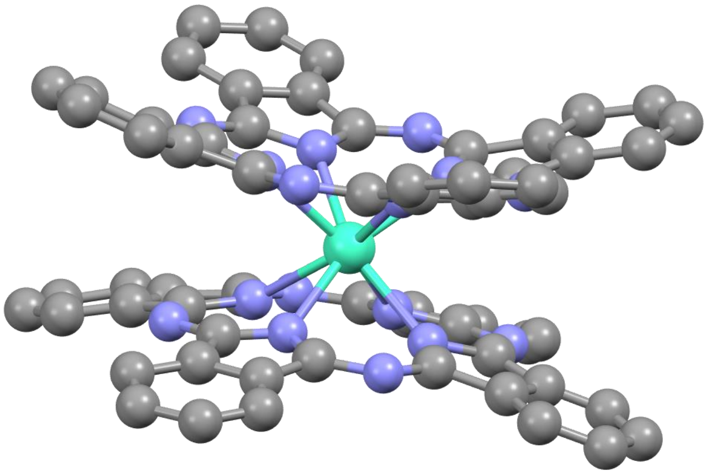

Figure 9: Crystal structure of a Tb phthalocyanine anion magnetically characterized by Ishikawa et al. in 2003. Phthalocyanine sandwich complexes were the first reported lanthanide SMMs

molecular magnetism were made, yet progress in the unique design goals of SMMs was frustratingly hard-won.

The introduction of lanthanide-based SMMs offered an interesting new perspective on design principles to increase U_{eff}. The magnetic characterization of lanthanide phthalocyanine sandwich complexes (Ln = Tb, Dy, Ho, Er, Tm, or Yb) by Ishikawa et al. in 2003 proved to be a major leap forward in the field.[51] This study on these complexes showed that a pursuit of higher nuclearity not the only possibility, and, that given the right system, anisotropy could be thought of as a synthetically-controllable parameter. With the Tb analog being the best-in-class, a single ion ended up displaying a higher effective barrier (~230 cm^{-1}) than any SMM involving the family of multinuclear clusters.

The source of this advantage in superparamagnetism came from the choice in metal center, and it was a conceptual model, ported from solid-state magnetism and given the new versatility of molecular synthetic tunability, that provided the answer.[52] Lanthanide SMMs have a characteristic that transition-metal SMMs lack; their *4f* valence orbitals are contracted and have minimal interaction with ligands. This has two main consequences: (1) the orbitals maintain near-degeneracy leaving the spin-orbit coupling mostly preserved providing anisotropy to the ion, and (2) lanthanides generally have only weak covalent interaction with ligands and their bonding acts much more like point charge interactions. For single-ion lanthanide-based SMMs, these design principles formulate a starting point whereby ideal crystal-field shapes could be predictive of the barrier which controls relaxation between magnetic states. Idealized shapes came in the form of oblate and prolate electron distributions for the lanthanides. Using the shapes as charge potentials, the ideal shape for Tb's electron configuration, for example, is oblate spheroid, matching well with the stabilization by sandwiching, rigid, phthalocyanine ligands. This simple single-ion (magnetocrystalline) anisotropy model provides a general intuition to guide synthesis and further exploration. An explosion of synthetic, physical characterization, and theoretical, efforts on highly anisotropic lanthanide systems has resulted in a series of dysprosium complexes[53-55] with considerably stronger magnetic properties, the current state-of-the-art being a single-ion magnet showing blocking behavior at 80 K with a U_{eff} of 1541 cm^{-1}.

Advancements in Ln SMMs also helped pave the way for new transition metal SMM design principles. With the gains Ln SMMs were showing, some in the field moved away from maximizing spin to maximizing anisotropy. There were two main approaches to do this - enforce strict symmetry to preserve spin-orbit coupling or maximize state interactions to increase ZFS anisotropy with less emphasis on the ligand symmetry. Many have offered predictions to maximize ZFS values, with a notable addition by Gomez-Coca et al,[56] but these predictions proved mercurial as the empirically-based ZFS parameter cannot reliably be used to forecast the effects of covalency on state interactions. On the other hand, success was found in preserving spin-orbit coupling by focusing on ligand binding modes that enforce strict symmetries. One geometry that had particular success was linear coordination,[57-59] with the current largest barrier being a linear Co(II) complex published by Bunting et al in 2018 with a U_{eff} of 450 cm^{-1}. Although this complex had the largest barrier reported for a transition metal, it lacked a measurable blocking temperature as a result of barrier relaxation dynamics.

Through the study of the above Dy and Co complexes, it seems that the discipline is fast approaching the physical limit of single-ion magnetism and the best system so far showcases superparamagnetic behavior slightly above liquid nitrogen temperatures. These gains are amazing from the point of view of what seemed theoretically feasible a decade ago – let alone synthetically demonstrated. They also point to an exciting prospect – SMM research has reached a point where it has the potential to connect with many other fields across science and technology. Doing so is no longer a distant theoretical possibility, it only depends upon expanding the models from simply how to make "the best" SMM by a narrow, self-determined set of criteria, to a more general goal of how to design the magnetic structure and transition probabilities for any goal involving control over the magnetic relaxation in a molecule. This wider set of goals is an exciting challenge that will necessarily broaden the scope of SMM research. At its essence, it requires versatility.

A large part of the movement towards versatility in SMM design can be described as a push to higher nuclearity, with the caveat that preservation of the anisotropy comes before building nuclearity. Advancements in increasing nuclearity have come in the form of single-chain magnets, the 1D analog of SMMs, and other higher-dimensional systems with varied results,[60-62] but as no system has shown the same strength in superparamagnetic properties that the Dy systems have shown, there is vast potential in developing building blocks from highly anisotropic SMMs. If one can synthesize an SMM with ligand motifs that can be modified to increase nuclearity, one could unlock higher dimensional magnetic materials with fascinating properties. However, to synthesize such a building block, significant groundwork would need to be laid to understand the effects of metal-ligand bonding and what effects change the magnetic properties. In Chapter Two of this dissertation, I will review our attempts at building ligand motifs that would potentially act as the template for SMM building blocks.

Another issue in the field to be addressed is developing consistent modelling techniques that give some insight into physical meaning without overparameterization. We have discussed much about the potential pitfalls of effective Hamiltonians and their limitations; however, through the use of LFT and CF approximations we can potentially build methods that accurately predict both spectroscopic and magnetic properties. In Chapter Three, I will review our attempts at modelling octahedral Co(II) through a combination of spectroscopic and magnetic data.

Chapter 2: Exploring the properties of Co complexes ligated by mesoionic carbenes

2.1 Introduction

Using ligand coordination to fine-tune the electronic structure of transition metals is a mature area of both organometallic and inorganic coordination chemistry.[63] The discovery of distinctly new properties and reactivity, therefore, is often contingent upon the use of ligands that induce non-standard perturbations upon the metal center. An iconic example was the introduction of N-heterocyclic carbene (NHC) ligands where strong σ-donation and wide steric tunability led to an explosion of newly accessible organometallic reactivity. NHC-ligated complexes with nearly every transition metal have been isolated to target luminescent, magnetic, catalytic, and a wide range of other properties.[64] In addition to NHCs, the electronic versatility of carbenes has diversified to include systems such as the strong σ-donating and π-accepting cyclic alkyl-amino carbenes (CAACs)[65] and the more purely σ-donating mesoionic carbenes (MICs) (Figure 10).[66-70]

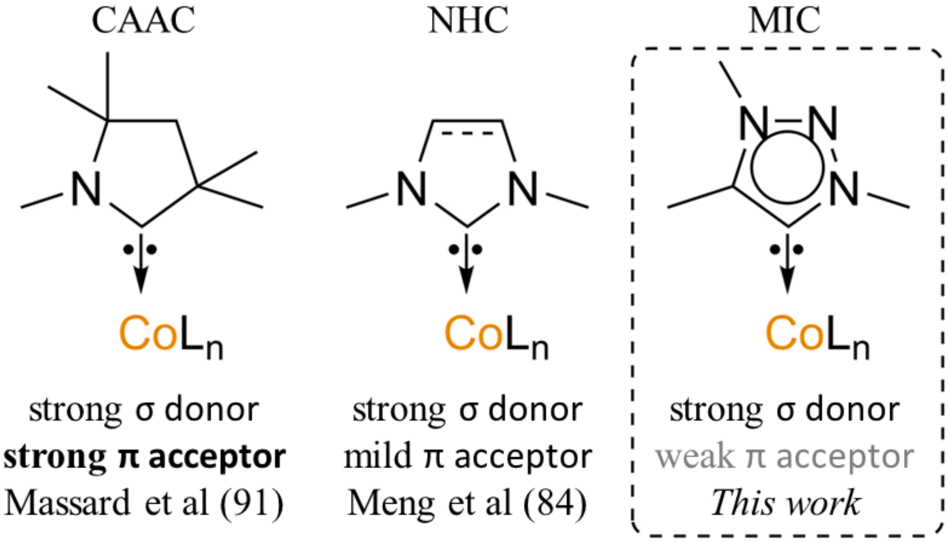

Figure 10: Cobalt complexes bearing carbenes with different donor and acceptor properties. Shown here are some of the first complexes containing CAACs (left), NHCs (middle), and MICs (right)

These variable electronic properties offer an intriguing and less explored contrast to the NHCs, especially for first-row transition metal complexes where only 36 such MIC complexes have been reported in the Cambridge Structural Database as of the original publication of this paper.

Amongst the transition metals, complexes of Co(II) provide some of the most diverse and interesting electronic structure behavior due to an inherent ground-state bistability from Kramer's degeneracy and relatively large spin-orbit coupling.[71] Tetrahedrally-coordinated high-spin Co(II) is particularly intriguing from an electronic structure standpoint. While its $^4A_2$ ground state has no first order orbital moment, it does have a wide variability in ligand-field strength, distortions in symmetry, and spin-orbit coupling that all contribute to a rich manifold of low-lying excited states. These provide a source of electronic structure tunability, opening up diverse applications from olefin oligomerization,[72] electrocatalytic C-C bond formation,[73] quantum sensing and computing,[74] as well as molecular spintronics,[75] and single-molecule magnetism (SMM).[76-82]

Despite intense interest in both Co(II) and MICs, there are no examples of structurally-characterized complexes combining this metal-ligand pair. In fact, only two MIC complexes with any Co oxidation state have been previously characterized, both being Co(III).[83] Additionally, while there have been a small number of reported SMMs containing carbenes in the literature,[58, 84-91] no comprehensive magnetic study on a series of simple metal halide carbenes of any type is available, nor have the magnetic properties of any MIC-containing compound been explored, leaving an invaluable characterization method for complex electronic structures untapped. To this end we synthesized and used a combination of optical absorption spectroscopy and magnetometry to characterize a series of tetrahedral complexes comprising $CoX_2{}^{Dipp}MIC_2$ ($X = Cl^-$, **1**; Br^-, **2**; and I^-, **3**) (Figure 11). In addition to the new information garnered about the Co(II)-MIC interaction, we demonstrate the further control over the magnetic anisotropy through the halide ligand, with

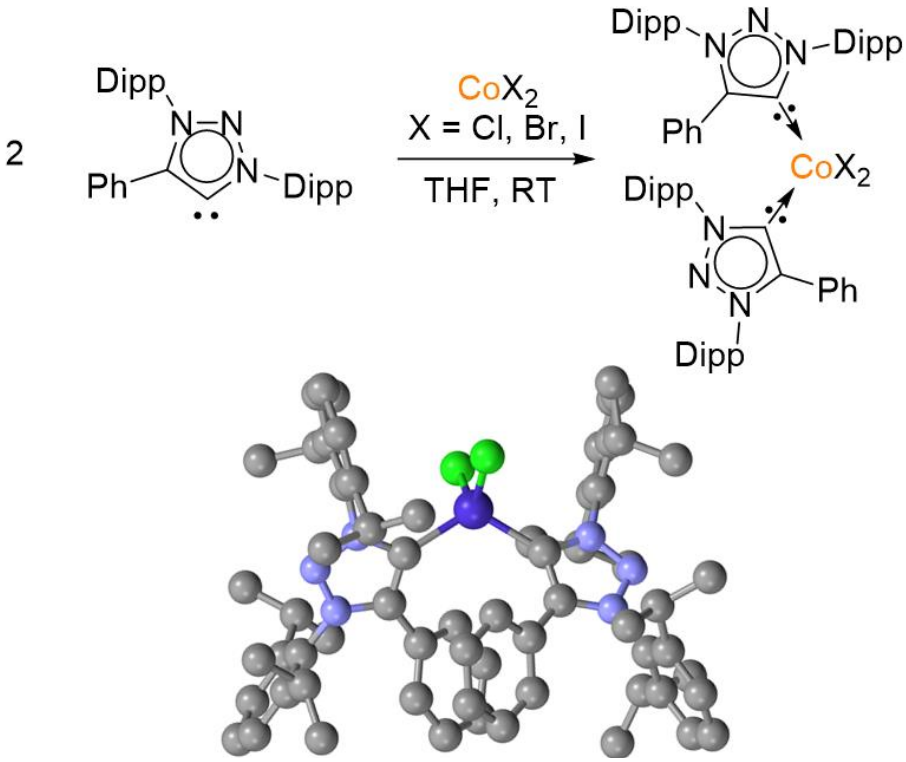

Figure 11: (Top) Reaction scheme for compounds **1**-**3**. (Bottom) Crystal structure of **1** with spheres representing C (grey), Co (dark blue), N (light blue), and Cl (green). Hydrogen atoms have been omitted for clarity

an approximate doubling of the axial zero field splitting (ZFS) anisotropy constant $|D|$ between 1 and 3. In this dissertation, I will also present yet unpublished data that was not included in the original manuscript regarding our investigations on redox properties as well as further spectroscopic and magnetic investigations.

2.2 General Methods and Procedures

Experimental Procedure

All chemicals were purchased from commercial suppliers unless otherwise indicated. All air and moisture-sensitive compounds were handled using a standard mBraun glovebox containing purified N_2 or standard Schlenk line techniques using an argon atmosphere. Solvents for moisture-sensitive reactions were purified on an activated alumina column and stored over a 1:1 mixture of 3 Å and 4 Å molecular sieves. All non-volatile solids were dried at 110 °C under vacuum.[92]

Physical Measurements

Single crystal X-ray diffraction data for all compounds were collected at 100 K on a Bruker κ Diffractometer with a Mo Kα radiation source equipped with an Apex II Area Detector. Structures were solved using Olex[93] via the SHELXT[94] routine and refined with SHELXL.[95] Magnetic data was collected on a Quantum Design Magnetic Properties Measurements System 3 SQUID Magnetometer in Direct Current scan mode. Magnetic measurements were performed on crushed crystallized samples pressed into plastic sample holders to prevent torquing. DC susceptibility measurements were collected with HDC = 1000 Oe with a sweep rate of 4 K/min. All data were corrected for diamagnetism using Pascal's constants.[96] Fitting of magnetic data was done using PHI.[17] UV-Vis-IR absorption spectroscopy was performed using an Agilent Cary 5000 with dry THF as the solvent. Elemental analysis (CHN) was performed by Midwest Microlab. Far IR Magnetospectroscopy (FIRMS) measurements were performed by the National High Magnetic Field Laboratory 5 mg of a polycrystalline sample of **1-3** at 4.2 K for IR energies <900 cm−1 using a Bruker Vertex 80v vacuum FTIR spectrometer with a resolution of 0.3 cm^{-1}.

Ligand Synthesis [^{Dipp}MIC-H]Cl

Synthesis of the triazolium salt was adapted from literature procedure.[97] A neat mixture of 2,6-diisopropylaniline (75 mmol, 13.30 g) was mixed with half an equivalent of isoamyl nitrite (37.5 mmol, 4.39 g) at room temperature. The dark red solution was allowed to sit at room temperature for 4 h and then stored at -20 °C and allowed to crystallize overnight. The resulting slurry was filtered and washed with cold ethanol and the triazene was isolated as large yellow blocks which were used without further purification (yield 42%, 31.5 mmol, 11.5 g). Triazolium chloride salts were synthesized from the resulting triazene in the presence of 1.5 equivalents (47.3 mmol, 5.13 g) of tert-butyl hypochlorite in dry dichloromethane at −78 °C. Upon addition of the oxidant, the solution immediately turned dark purple/brown and was stirred for 30 minutes. A slight excess of phenylacetylene (42.3 mmol, 4.32 g) was then added and the reaction stirred overnight in the dark and allowed to slowly come to room temperature. The solvent was then removed in vacuo, and the resulting purple powder was triturated for 2 hours in diethyl ether. The resulting slurry was filtered and the triazolium salt was isolated as an off-white powder (Yield 65%, 10.3 g). 1H-NMR (CD_3CN, 300 MHz): 9.17 (s, 1H), 7.77 (td, 2H), 7.61-7.48 (m, 7H), 7.44-7.41 (m, 2H), 2.46 (sept, 2H), 2.38 (sept, 2H), 1.32 (d, 6H), 1.18 (d, 6H), 1.12 (d, 6H), 1.01 (d, 6H).

Synthesis of $CoX_2{}^{Dipp}MIC_2$ (X = Cl, Br, I)

Free mesoionic carbene was generated from the deprotonation of [^{Dipp}MIC-H]Cl (1 mmol, 0.502 g) in a slurry of 5 mL THF upon addition $K(N(SiMe_3)_2)$ (1 mmol, 0.199 g) dissolved in 10 mL THF. The resulting mixture instantly turned brown upon addition of base and produced a white precipitate. The reaction was allowed to proceed overnight. KCl was removed via centrifugation and the supernatant containing free ^{Dipp}MIC was added to 0.45 equivalents of CoX_2 (X = Cl, Br, I) and stirred for 6 hours. Volatiles were removed in vacuo and the solid was washed with Et_2O to remove excess MIC. The remaining solid was dissolved in THF, transferred into a tared vial, and the solvent was removed in vacuo to produce sapphire blue, aqua, and green $CoCl_2{}^{Dipp}MIC_2$ (**1**), $CoBr_2{}^{Dipp}MIC_2$ (**2**), and $CoI_2{}^{Dipp}MIC_2$ (**3**) respectively. Yields were 62%, 56%, and 55% for 1, 2, and 3 respectively. Sapphire blue, aqua, and green crystals suitable for X-ray analysis were obtained by slow diffusion of pentane into toluene. Solid samples were air stable for at least 6 months stored in vials stored at room temperature but were susceptible to degradation in wet THF—presumably from the protonation of ligand from water. CHN analysis (calc., found) for 1: C (72.44, 73.23), H (7.41, 7.60), N (7.92, 7.29); for 2: C (66.84, 67.68), H (6.84, 6.89), N (7.31, 7.36); for 3: C (61.79, 61.77), H (6.32, 6.38), N (6.76, 6.43).

Reduction of $CoX_2{}^{Dipp}MIC_2$ (X = Cl, Br, I)

All three halide analogs of the Co(II) complex were susceptible to one electron reduction to their Co(I) analogs. 0.250 g of $CoX_2{}^{Dipp}MIC_2$ was reduced using 1 equivalent of Na in an amalgam of Hg in 10 mL THF. The reaction was stirred overnight, and each analog turned into a dark red solution. NaX (X = Cl, Br, I) and Hg were removed via centrifugation and the supernatant was collected and solvent removed in vacuo to produce dark red powders of $CoCl^{Dipp}MIC_2$ (**4**), $CoBr^{Dipp}MIC_2$ (**5**), and $CoI^{Dipp}MIC_2$ (**6**). Due to reactions not going to completion and similar solubility properties preventing purification between reactants and products, yields were not calculated. Single crystals suitable for X-ray analysis were grown by slow vapor diffusion of pentane into toluene solutions.

Reduction of $CoCl^{Dipp}MIC_2$

To investigate the ability of MICs to stabilize the Co(0) analog, reduction of $CoCl^{Dipp}MIC_2$ (0.250g, ~0.25 mmol) was reacted with 1 equivalent of Na in an amalgam of Hg. The reaction was allowed to stir overnight, and the mixture turned from a dark red solution into a black solution. NaCl was removed via centrifugation and solvent removed in vacuo to give $Co(\kappa^2\text{-}{}^{Dipp}MIC)_2$ (**7**). Due to purity issues, percent yield was not calculated. Crystals suitable for X-ray analysis were produced through vapor diffusion of pentane into product dissolved in toluene

2.3 Results and Discussion

Compounds **1**–**3** were obtained in good yield by treatment of a THF solution of the free MIC with the corresponding divalent cobalt halogen precursors (CoX_2, X = Cl^-, Br^-, I^-; Figures 11 and 12).The structures of **1**–**3** were confirmed by X-ray crystallography and elemental analysis. As expected, in the solid-state, all three complexes have similar coordination environments although they crystallized in distinct space groups ($P\bar{1}$, $P2_{1/n}$, and P_{ccn} respectively). Select bond angles and distances between the cobalt center and ligands are tabulated in Table 2. The Co coordination environment in all three complexes is distorted tetrahedra with approximate C_{2v} symmetry. The phenyl substituents are arranged with parallel faces, which can be attributed to π-stacking interactions. Cobalt–carbene distances are comparable to bis-NHC bis-halide Co(II)

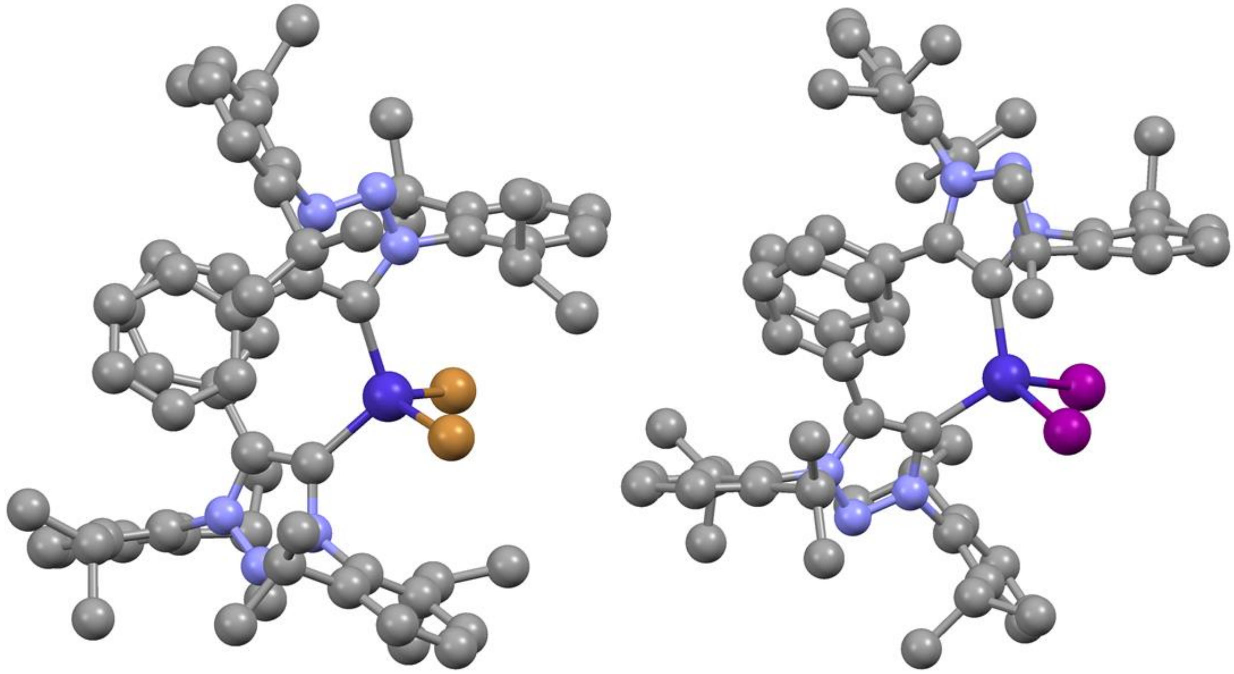

Figure 12: Crystal structure of **2** (left) and **3** (right) with spheres representing C (gray), Co (dark blue), N (light blue), Br (orange), and I (purple). Hydrogen atoms have been omitted for clarity.

Table 2: Selected bond lengths, angles, and distortion parameters for complexes **1**-**3**

	d(Co-C) (Å)	d(Co-X) (Å)	α (largest L-Co-L) (°)	β (second largest L-Co-L) (°)	τ_δ
$CoCl_2{}^{Dipp}MIC_2$ (**1**)	2.061/2.062	2.256/2.262	117.25(6)	116.87(1)	0.890
$CoBr_2{}^{Dipp}MIC_2$ (**2**)	2.044/2.054	2.408/2.416	116.79(3)	114.28(4)	0.895
$CoI_2{}^{Dipp}MIC_2$ (**3**)	2.089	2.609	117.25(0)	117.25(5)	0.890

complexes.[98-99] The angular distortion from ideal tetrahedral geometry was calculated using an angular distortion parameter:

$$\tau_\delta = \frac{360 - (\alpha + \beta)}{141}\delta \tag{2.1}$$

$$\delta = \frac{\beta}{\alpha} \tag{2.2}$$

where α and β define the largest and second largest L-Co-L angles.[100] All three structures are remarkably similar in terms of total distortion from ideal tetrahedral geometry, with τ_δ values of ~0.89 being found for all three structures.

Variable temperature magnetic susceptibility (T = 1.8–300 K) and variable field (H = −7–7 T) DC magnetometry data were collected and fit globally (Figure 13) using an effective spin Hamiltonian with axial zero-field splitting (ZFS) and Zeeman contributions (Equation 2.3) using the PHI software package.[17]

$$\hat{H} = D\hat{S}_z^2 + g_{iso}\mu_B S \cdot B \tag{2.3}$$

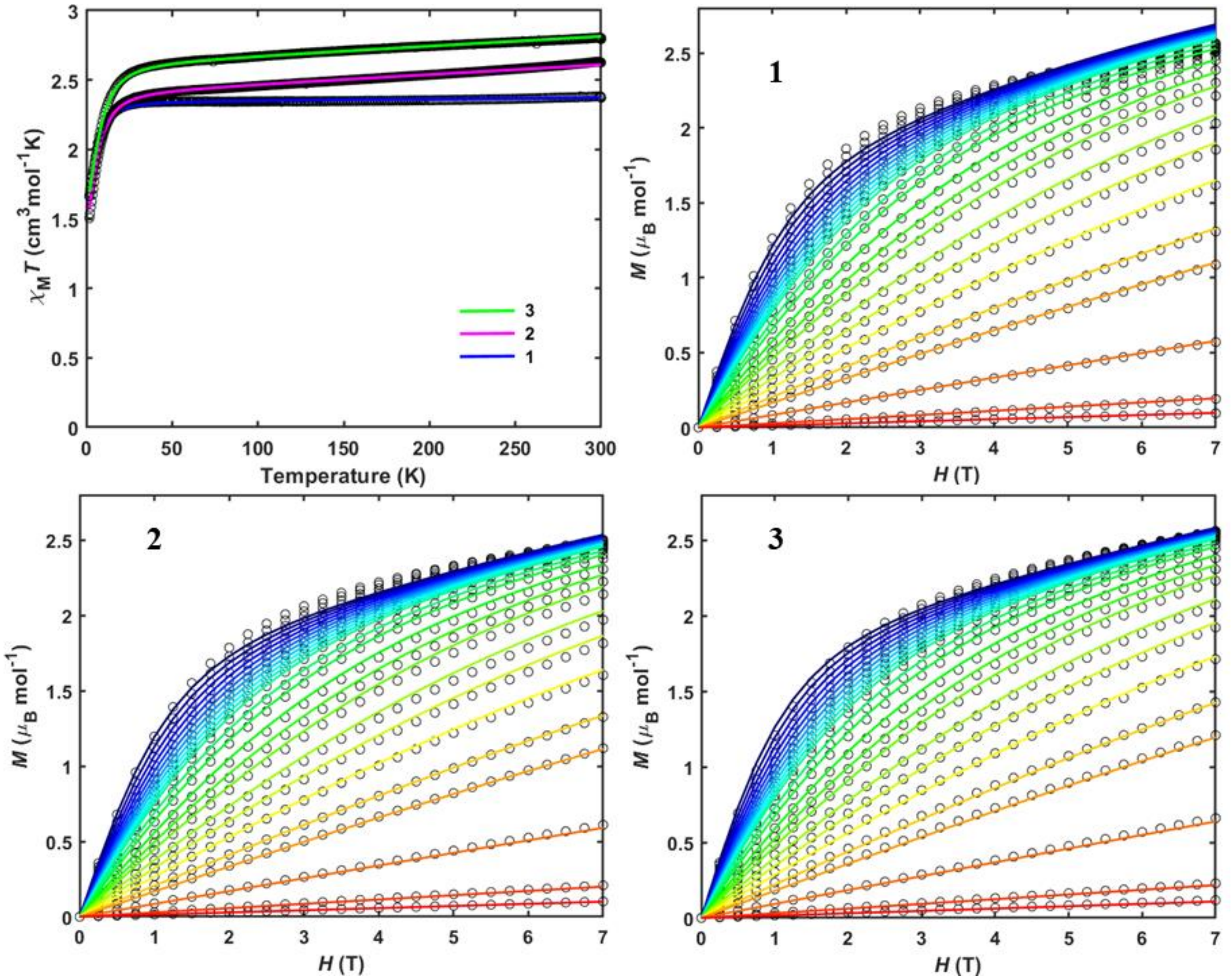

Figure 13: (Top Left) Magnetic susceptibility data (black) and fits of compounds (colored lines) **1**-**3**. Fits were modelled in conjunction with *M* vs. *H* data, here labeled **1**-**3**, corresponding with the modelled compound.

To reduce correlation between the effective g value and our phenomenological anisotropy term, an isotropic g value was used. Parameter error bars were determined through the PHI software, as were the residual values used to locate minima within the parameter space (Equation 2.4):

$$Residual = \left[\sum_{i=1}^{points} \left(M_{exp} - M_{calc}\right)^2\right]\left[\sum_{i=1}^{points} \left(\chi_{exp} - \chi_{calc}\right)^2\right] \tag{2.4}$$

Best fit values of D = −6.54 ± 0.02, −8.27 ± 0.01, and −9.67 ± 0.01 cm^{-1}, and g = 2.24, 2.25, and 2.36, were obtained for **1**, **2**, and **3,** respectively. Errors in the g value were negligible compared to the quoted number of significant figures. A two-dimensional analysis of the parameter space was used to locate additional minima in the residuals with positive D values [Figure 14 (**1**), Figure 15 (**2**), Figure 16 (**3**)]. Best-fits constrained within these local minima yield $D = 8.04 \pm 0.02$ (**1**), 10.47 ± 0.03 (**2**), and 9.68 ± 0.02 (**3**) cm^{-1} and $g = 2.24$ (**1**), 2.26 (**2**), and 2.36 (**3**). Based on a residual analysis (Equation 2.4), the global minima (negative D values) were reduced by factors of 22% (**1**), 83% (**2**), and 96% (**3**) compared to their positive counterparts (Table S2).

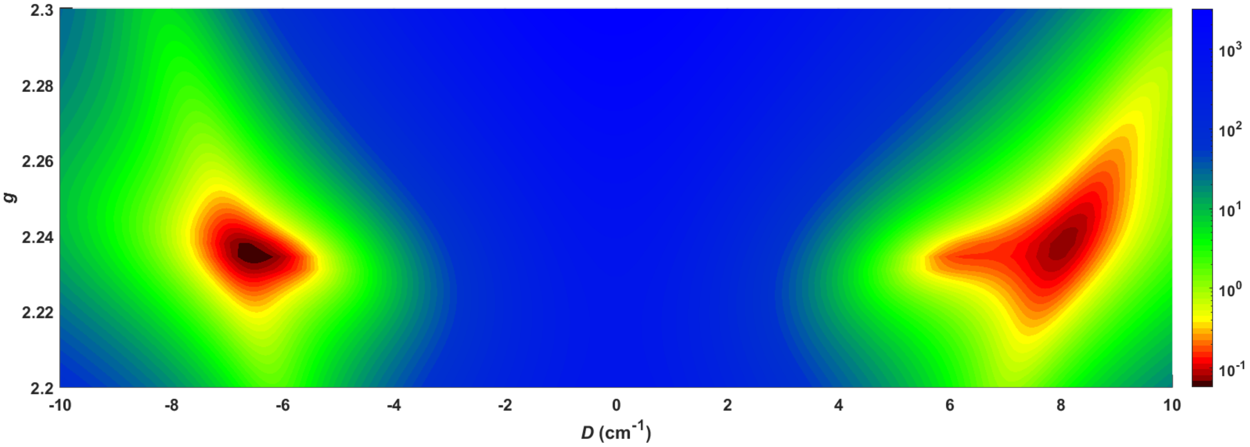

Figure 14: Survey of the effects of D and g on compound **1** showing two wells of best fits corresponding to a positive and negative D value. Dark red signifies best fit with blue signifying poor fits

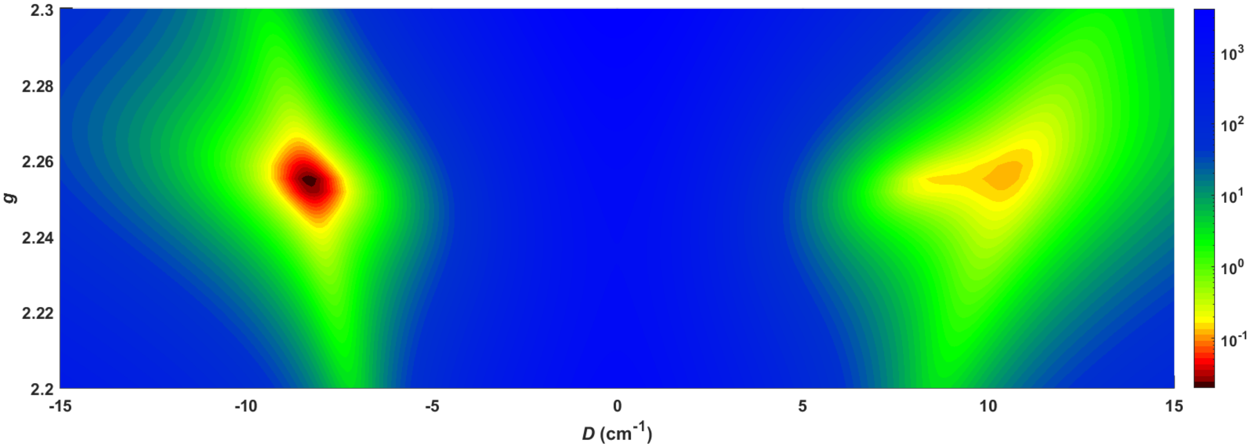

Figure 15: Survey of the effects of D and g on compound **2** showing two wells of best fits corresponding to a positive and negative D value. Dark red signifies best fit with blue signifying poor fits

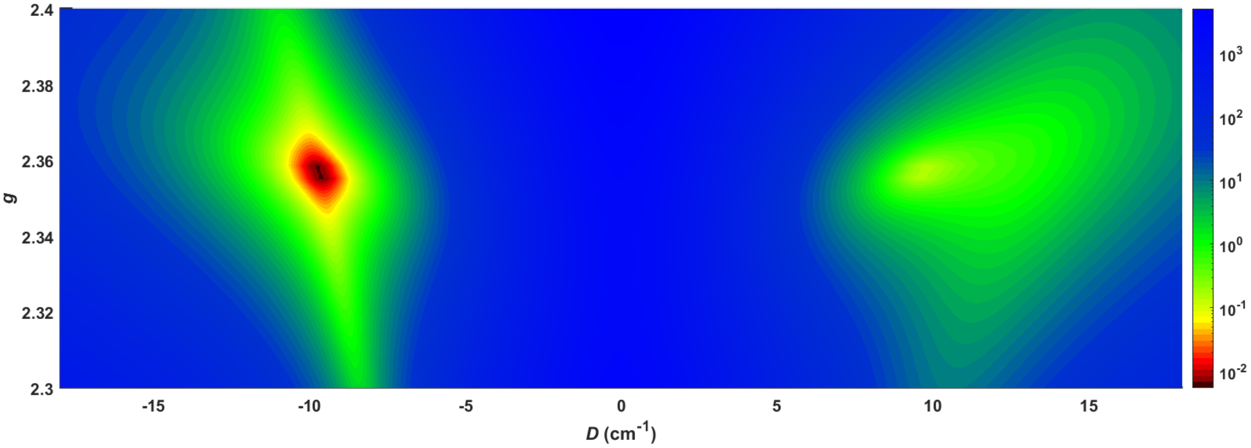

Figure 16: Survey of the effects of *D* and *g* on compound **3** showing two wells of best fits corresponding to a positive and negative *D* value. Dark red signifies best fit with blue signifying poor fits

Table 3: Best fits of compounds **1-3** for both positive and negative *D* wells seen in the surveys

	Negative *D* fit	Negative *D* residual	Positive *D* fit	Positive *D* residual
$CoCl_2{}^{Dipp}MIC_2$ (**1**)	*D* = -6.54 ± 0.02 *g* = 2.24	0.05695	*D* = 8.04 ± 0.02 *g* = 2.24	0.07284
$CoBr_2{}^{Dipp}MIC_2$ (**2**)	*D* = -8.27 ± 0.01 *g* = 2.25	0.02008	*D* = 10.47 ± 0.03 *g* = 2.26	0.12033
$CoI_2{}^{Dipp}MIC_2$ (**3**)	*D* = -9.67 ± 0.01 *g* = 2.36	0.00518	*D* = 9.68 ± 0.02 *g* = 2.36	0.12586

Samples 2 and 3 displayed obvious signs of temperature independent paramagnetism (TIP) consistent with a susceptibility contribution unaffected by the Boltzmann population. To account for this, empirical values of χ_{TIP} = 0.0001, 0.0008, and 0.0007 cm^{3}mol^{-1} were employed for **1**, **2** and **3**, respectively, similar in magnitude to other four-coordinate Co complexes reported in the literature.[101]

Although there are no direct comparisons for the ZFS values available in the literature for bis-carbene bis-halide Co(II) complexes, these values are within the range of reported values for bis-carbene two coordinate Co(I) complexes (*D* = −8.2, −0.11, and 33.4

cm^{-1}), and two and three coordinate isoelectronic Fe(I) complexes (D = 19.8, −13.6 cm^{-1}).[84, 87] It is interesting that axial D-values for **1**-**3** approach the magnitude of lower-coordinate systems, as typically lower-coordination of similar complexes leads to higher D-values due to smaller crystal fields.

Complexes **1**-**3** display room temperature $\chi_M T$ values of 2.37, 2.63 and 2.79 $\text{cm}^3\text{mol}^{-1}\text{K}$, respectively (Figure 13, top left). The value of $\chi_\text{M}T$ down to ~25 K is largely independent of temperature, especially for **1**, while **2** and **3** show large contributions from TIP. At lower temperatures, the drop accelerates to reach $\chi_\text{M}T \approx 1.6\ \text{cm}^3\text{mol}^{-1}\text{K}$ for each compound. The room-temperature values are significantly larger than the spin-only value for a tetrahedrally coordinated d^7 metal with S = 3/2, suggesting a large second-order orbital contribution. This contribution is a manifestation of mixing excited states into ground states, with lower-field ligands (i.e. $\text{Cl}^- > \text{Br}^- > \text{I}^-$) bringing excited states closer in energy to the ground state. The room-temperature magnetic susceptibilities of these compounds are larger than their bis-NHC, bis-halide Co counterparts,[102] while being slightly less than previously reported two- and three-coordinate Co(II) and isoelectronic Fe(I) carbene-based SMMs.[58, 87]

The tuning effect induced by the halide series was also apparent in spectroscopic data. Normalized to max intensity, UV/Vis/near-IR absorption data (Figure 17) show two distinct regions of excited energy states ranging from roughly 18,000–13,000 and 11,000–5,500 cm^{-1}, in close agreement with reported bis-NHC bis-halide Co(II) complexes.[98] These regions correspond to the transitions of the tetrahedral $^4\text{A}_2(^4\text{F})$ ground state to the excited $^4\text{T}_1(^4\text{F})$ and $^4\text{T}_1(^4\text{P})$ states, with the $^4\text{A}_2(^4\text{F}) \rightarrow {}^4\text{T}_2(^4\text{F})$ transition outside of our measurement window.[103] The spectra of the complexes show a clear red-shift with

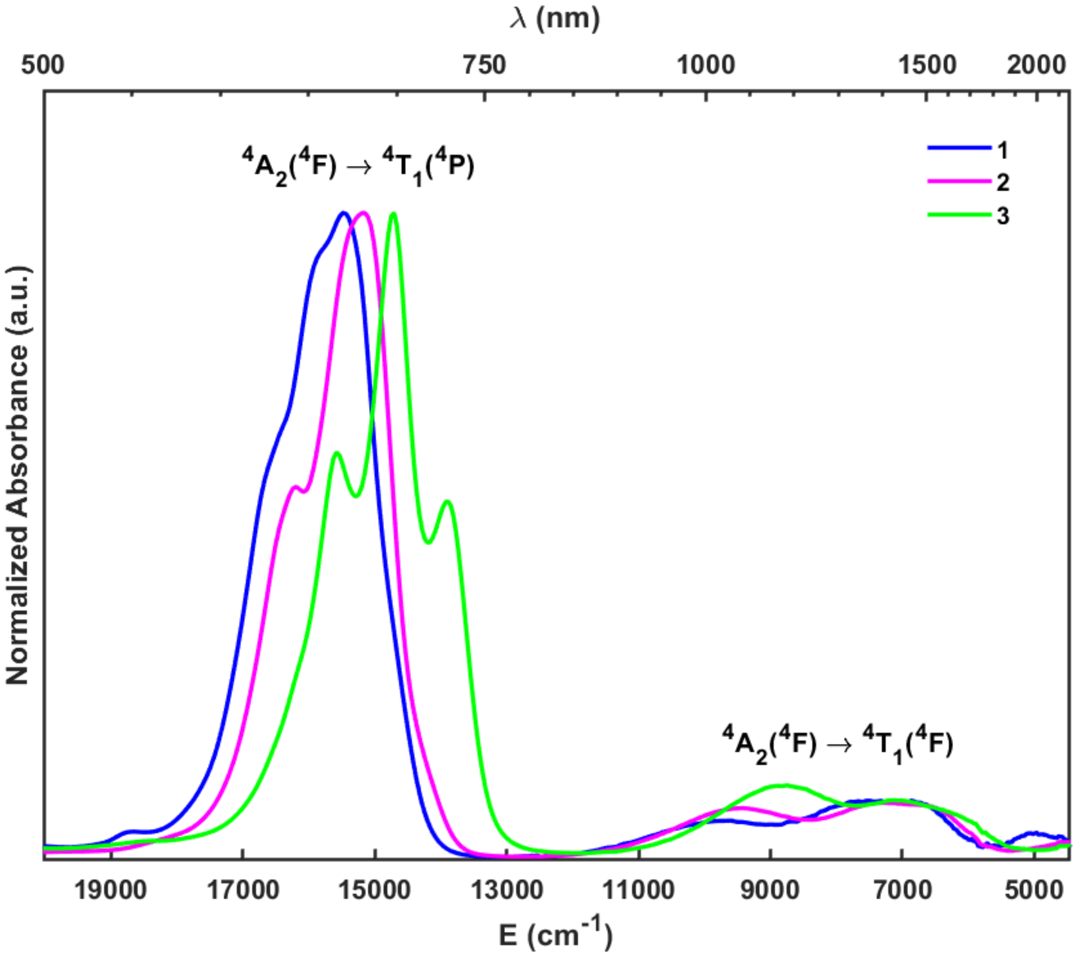

Figure 17: Normalized absorbance data for compounds **1**-**3** in THF showing red shifts as halide size increases

increasing halide size for both regions, which can be attributed to the lower ligand-field strength of the heavier halides. Both regions for all three complexes contain multiple features resulting from spin-orbit coupling and splitting of the parent tetrahedral geometry to C_{2v} symmetry, which splits the $^4T_1$ states into their $^4A_1$, $^4B_2$, and $^4B_1$ components.[104] To quantify the ligand field, Tanabe-Sugano diagrams were used to calculate *Dq* values.[105] Using the median energy value from the two excitation ranges in the absorption data to approximate a non-distorted tetrahedral excitation, *Dq* and B were calculated as *Dq* = 394, 387, and 367 cm^{-1} and B = 635, 615, and 571 cm^{-1} for complexes **1**-**3**, respectively. These values are slightly larger than their phosphine-halide analogs, indicative of stronger σ-donation of the MIC ligands.[106]

The ligand field of the complex plays a critical role in the low-lying energy states caused by ZFS. The two components contributing to ZFS are the minor direct spin-spin interactions and the dominant second-order spin-orbit coupling (SOC) introduced by mixing of ground and excited states.[107] Computational[101, 108] and experimental[109-113] works have shown how anisotropy can be influenced via heavy atom coordination with further corroboration for ligand influence on ZFS in tetrahedral Co halide complexes emerging over the past several years.[79, 114-115] Complexes 1–3 show a clear trend in their $|D|$ values consistent with the expected electronic-structure effect. Specifically, we can attribute this trend to three effects: (1) Ligand-field strength correlates inversely with halide size, bringing the Co excited-states lower in energy for larger halides (Figure 17). This decreased ligand-field strength allows more mixing between Co states, which incorporates more SOC into the ground state. (2) Covalency in halides increases with halide size, yielding a larger contribution of ligand character to the molecular orbitals. (3) Relativistic effects in the larger halides allow for greater SOC, an effect that is enhanced due to the increased covalency and mixed states.

Post-publication, we attempted to further probe the magnetic properties of **1**-**3** through the use of Far-IR Magnetospectroscopy (FIRMS).[116] This method can be used to determine ZFS values by measuring the response of low-energy excitations to a magnetic field. Any excitation that has a response to a magnetic field must be from or coupled to a paramagnetic state; conversely, if the absorption has no response it is from some vibrational mode in the solid with no magnetic moment. The ZFS value of the chloride analog was not able to be resolved due to it being below the limit of detection; however, both **2** and **3** had measurable ZFS values. $\mathrm{CoBr_2}^{\mathrm{Dipp}}\mathrm{MIC_2}$ was measured to have a ZFS value of -14.0 $\mathrm{cm^{-1}}$ while $\mathrm{CoBr_2}^{\mathrm{Dipp}}\mathrm{MIC_2}$ was measured to be -19.1 $\mathrm{cm^{-1}}$ as shown in Figure 18 and Figure 19.

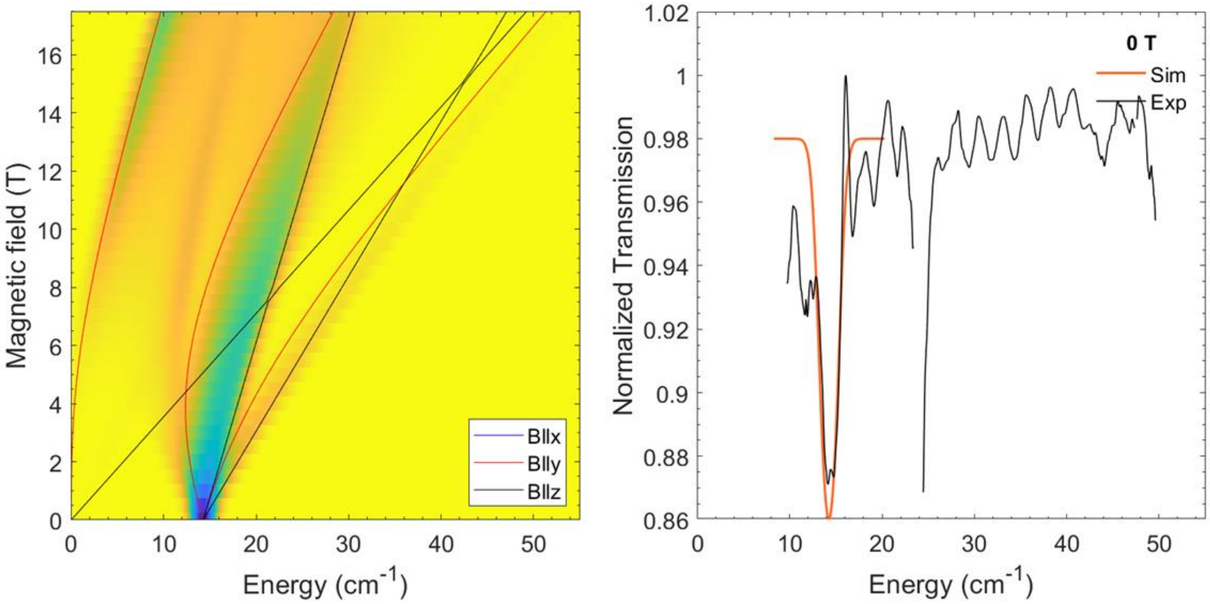

Figure 18: (Left) Measured shifts in Far-IR data of (**2**) in response to a magnetic field. These values are used to predict (right) the ZFS of the compound

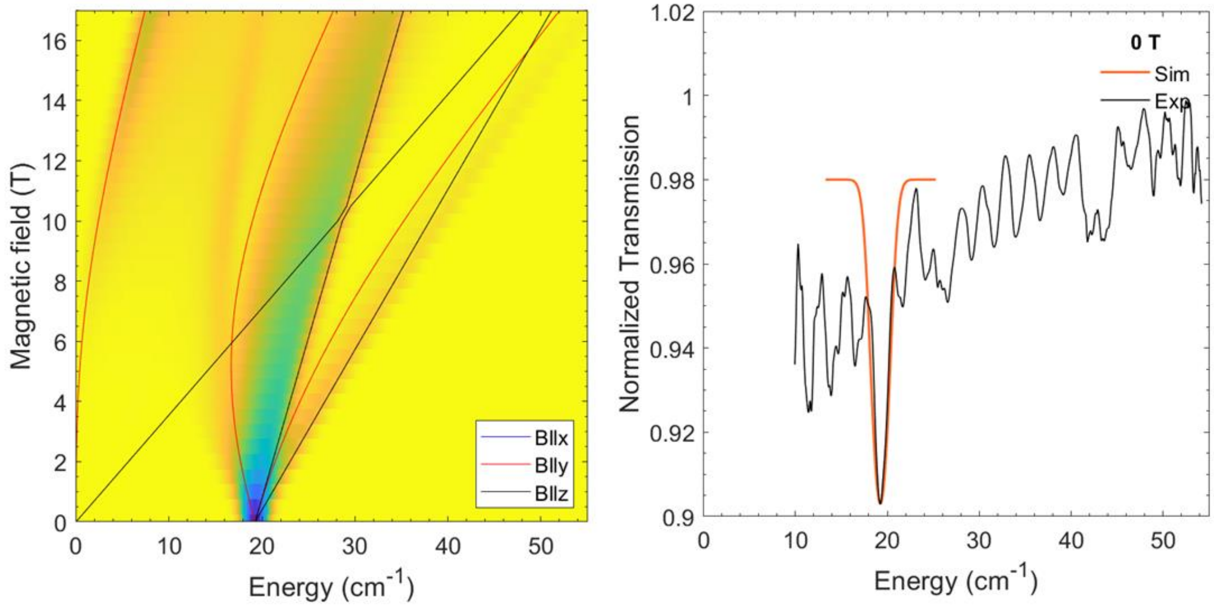

Figure 19: (Left) Measured shifts in Far-IR data of (**3**) in response to a magnetic field. These values are used to predict (right) the ZFS of the compound

These FIRMS data correspond well with the predicted trend and modeled *D* values calculated through PHI.

The redox properties of these complexes were also probed. Complexes **1**-**3** were reacted with one equivalent of sodium amalgam. Although single-crystals were obtained through vapor diffusions, purification was never achieved as the reactions would not go to completion and reactants and products had very similar solubility properties. Crystal structures obtained showed three-coordinate Co(I) complexes as shown in Figure 20 (Cl), Figure 21 (Br), and Figure 22 (I). A second reduction was also attempted on the unpurified Co(I) complex in an attempt to probe the Co-MIC reactivity. After reacting overnight with an equivalent of sodium amalgam and crystalizing through vapor diffusion, a Co(II) product (Figure 23) was formed that seemed to have gone through two oxidative additions across the benzyl C-H bond followed by a reductive elimination, suggesting that Co-MIC complexes may act as C-H activation catalysts. Again, due to purity issues, further characterization was not completed.

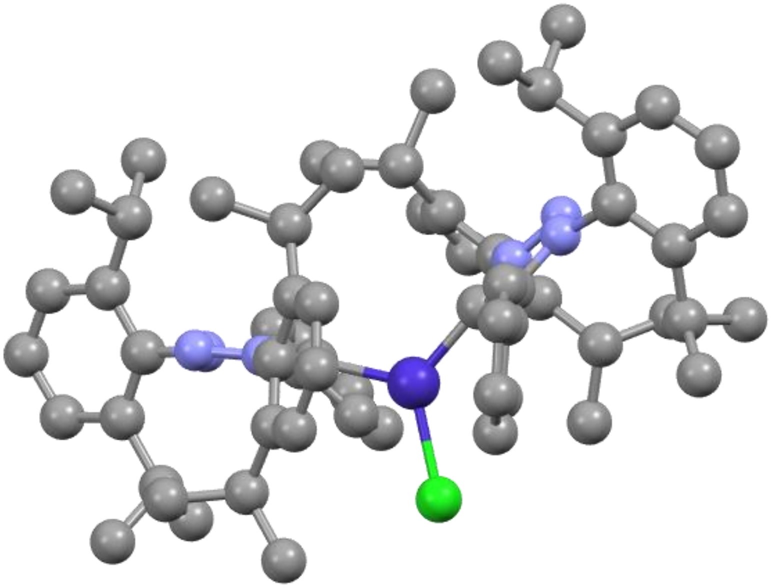

Figure 20: X-ray structure of $\mathrm{CoCl^{Dipp}MIC_2}$, C (gray), Co (dark blue), N (light blue), and Cl (green), Hydrogen atoms have been omitted for clarity.

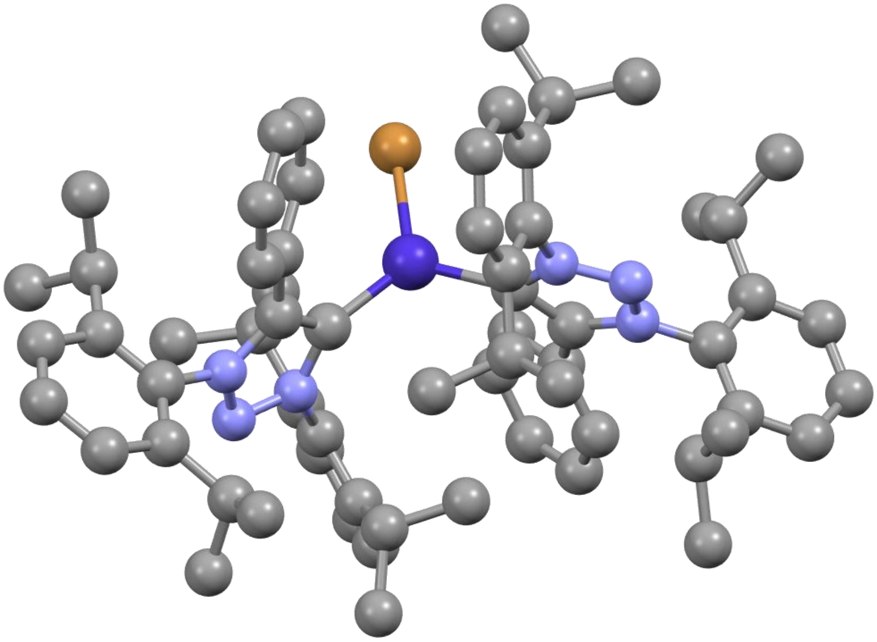

Figure 21: X-ray structure of $CoBr^{Dipp}MIC_2$, C (gray), Co (dark blue), N (light blue), and Br (orange). Hydrogen atoms have been omitted for clarity.

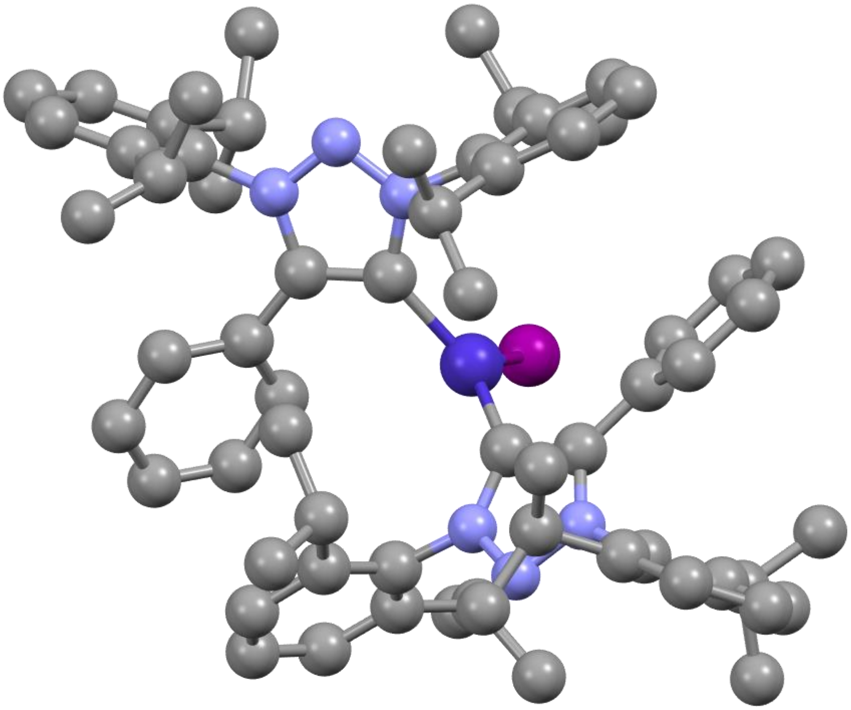

Figure 22: X-ray structure of $CoI^{Dipp}MIC_2$, C (gray), Co (dark blue), N (light blue), and I (purple). Hydrogen atoms have been omitted for clarity.

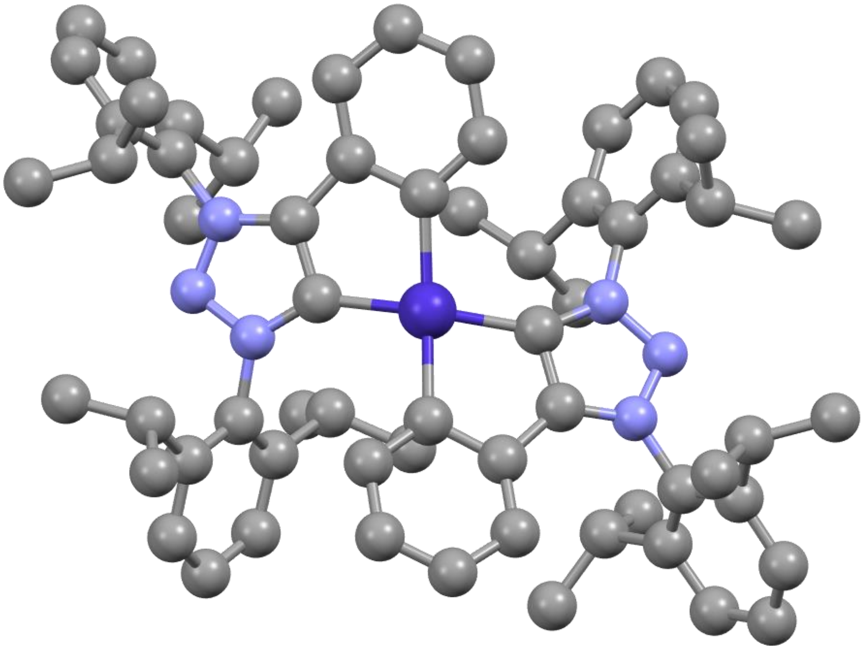

Figure 23: X-ray structure of Co(κ^2-$^{\text{Dipp}}$MIC)$_2$, C (gray), Co (dark blue), N (light blue), and I (purple). Hydrogen atoms have been omitted for clarity.

2.4 Conclusion

In summary, we present the first synthesis and electronic-structure analysis of Co(II)–MIC complexes. These compounds show clear correlations between halide size, excited-state energies, and ZFS. Analysis of magnetic and spectroscopic data revealed the ability of ligands to incorporate varying levels of second-order SOC into the metal center itself. The synthesis of these complexes paves the way for further studies on Co–MIC complexes to probe carbene effects on low-coordination environments. Now that a baseline for understanding changes in axial anisotropy in carbene-containing compounds has been set, future work will focus on making direct comparisons between MIC complexes and their NHC/CAAC counterparts. Expanding upon these trends will allow targeted development of systems that exploit the unique nature of the MIC ligand to control electronic and magnetic structure.

The material in Chapter 2 of this dissertation was adapted from: Mantanona, A.J, Tolentino D.R., Cay, K.S., Gembicky, Jazzar, R., M., Bertrand, G., and Rinehart, J. D "Tuning electronic structure through halide modulation of mesoionic carbene cobalt complexes". *Dalton Trans.*, 2020, 49, 2426-2430. The dissertation author is the primary author of this publication. Reproduced by permission of The Royal Society of Chemistry

Chapter 3: Modeling the molecular magnetism of near-perfect octahedral Co(II) complexes with physically intuitive parameterization

3.1 Abstract

A central intuition in single-molecule magnetism is that a well-isolated, bistable ground state can be achieved by maximizing axial anisotropy. For a mononuclear transition metal complex, anisotropy is often best achieved by manipulating the strength and symmetry of the crystal field to generate mixing via the spin-orbit interaction. The resulting electronic structures defy simple description and chemical intuition is often sought using qualitative terms or in the extension of phenomenological spin Hamiltonians where the fitting parameters have limited or unclear physical significance. To study the consequences of these approximations, we describe the electronic structure of two nearly-perfect octahedral complexes, $[Co(MeCN)_6](PF6)_2$ and $[Co(DMSO)_6](BPh_4)_2$, using straightforward optical and magnetic characterization methods. Although these molecules manifest many of the same magnetic signatures, including slow magnetic relaxation (H_{DC} = 800 Oe) and large deviations from spin-only behavior, the use of crystal field parameters and the application of symmetry allows us to describe the magnetic and electronic behavior of these molecules with less reliance on phenomenological Hamiltonians. The inclusion of optical data provides a restriction on the fit that is much more in line with the energy scale of standard crystal field splittings, thus allowing the identification of unphysical parameters more easily. This approach allows for descriptions of the data that are consistent with the expected Co(II) ion spin-orbit coupling, empirically observed octahedral splitting, and mixing between the ^4F and ^4P states.

3.2 Introduction

Among first-row transition metal ions, octahedral divalent cobalt is well-known for its strong magnetic anisotropy.[117] This magnetic anisotropy, or preferred orientation of the ground state angular momentum, is a product of the spin-orbit coupling tethering the spin system to unquenched orbital moment.[118] Because of the comparable energy scales of Coulombic, crystal field, and spin-orbit Hamiltonian terms, these ions have some of the most complex electronic structures on the periodic table (Figure 6). This complexity requires a reserved approach to parameterization often leading to phenomenological Hamiltonians where, for example, orbital moments are accounted for using effective g values and mixing of angular momenta components are accounted for with zero-field splitting (ZFS) parameters. This parameterization is extremely successful for describing systems without large contributions from the orbital moment and even for highly anisotropic systems when high-field electron paramagnetic resonance (EPR) data are available. When only powder-average magnetometry data is available, the results become far less reliable and in highly anisotropic systems ZFS values can generally only be considered fitting parameters with limited physical meaning.[119] In order to provide some quantification to low-symmetry systems, magnetization data is often fit to the axial term of a ZFS Hamiltonian, with higher order terms added as necessary if allowed by symmetry and spin state.

With its high level of complexity and variability, it is unsurprising that researchers have found many methods to approach the problem of modeling molecular magnetism for the Co(II) ion. Notably, a Hamiltonian developed by Griffith and Figgis has had success in describing octahedral complexes that distort from perfect symmetry.[38, 120-122] This approach describes the mixing of ground and excited states of the d^7 ion using an orbital reduction factor which simplifies mixing and covalency into a singular term by assuming the orbital angular momentum of the ^4P excited state can be scaled from the ground $^4T_{1g}$ state. Using this approach, the calculations are greatly simplified and allow for any deviations from perfectly octahedral complexes to be fit using a distortion parameter. This method has been fairly successful in reproducing magnetic data, particularly with a method developed by the Pardo group;[22] however, the lack of physical significance is still elusive due to oversimplification or overparameterization.

Herein we explore the fitting results of various perturbation approaches in systems with relatively high symmetry allowing us to probe the propensity of solutions with dubious physical meaning. The previously reported complexes $[Co(DMSO)_6](BPh_4)_2$[123] and $[Co(MeCN)_6](PF_6)_2$[124]. provide particularly striking examples where acceptable fits on magnetic data to various Hamiltonians can be found but meaning is practically limited due to the many correlated fitting parameters. Sakiyama et al. analyzed the static magnetic

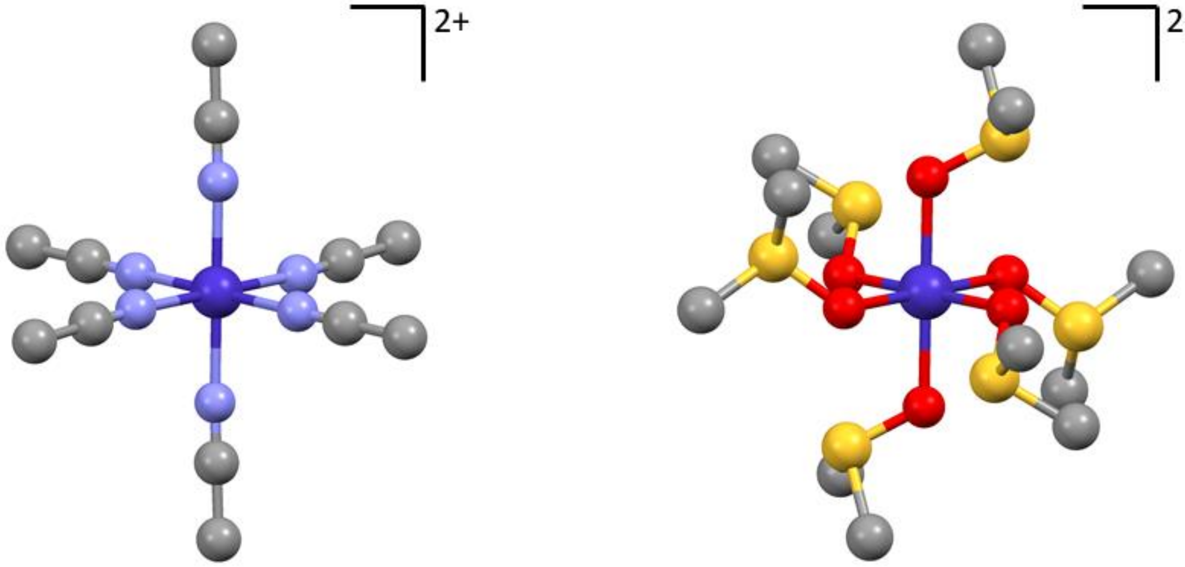

Figure 24: Crystal structures of $[Co(MeCN)_6]^{+2}$ (left) and $[Co(DMSO)_6]^{+2}$ (right). Respective counter ions not shown.

properties of the DMSO adduct using the TP equivalence method described by Griffith and Figgis.[123] Analysis of this compound focused on axial and rhombic distortion parameters which led to good fits of the magnetic data. Additionally, the Dunbar group recently reported[125] a study on the acetonitrile adduct which employed a similar approach using spin-orbit coupling in tandem with axial (B_2^0) and transverse (B_2^2) crystal field parameters to describe this system. Both approaches use phenomenological terms to overcome the challenge of the complexities of multiple interactions of similar energy. While the employment of crystal field parameters allows for good mathematical fits which can be used to study and compare magnetic data, physical significance of parameters eludes this approach. The use of only two crystal field parameters leads to incomplete pictures of the electronic structure which is a byproduct of analysis that is limited by the sole use of magnetic data in their fits. Given our observations of slow magnetic relaxation under an applied field in highly symmetric, simple solvent adducts of Co(II), we attempted to develop a new approach to fitting magnetic data using simple magnetometry and absorption spectroscopy to model the magnetic properties and electronic structure on the basis of crystal field theory using PHI, a software package developed by the Chilton group.[17] This approach allows for results with some limited physical significance, and importantly, results obtained by fitting can be checked through comparisons to spectroscopic data.

3.3 Materials and General Methods

Experimental Procedure

All chemicals were purchased from commercial sources unless otherwise noted. Acetonitrile and DMSO were dried over a mixture of activated 3Å and 4Å molecular sieves.

Synthesis of $[Co(MeCN)_6](PF_6)_2$ was adapted from that of $[Co(MeCN)_6](BF_4)_2$ as described by Dunbar and coworkers.[124] Under dinitrogen atmosphere, acetonitrile (20 mL) was added dropwise to a mixture of $NOPF_6$ (1.0 g, 5.7 mmol) and Co powder in excess (2.0 g, 34 mmol). Effervescence was immediately observed. After completion of the addition, dissolved NO was removed under reduced pressure (10^{-1} torr) and the mixture was stirred at room temperature for 12 h. The resulting peach/pink solution was centrifuged, and the supernatant extracted with acetonitrile and concentrated under vacuum. Peach-pink crystals suitable for single-crystal X-ray diffraction analysis and magnetometry measurements were grown from vapor diffusion of Et_2O into acetonitrile. CHN elemental analysis was performed by Midwest Microlabs. CHN (measured, projected) C: 23.64, 24.22 H: 5.78, 3.05 and N: 12.68, 14.12. Synthesis of $[Co(DMSO)_6](BPh_4)_2$ was adopted from a synthesis reported by Sakiyama.[126] Briefly, Co(II) nitrate hexahydrate (1.0 g, 3.4 mmol) was refluxed in 2.0 mL of DMSO for one hour in the presence of $NaBPh_4$ (2.4 g, 6.8 mmol) with precipitation of purple crystals upon cooling. Purple crystals suitable for single-crystal X-ray diffraction analysis were grown upon recrystallization from a minimal amount of DMSO consistent with literature procedure.

Physical Measurements

Single crystal X-ray diffraction data were collected at T = 100 K on a Bruker κ Diffractometer with a Mo Kα radiation source and an Apex II Area Detector. The structure was solved using Olex[2] [93] via the SHELXT[94] routine and refined using full-matrix least-squares procedures with SHELXL.[95] Magnetic data were collected using a Quantum Design Magnetic Properties Measurements System (MPMS3) Superconducting Quantum

Interference Device (SQUID) Magnetometer in Direct Current (DC) scan mode. Magnetic measurements were performed on randomly oriented, crushed microcrystalline samples interspersed in the inert wax eicosane to provide thermal bath contact and prevent crystallite torquing at high field. Samples were sealed under vacuum in a custom quartz tube with a thin shelf to designed to avoid end effects (i.d. = 4 mm; D & G Glassblowing Inc.). All data were corrected for diamagnetism using Pascal's constants.[96] UV-Vis absorption spectroscopic data was collected as acetonitrile or DMSO solutions in quartz cuvettes using an Agilent Cary 5000 UV-Vis-NIR spectrometer.

3.4 Results and Discussion

$[Co(MeCN)_6](PF_6)_2$ crystallizes in the $R\overline{3}$ space group. The metal complex sits on a site of $\overline{3}m(D_{3d})$ symmetry described by equivalent Co – N bonds (d = 2.110 Å) and a 1.8° trigonal distortion from O_h. This negligible distortion is rare among homoleptic, octahedral Co(II) complexes with electronic degeneracy; typically, octahedral complexes are subject to Jahn-Teller distortions that give rise to D_{4h} symmetry.[117] Using the SHAPE software which measures distortions from perfect polyhedron,[127-129] the inner-coordination sphere of the solid-state complex is perfectly octahedral up to the level of accuracy provided by this measurement with the distortion from a perfect octahedron measuring at 0.00000 (Table 4).

Table 4: Deviations in geometry for $[Co(MeCN)_6]^{+2}$ calculated from ideal six-coordinate structures

$[Co(MeCN)_6]^{+2}$		
Ideal Structures	Description	Deviation
HP-6	Hexagon	33.33322
PPY-6	Pentagonal pyramid	30.43692
OC-6	Octahedron	0.00000
TPR-6	Trigonal Prism	16.73672
JPPY-6	Johnson pentagonal pyramid	34.02824

Table 5: Deviations in geometry for $[Co(MeCN)_6]^{+2}$ calculated from ideal six-coordinate structures

$[Co(DMSO)_6]^{+2}$		
Ideal Structures	Description	Deviation
HP-6	Hexagon	32.38670
PPY-6	Pentagonal pyramid	28.34593
OC-6	Octahedron	0.18643
TPR-6	Trigonal Prism	15.31632
JPPY-6	Johnson pentagonal pyramid	31.59745

The crystal structure of $[Co(DMSO)_6](BPh_4)_2$ used for magnetic data collection was consistent with the reported structure, crystallizing in the $P\bar{1}$ space group with anisotropic trigonal distortions of approximately 3.2°. The DMSO adduct shows a Jahn-Teller elongation along one axis of the CoO_6 core, with two bond lengths of 2.219 Å compared to a range of 2.065 – 2.094 Å for the other distances. Performing the same continuous SHAPE measurement as the acetonitrile adduct, the CoO_6 core was measured as a near-perfect octahedron with a 0.18643 measured distortion. The next closest geometry, trigonal prismatic, had a SHAPE parameter of 15.31632.

In the absence of an applied DC field, neither $[Co(MeCN)_6]^{+2}$ nor $[Co(DMSO)_6]^{+2}$ showed any notable dynamic magnetic properties; however, upon the application of a field, both complexes showed measurable frequency dependence, as shown in Figure 25 and Figure 26 for $[Co(MeCN)_6]^{+2}$ as well as Figure 27 and Figure 28 for $[Co(DMSO)_6]^{+2}$. The in-phase and out-of-phase components vs. frequency were fit simultaneously with a generalized Debye equation (Equation 3.1).[118]

$$\tau^{-1} = \tau_0^{-1} \exp\left(-\frac{U_{\mathrm{eff}}}{k_B T}\right) + CT^{n} \tag{3.1}$$

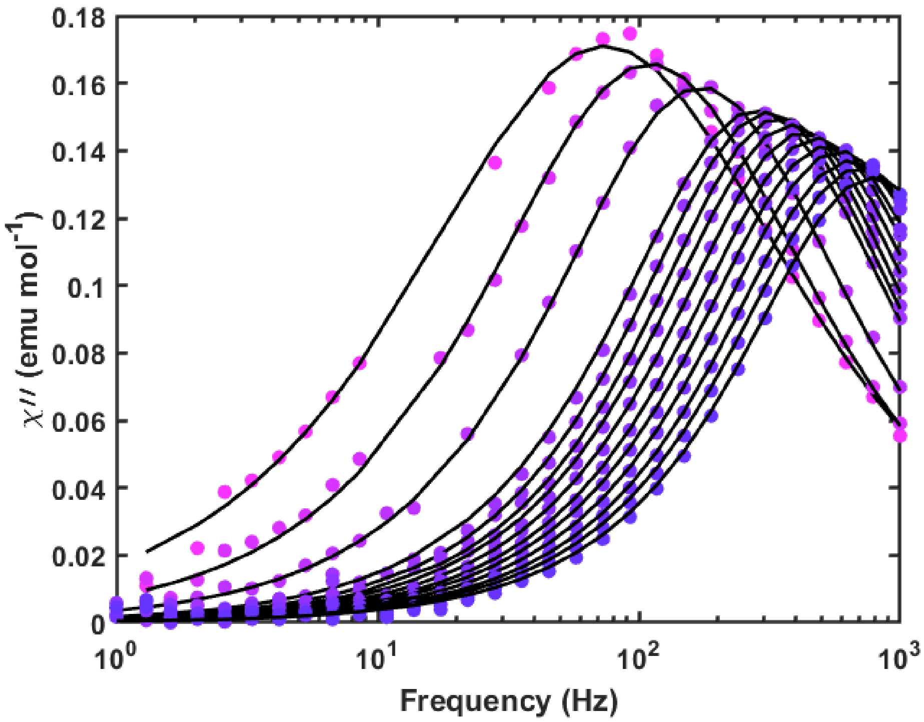

Figure 25: Out-of-phase AC susceptibility vs Frequency of $[Co(MeCN)_6](PF_6)_2$ under an applied DC field of 800 Oe

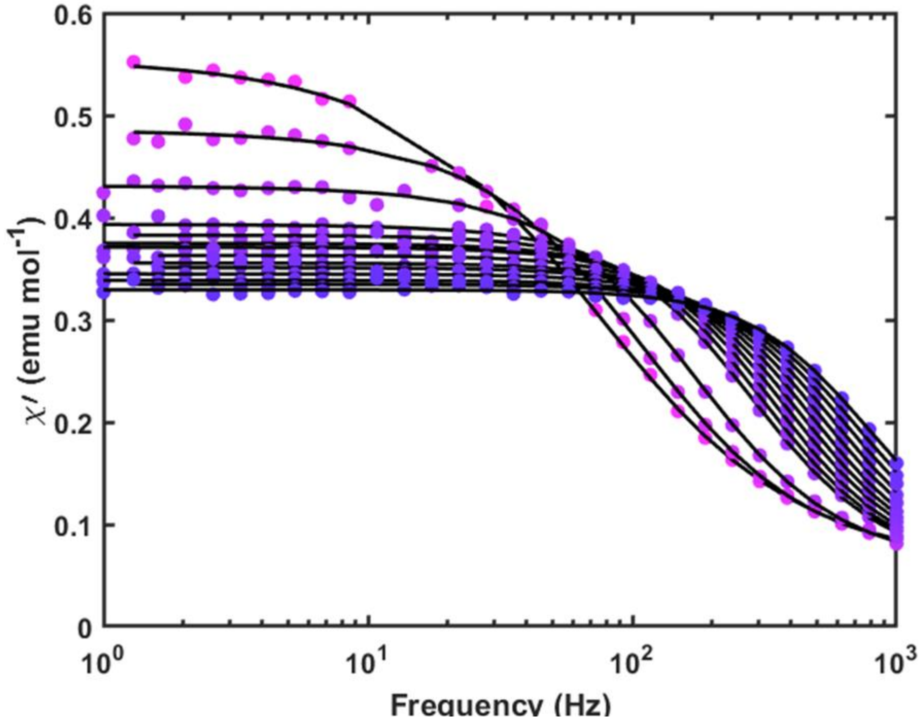

Figure 26: In-phase AC susceptibility vs Frequency of $[Co(MeCN)_6](PF_6)_2$ under an applied DC field of 800 Oe

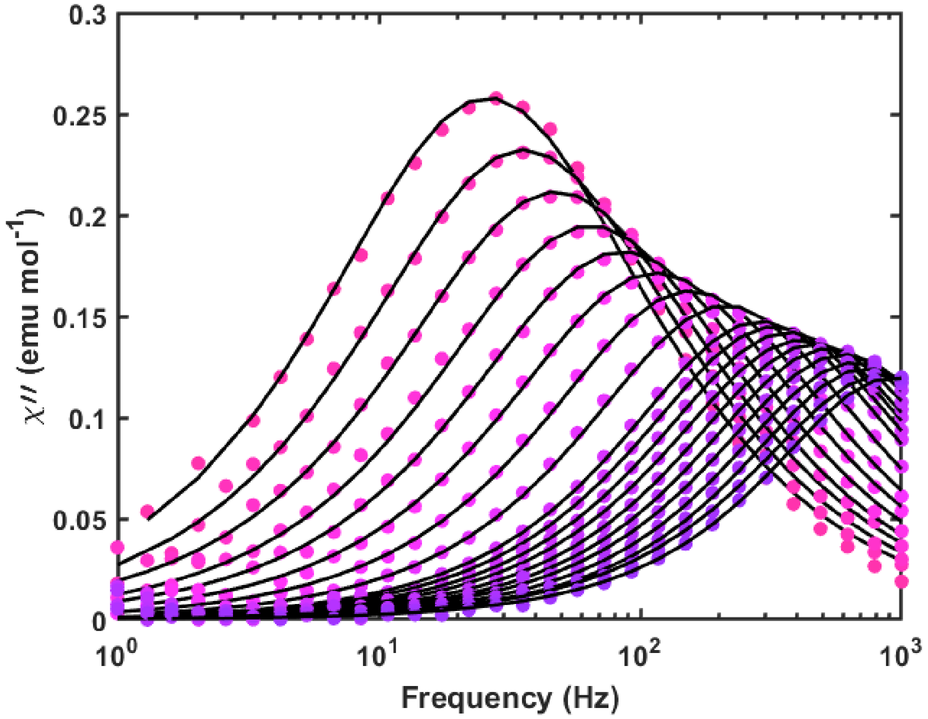

Figure 27: Out-of-phase AC susceptibility vs Frequency of [Co(DMSO)$_6$](BPh$_4$)$_2$ under an applied DC field of 800 Oe

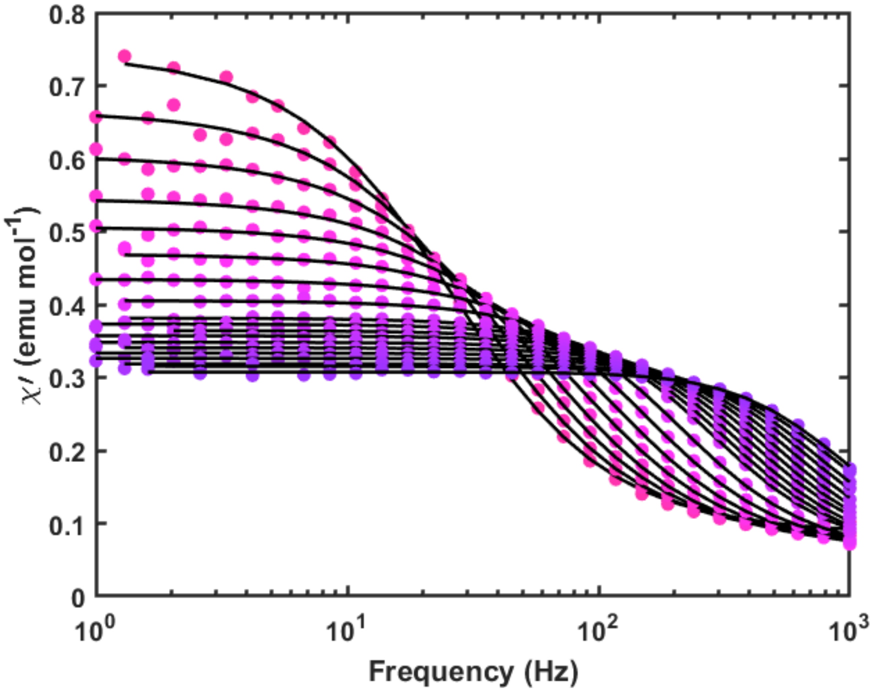

Figure 28: In-phase AC susceptibility vs Frequency of [Co(DMSO)$_6$](BPh$_4$)$_2$ under an applied DC field of 800 Oe

This form of the generalized Debye equation has two terms, the first being an Orbach or over barrier process ($\tau_0^{-1} \exp\left(-\frac{U_{eff}}{k_B T}\right)$), and the second being a Raman or vibrationally-coupled process (CT^n). Data were fit to Orbach and Raman/vibrationally-coupled processes although the low barrier (U_{eff}) and relatively small measurement range preclude drawing concrete conclusions as to the nature and number of these processes. The χ' (in-phase) and χ'' (out of phase) dependency plots vs frequency and temperature were collected with an applied DC field of 800 Oe and peaks were plotted in an Arrhenius-like plot (Figure 29 and Figure 30). The higher temperature region was dominated by an Orbach process while at lower temperatures, Raman relaxation effects become the fastest available mechanism.

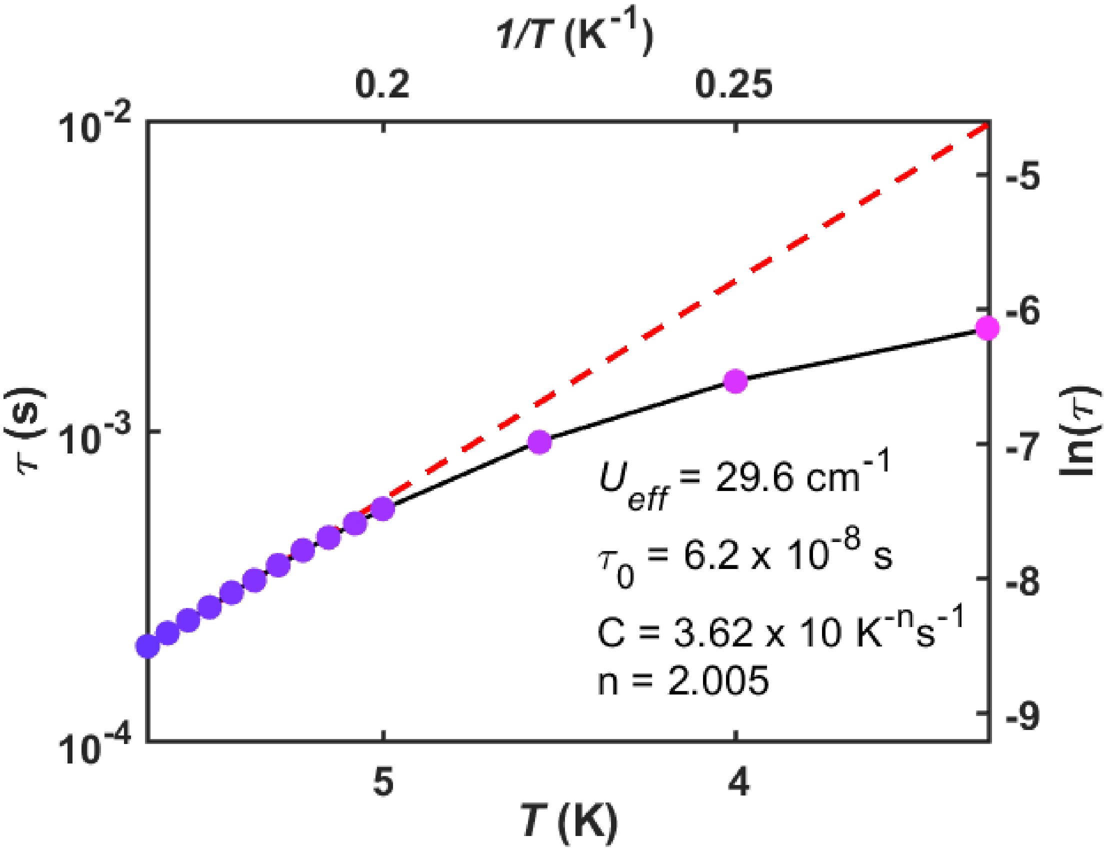

Figure 29: Arrhenius plots of relaxation times versus temperature for $[Co(MeCN)_6](PF_6)_2$ Black lines are fits to a multi-term relaxation model, Equation 3.1, while the dashed red line represents the Orbach-only fit

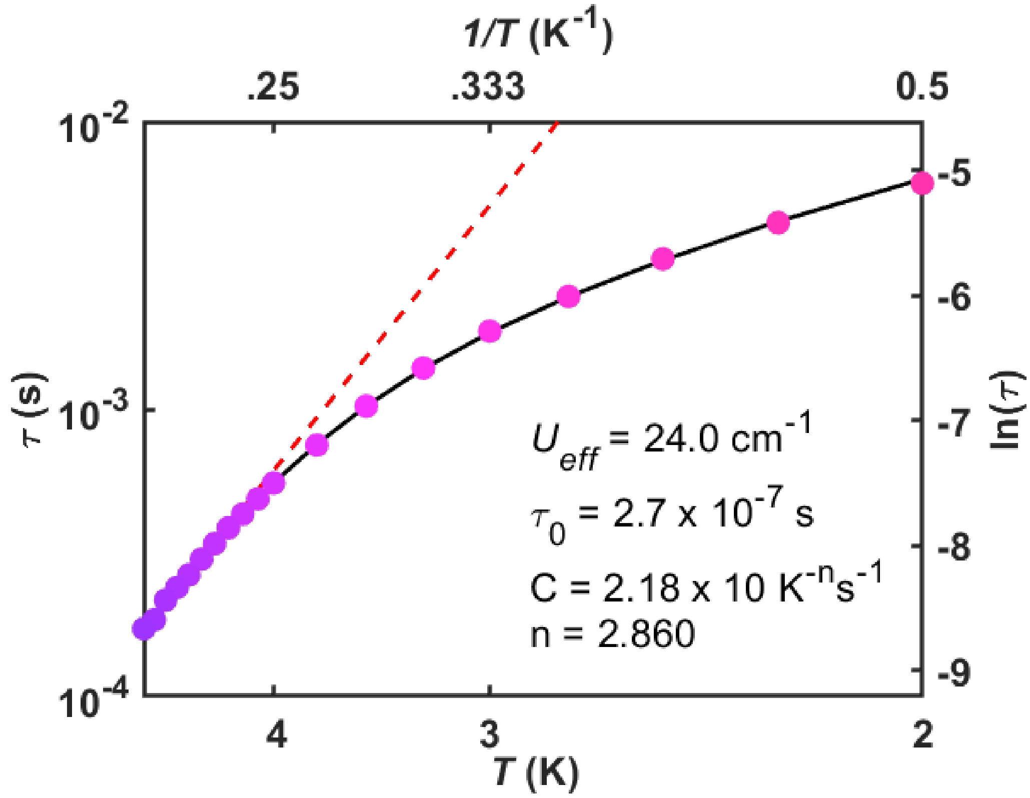

Figure 30: Arrhenius plots of relaxation times versus temperature for $[Co(DMSO)_6](PF_6)_2$ Black lines are fits to a multi-term relaxation model, Equation 3.1, while the dashed red line represents the Orbach-only fit

Using these processes to fit the relaxation behavior gave an attempt time for the acetonitrile adduct of $\tau_0 = 6.2 \times 10^{-8}$ s, effective barrier (U_{eff}) of 29.6 cm^{-1}, and a Raman relaxation constant of $C = 3.62 \times 10^1$ $K^{-n}s^{-1}$ with n = 2.005 (Figure 29). The DMSO adduct was fit with $\tau_0 = 2.7 \times 10^{-7}$ s, U_{eff} of 24.0 cm^{-1}, and $C = 2.18 \times 10^1$ $K^{-n}s^{-1}$ with $n = 2.860$ (Figure 30). Although these results are important to note, the significance of the parameters of this fit are not the focus of this paper and are more thoroughly discussed in other works in the literature.[116]

Temperature dependence of the magnetic susceptibility (χT vs. T) for both complexes was studied between $T = 1.8$ and 300 K under a bias field of $H_{DC} = 1000$ Oe. At room temperature, $\chi_M T$ values of 3.30 and 3.05 emu K mol^{-1} were found for the MeCN

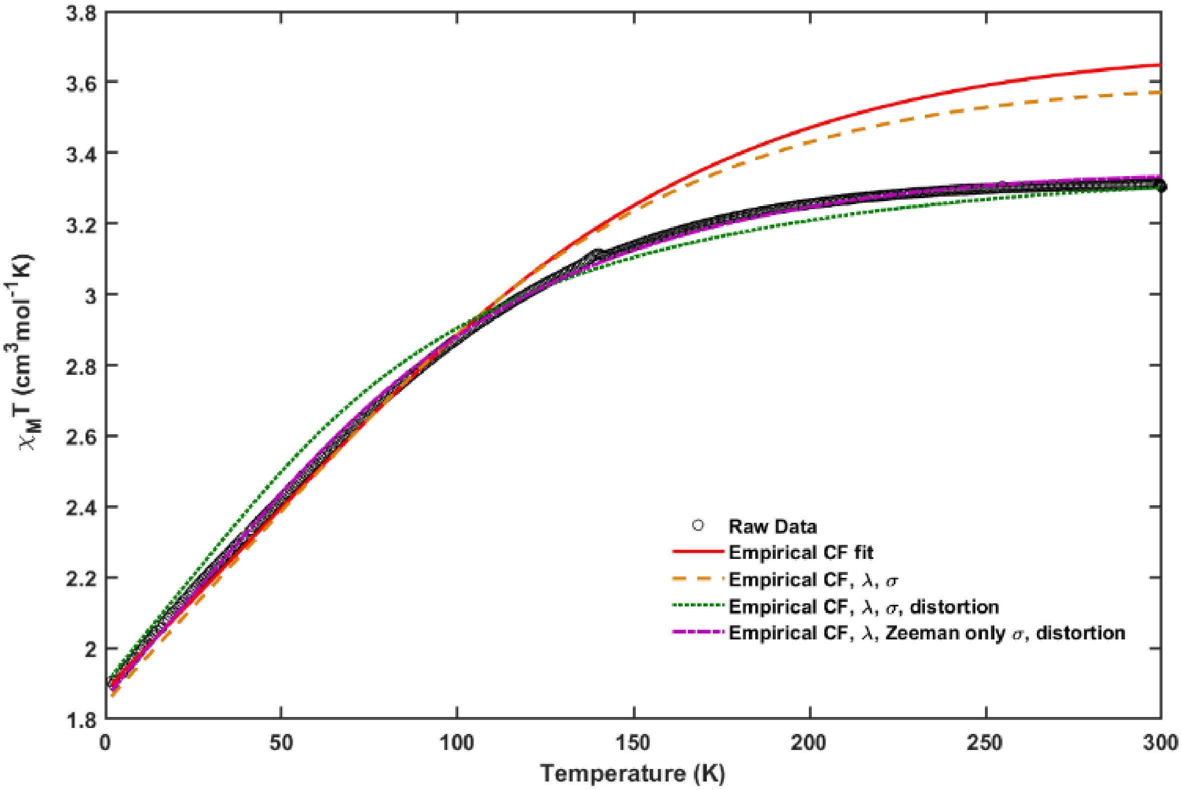

Figure 31: Temperature independent magnetic susceptibility of $[Co(MeCN)_6](PF_6)_2$ (black) with fits using subsequent perturbations containing empirical CF fits (red line), spin-orbit coupling and orbital reduction (dashed orange line), symmetry-lowering distortion (dotted green line), and applying orbital reduction to only the orbital reduction factor (dash-dot purple line)

(Figure 31) and DMSO (Figure 32) analogs respectively which exceeds the spin-only value of $\chi_M T$ = 1.875 emu K mol^{-1}. The $\chi_M T$ values for both complexes decline minimally until approximately T = 250 K, at which point the decline accelerates, eventually reaching minimum values of $\chi_M T$ = 1.91 and 1.71 emu K mol^{-1} at 1.8 K for the MeCN and DMSO analogs, respectively. Field-cooled and zero-field-cooled data were superimposable, indicating that relaxation was fast enough to equilibrate the system on the timescale of DC data collection. As reported by Sakiyama,[123] we also observed a notable dip in the susceptibility of the DMSO analog at around 240 K, attributable to a change in crystal

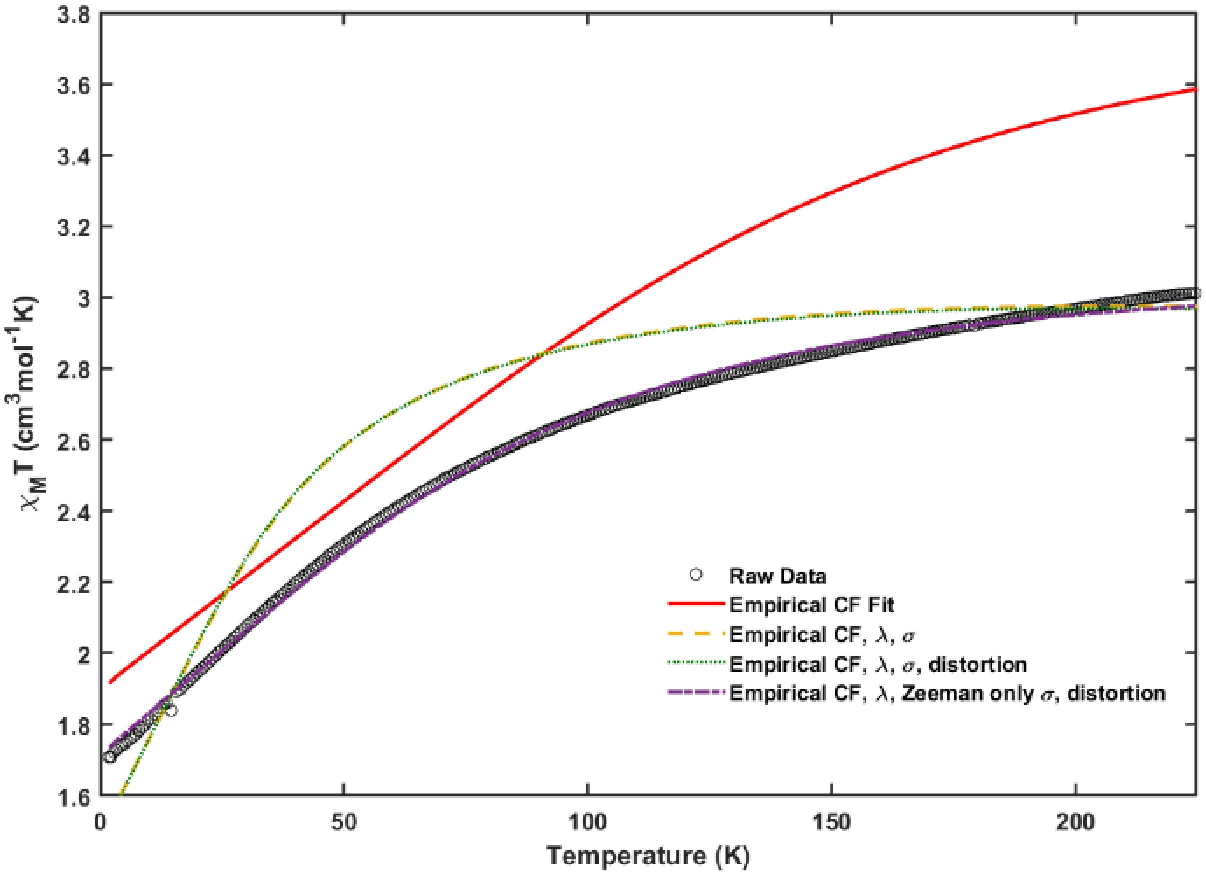

Figure 32: Temperature independent magnetic susceptibility of $[Co(DMSO)_6](BPh_4)_2$ (black) with fits using subsequent perturbations containing empirical CF fits (red line), spin-orbit coupling and orbital reduction (dashed orange line), symmetry-lowering distortion (dotted green line), and applying orbital reduction to only the orbital reduction factor (dash-dot purple line)

structure, therefore all modelling on the DMSO analog was done using data below this dip. Multiple models were employed to fit this data, these will be discussed below.

To probe the low-lying electronic structure, magnetization vs. field data were also collected in the region of non-linearity (1.8 K < T < 7 K) with larger intervals up to 300K (Figure 33-Figure 40). As expected from the dynamic data observations, magnetic hysteresis was not observed in either system. Modelling on this data was done in conjunction with the susceptibility data, this will also be discussed below.

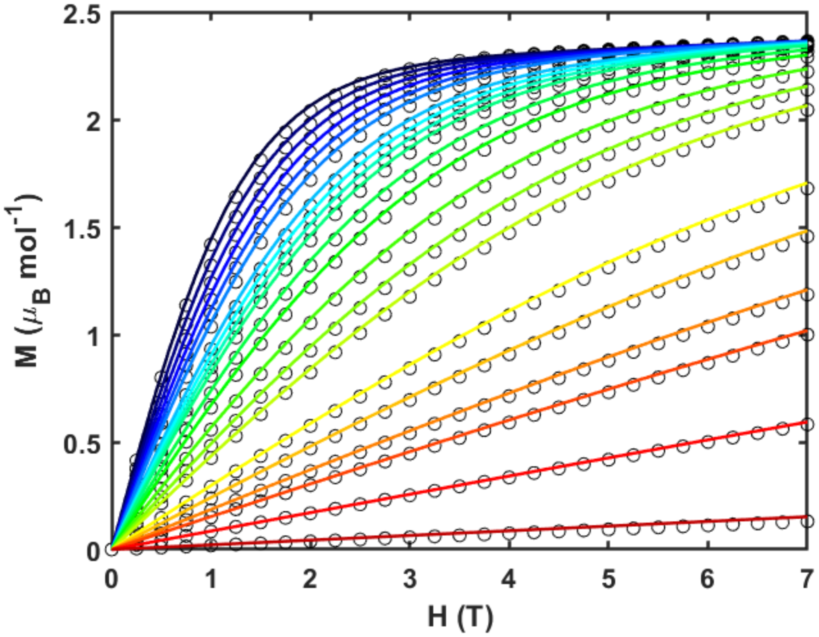

Figure 33: Magnetization data (black circles) of $[Co(MeCN)_6](PF_6)_2$ fit using empirically derived crystal field data using the B_4^0 term. Data and fits range from 1.8 K (dark blue) to 300 K (dark red).

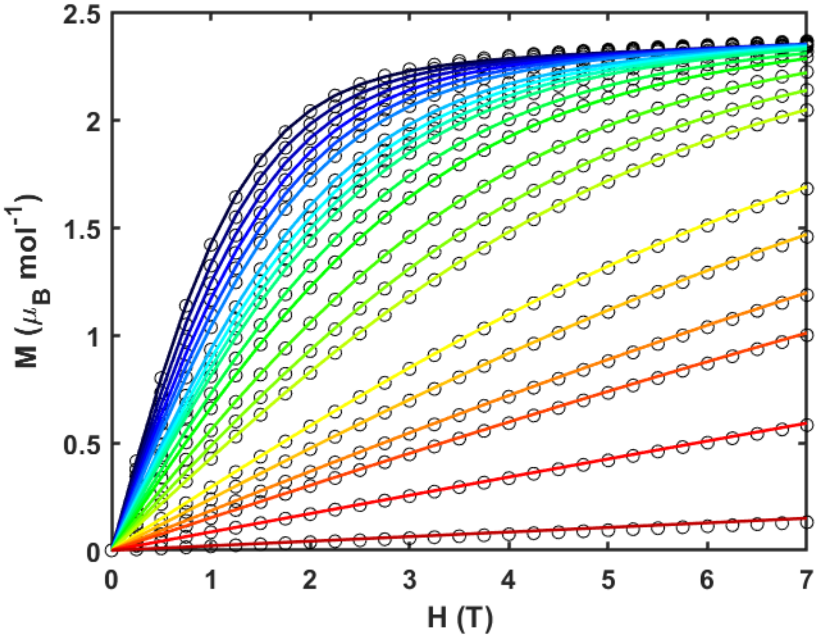

Figure 34: Magnetization data (black circles) of $[Co(MeCN)_6](PF_6)_2$ fit using empirically derived crystal field data using the B_4^0 term and spin-orbit coupling. Data and fits range from 1.8 K (dark blue) to 300 K (dark red).

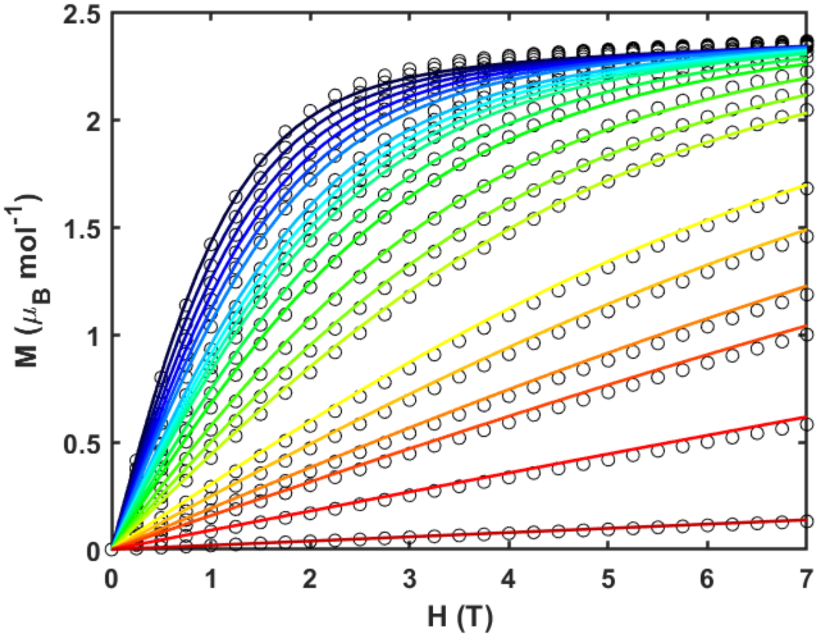

Figure 35: Magnetization data (black circles) of $[Co(MeCN)_6](PF_6)_2$ fit using empirically derived crystal field data using the B_4^0 and B_4^3 terms as well as spin-orbit coupling. Data and fits range from 1.8 K (dark blue) to 300 K (dark red).

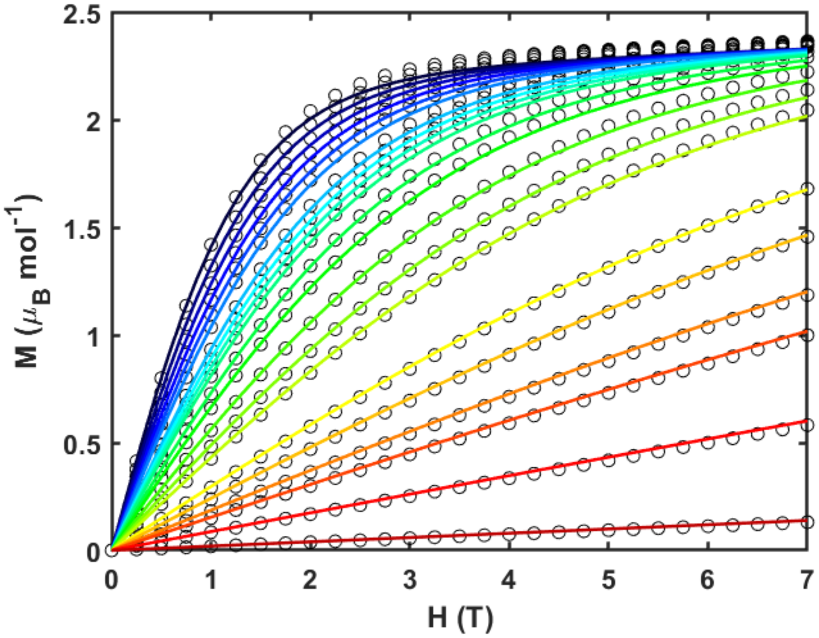

Figure 36: Magnetization data (black circles) of $[Co(MeCN)_6](PF_6)_2$ fit using empirically derived crystal field data using the B_4^0 and B_4^3 terms as well as spin-orbit coupling, restricting the orbital reduction term to the Zeeman effect. Data and fits range from 1.8 K (dark blue) to 300 K (dark red).

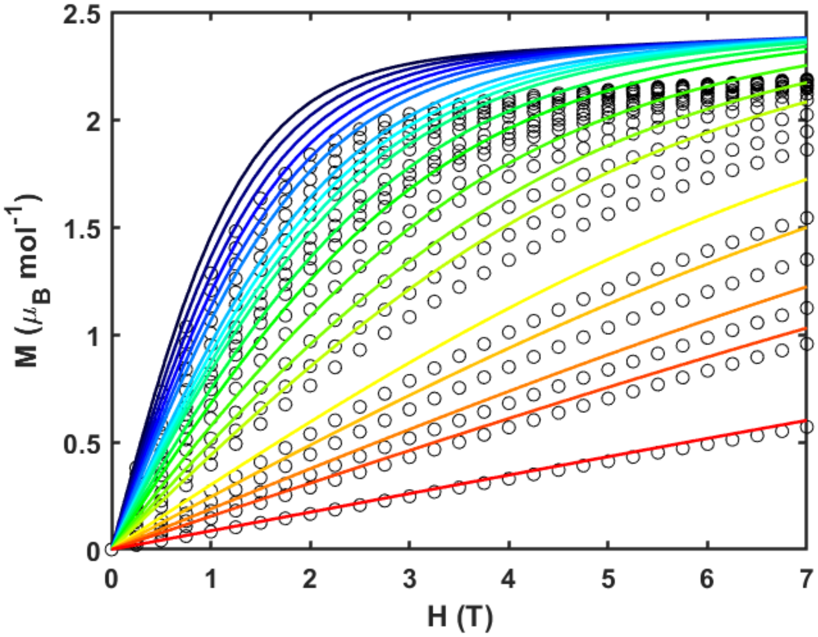

Figure 37: Magnetization data (black circles) of $[Co(DMSO)_6](BPh_4)_2$ fit using empirically derived crystal field data using the B_4^0 term. Data and fits range from 1.8 K (dark blue) to 300 K (dark red).

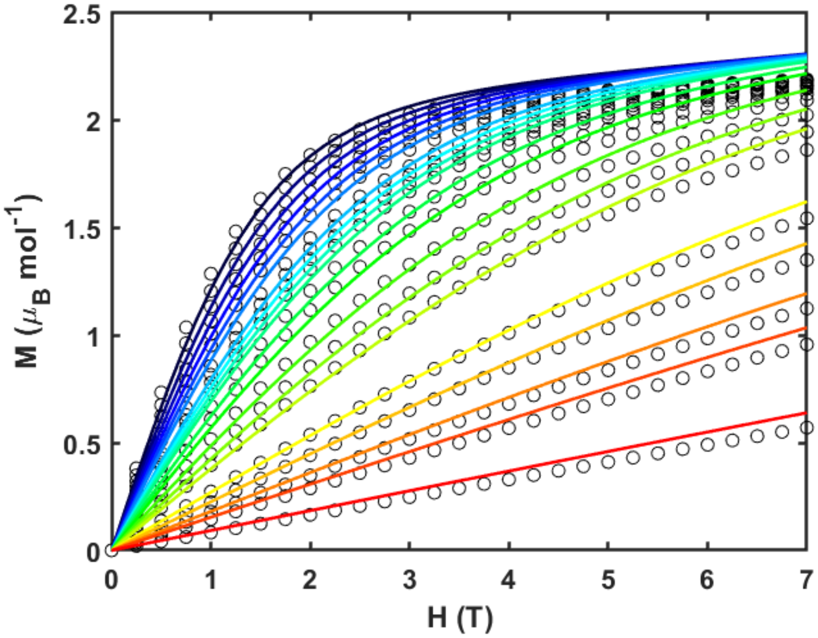

Figure 38: Magnetization data (black circles) of $[Co(DMSO)_6](BPh_4)_2$ fit using empirically derived crystal field data using the B_4^0 term and spin-orbit coupling. Data and fits range from 1.8 K (dark blue) to 300 K (dark red).

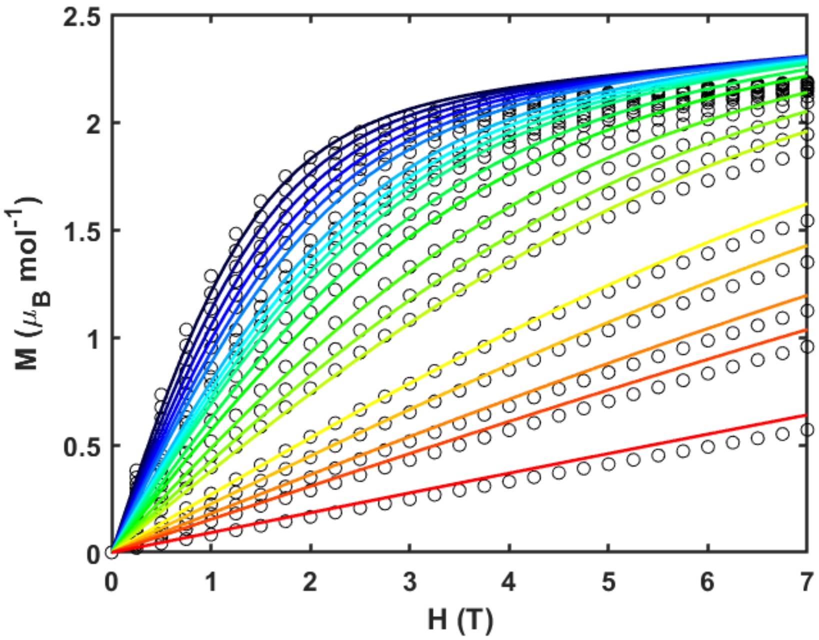

Figure 39: Magnetization data (black circles) of [Co(DMSO)$_6$](BPh$_4$)$_2$ fit using empirically derived crystal field data using the B_4^0 and B_4^3 terms as well as spin-orbit coupling. Data and fits range from 1.8 K (dark blue) to 300 K (dark red).

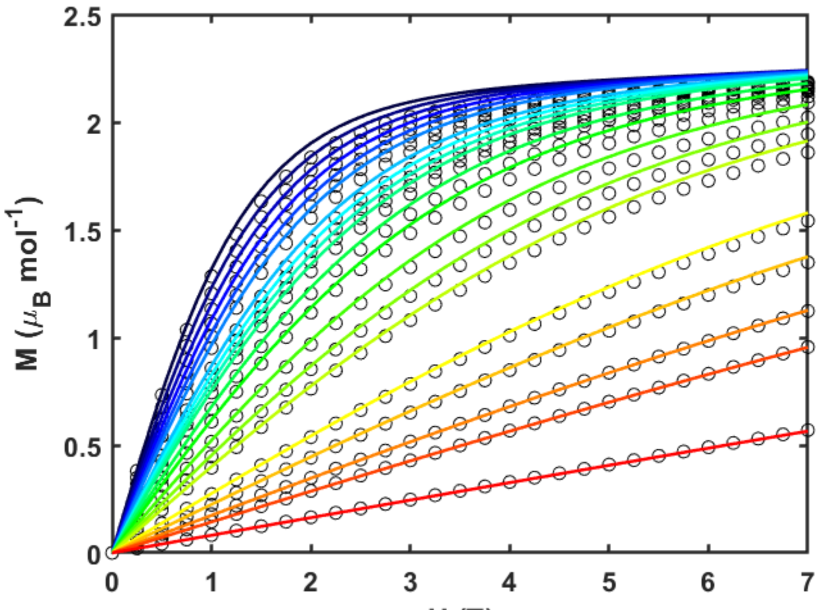

Figure 40: Magnetization data (black circles) of [Co(DMSO)$_6$](BPh$_4$)$_2$ fit using empirically derived crystal field data using the B_4^0 and B_4^3 terms as well as spin-orbit coupling, restricting the orbital reduction term to the Zeeman effect. Data and fits range from 1.8 K (dark blue) to 300 K (dark red).

UV-Vis-IR spectroscopy was used to roughly determine the electronic excited energy states of the two complexes. The ligand field splitting of an octahedral or nearly octahedral Co(II) complex is well-described using only the d-d transitions appearing within the UV/visible/near IR energy range. Three prominent spin-allowed transitions are expected from excitations of the ${}^4T_{1g}({}^4F)$ ground state to the ${}^4T_{2g}({}^4F)$, ${}^4A_{2g}({}^4F)$, and ${}^4T_{1g}({}^4P)$ excited states (Figure 5). These states provide an empirical basis for the octahedral crystal field terms such that the parameter space can be significantly reduced. This is vital as the spin orbit coupling results in a significant increase in complexity.[22] To assess the energy of the excited d-electron states in our systems, absorption

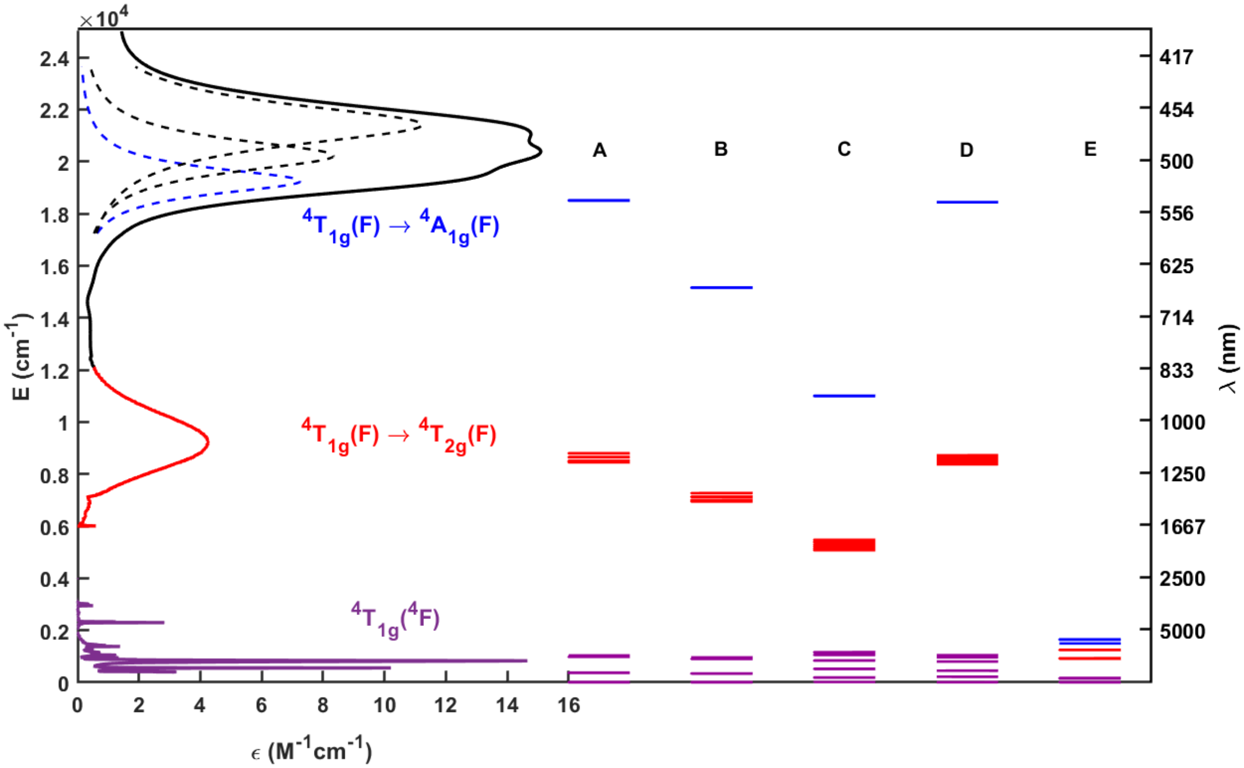

Figure 41: On the left is shown the solution-state UV-Vis-NIR spectroscopic data of $[Co(MeCN)_6](PF_6)_2$ supplemented by lower-energy ATR-IR data (normalized scale). To the right of this figure are energy states generated in simulations in PHI showing the splitting of the ${}^4T_{1g}({}^4F)$ ground state (purple) from the first set of excitations in the ${}^4T_{2g}({}^4F)$ state (red) and the second set of excitations ${}^4A_{1g}({}^4F)$ state (blue). The figures show progressive perturbations on the Co(II) ion with A using the empirically derived B_4^0 term, B including spin-orbit coupling and orbital reduction terms, C including a B_4^3crystal field term, and D restricting orbital reduction to acting only on the Zeeman component of the Hamiltonian. The fifth simulation, E, employs the Hamiltonian used in the literature description of this complex.

spectra were collected in acetonitrile and DMSO solutions (λ = 250 – 1500 nm) as well as solid-state ATR-IR spectra. As previously reported,[130] the absorption (Figure 41) for the acetonitrile adduct centered at λ = 1091 nm (9116 cm^{-1}) corresponds to the $v_1 = {}^4T_{1g}({}^4F) \rightarrow {}^4T_{2g}({}^4F)$ transition, while the three-feature peak contains the $v_2 = {}^4T_{1g}({}^4F) \rightarrow {}^4A_{2g}({}^4F)$ transition and the $v_3 = {}^4T_{1g}({}^4F) \rightarrow {}^4T_{1g}({}^4P)$ transition. To determine which peak corresponds to which transition, we employed peak fitting of the spectra to determine a 3-peak best fit of the data. The peaks of best fit were found at $E/\hbar c =$ 19250, 20222, and 21408 cm^{-1}, and used to estimate a Racah B parameter and Dq value via a d^7 Tanabe-Sugano diagram.[35] Assuming the two peaks of higher energy were the result of a solution based distortion which would split the triplet term, we assigned the $v_3 = {}^4T_{1g}({}^4F) \rightarrow {}^4T_{1g}({}^4P)$ transition as the average of these two peaks, while the $v_2 = {}^4T_{1g}({}^4F) \rightarrow {}^4A_{2g}({}^4F)$ transition was assigned to the peak centered at 19250 cm^{-1} (519 nm). Using these values, we obtained values of B = 862 cm^{-1} and Dq = 989 cm^{-1}.

The DMSO analog has a similar spectrum with a bathochromic shift for all peaks as shown in Figure 41; however, the solution-based distortion only resulted in the appearance of two prominent features in the visible region which were used to calculate crystal field parameters. The $v_1 = {}^4T_{1g}({}^4F) \rightarrow {}^4T_{2g}({}^4F)$ transition was assigned to the peak centered at 7200 cm^{-1} (1389 nm), with the $v_2 = {}^4T_{1g}({}^4F) \rightarrow {}^4A_{2g}({}^4F)$ transition centered at 18474 cm^{-1} (541 nm) and the $v_3 = {}^4T_{1g}({}^4F) \rightarrow {}^4T_{1g}({}^4P)$ transition centered at 20482 cm^{-1} (488 nm). Analysis via the Tanabe-Sugano diagram yields the Racah parameter B = 959 cm^{-1} and a Dq value of 829 cm^{-1}.

To fit the magnetometry data, we employed the Hamiltonian in Equation 3.2:

$$\hat{H} = \sigma\lambda\vec{\hat{L}}\cdot\vec{\hat{S}} + \sum_{i=1}^{N}\sum_{k=2,4,6}\sum_{q=-k}^{k}\sigma_i^k B_{ki}^q \theta_k \hat{O}_{ki}^q + \mu_B\left(\sigma\vec{\hat{L}}_i\cdot\bar{\bar{\mathrm{I}}} + \vec{\hat{S}}_i\cdot \mathrm{g}\bar{\bar{\mathrm{I}}}\right)\cdot\vec{B} \tag{3.2}$$

where σ is the orbital reduction factor, λ is the spin-orbit coupling parameter, $\vec{\hat{L}}$ and $\vec{\hat{S}}$ are orbit and spin respectively, $B_{ki}^{q}\theta_k\hat{O}_{ki}^{q}$ are the crystal field parameters with their associated Stevens operators, μ_B is the Bohr magneton, $\bar{\bar{I}}$ is the identity matrix of appropriate dimensionality, g is the Landé *g* factor, and $\vec{B}$ is the external magnetic field. This Hamiltonian can be broken up into three main

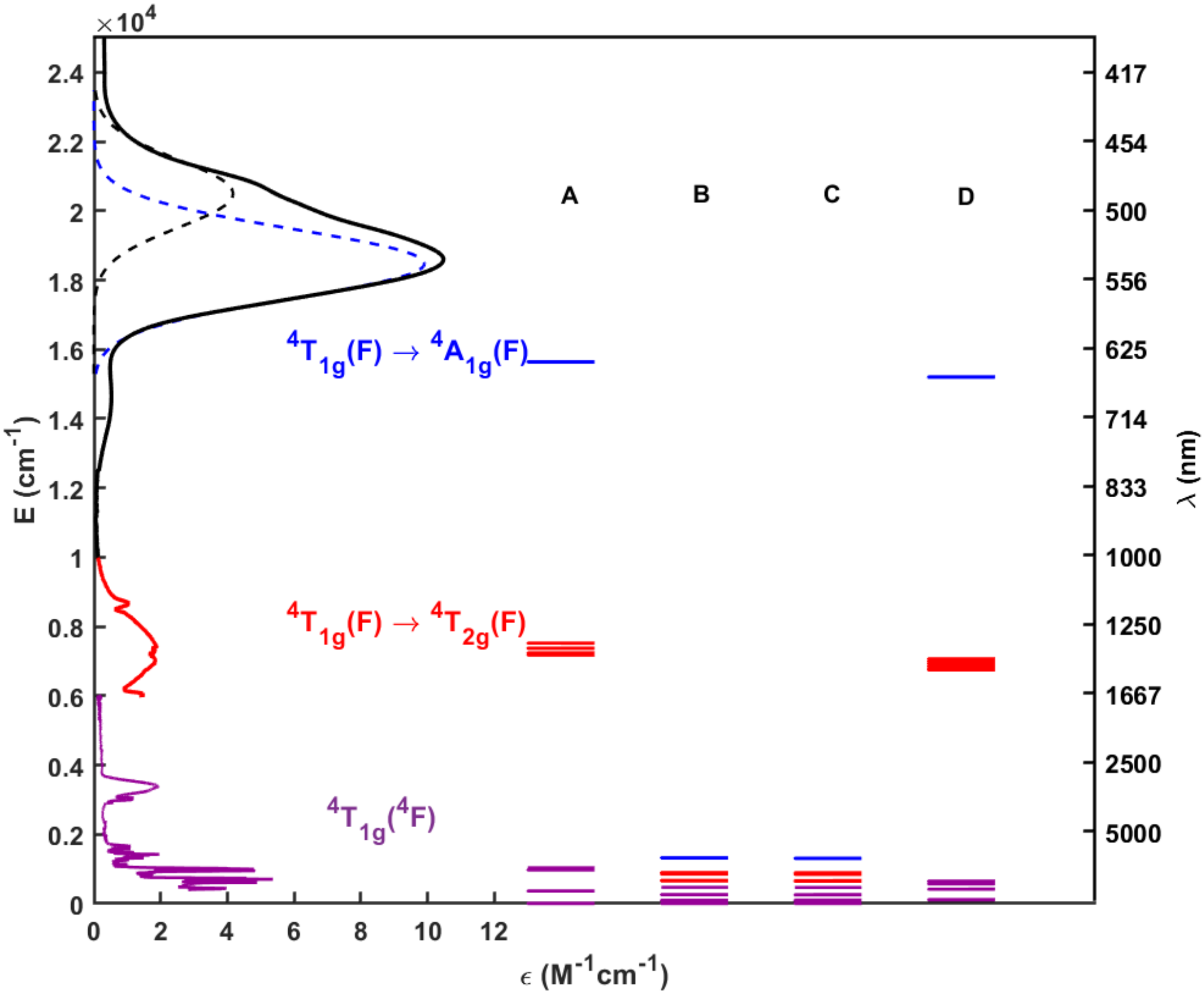

Figure 42: On the left is shown the solution-state UV-Vis-NIR spectroscopic data of $[Co(MeCN)_6](PF_6)_2$ supplemented by lower-energy ATR-IR data (normalized scale). To the right of this figure are energy states generated in simulations in PHI showing the splitting of the $^4T_{1g}(^4F)$ ground state (purple) from the first set of excitations in the $^4T_{2g}(^4F)$ state (red) and the second set of excitations $^4A_{1g}(^4F)$ state (blue). The figures show progressive perturbations on the Co(II) ion with A using the empirically derived B_4^0 term, B including spin-orbit coupling and orbital reduction terms, C including a B_4^3crystal field term, and D restricting orbital reduction to acting only on the Zeeman component of the Hamiltonian. The fifth simulation, E, employs the Hamiltonian used in the literature description of this complex

parts with the first term containing the spin-orbit coupling, the second term containing the crystal field parameters, and the third encompassing the Zeeman effect. The use of this Hamiltonian for the modelling of magnetic data in octahedral Co(II) provides several advantages. First, the inclusion of the first term allows a more accurate representation of the perturbation caused by the presence of first-order orbital angular momentum in near-perfect octahedral Co(II) systems. Secondly, the modelling of the crystal field terms can be guided by optical spectroscopy using conversion factors from Dq giving physical checks on the magnitudes of each crystal field term. Lastly, this model allows us to probe a large temperature space, with multiple states contributing to the magnetic properties observed while using an isotropic g factor.

Magnetization data and molar susceptibility were modeled using crystal field parameters derived from UV-Vis spectroscopy utilizing the PHI program developed by the Chilton Group.[17] Using the crystal-field parameters defined by Ballhausen[40] and converting them to a usable form in PHI through the conversions found in Mulak and Gajek[12] the energy splitting of both adducts were modeled in tandem with the magnetic data. The resulting value was used as the crystal field acting on the free ion with PHI. For the acetonitrile adduct, this crystal field value (B_4^0 = 2596 cm^{-1}) gives energy splittings that are in good agreement with the excitations seen in the spectroscopic data (Figure 41A) correlating with the first two excitations in the ^4F ground state but does not give the third d-d excitation to the ^4P state as calculation of this state is not included in the basis utilized by the PHI software. Additionally, this fit models the magnetization data quite well (Figure 33); however, it failed to properly model the susceptibility at higher temperatures (Figure 31). To address this, the spin-orbit coupling and orbital reduction were fit in PHI to give fit values of $\lambda = -167.0$ and $\sigma = 0.95$. Although this method gave a better fit of the magnetic data (Figure 34) and the energy diagram was somewhat consistent with the spectroscopic data (Figure 41B), it still struggled to model the susceptibility at high temperatures. We then included a reduction of symmetry by including the B_4^3 term in PHI in tandem with the spin-orbit and orbital reduction terms. Fitting these three parameters simultaneously gave $\lambda = -171.5$, $\sigma = 0.87$, and a trigonal distortion value of -3961 cm^{-1}. This series of fits seemed to properly simulate the high temperature data magnetic data (Figure 35); however, the shifts in energy caused by the orbital reduction factor led to much lower simulated energies for excitations (Figure 41C) as well as fits that did not model the low temperature magnetization data as accurately as the previous fits. We attribute this to the drop in the orbital reduction factor, a variable that is used to incorporate the effects of covalency and mixing of excited states into the Hamiltonian. This acts as a scaling factor on the energies of this system, and although the magnetic susceptibility is fit well, the energy diagram shows that incorporation of the orbital reduction factor on this scale in this system is inappropriate for modeling magnetic behavior. To address this, we decided to fit the orbital reduction term on the Zeeman portion of the Hamiltonian only. This limits the corrective factor of the orbital reduction term to the smallest perturbation allowing the energy manifold to be defined by the SOC and crystal field terms. This fit gives values of $\lambda = -143.4$, $\sigma = 0.92$, and a B_3^4 value of -1669 cm^{-1} allowing for a comparable fit of the magnetic data (Figure 36) while maintaining the correct excitation energies in simulations (Figure 41D). We also employed the Hamiltonian used in the previous literature report of this complex by Saber et al[125]. Using the values employed in this report gave us good fits on the magnetic data; however, the energy manifold is poorly simulated as shown in Figure 41E. When compared to our approach, it is clear this method addresses the energy problems inherent to using orbital reduction factors while simultaneously giving a consistent way of modeling the magnetic properties from crystal field values.

We repeated the same series of fits on the DMSO adduct using the spectroscopic data to find the initial crystal field value. Consistent with its weaker field, the spectroscopically-derived crystal field value for the DMSO adduct was also smaller (B_4^0 = 2176 cm^{-1}). This fit is adequate in regard to the magnitude for susceptibility and magnetization. The simulated energies of this system are on par with the spectroscopic data (Figure 42A); however, the overall fits to the data are poor. Introduction of the spin-orbit coupling term and orbital reduction terms gave best fits of $\lambda = -171.5$ and $\sigma = 0.48$ which led to much better magnetic fits, but the energies of excitations were greatly reduced by the orbital reduction factor (Figure 42B). Applying a trigonal distortion of -1130 cm^{-1} did not significantly alter the energy or other fitting values to this system (Figure 42C), but upon applying the orbital reduction to only the Zeeman portion of the Hamiltonian, quality fits were obtained with the inclusion of the trigonal distortion parameter. This fit gave values of λ = -127.7, σ = 0.76, and a trigonal distortion value of -1602 cm^{-1}. Importantly, the fit models both the magnetic data and energy spectrum effectively (Figure 42D). The drop in the spin-orbit coupling term may be explained by the distortion itself, with coupling being less effective as the distortion increases.

3.5 Conclusion

The magnetic complexity of first-row transition metals with unquenched orbital moment is arguably greater than that of the lanthanides. The near-perfect octahedral Co(II) complexes studied herein are exemplary of this complexity, with energetically important crystal-field, spin-orbit, and Coulombic interactions all shown to influence the magnetic fitting parameters. Oriented-crystal magnetometry and magnetic spectroscopies are ideal for extracting a full phenomenological model of the ground state of such systems; however, it may not be feasible to apply these methods to every system. To reduce the number of parameters, we move to a more realistic wavefunction, using d-d transition energies in the visible range to give a first approximation for the crystal field splitting parameters. This approach draws from the intuition of coordination chemistry where the electronic structure of a metal complex is often taken as roughly tetrahedral or octahedral plus some additional distortion. The systems studied herein were chosen as ideal cases to study and test various approaches based on easily attainable spectroscopic measurements and readily accessible magnetic data fitting software. Though not the first, these data provide a strong example of the danger of employing an orbital reduction factor without clearly defined restrictions. This factor should rarely be considered physically significant as it manipulates multiple Hamiltonian terms, is often highly correlated, and can be associated with multiple interpretations. While the use of spectroscopic data employed herein is rudimentary, it allows multiple independent datasets spanning a wide energy range to be used for restricting the parameter space of complex magnetic Hamiltonians. The simple nature of the data collection and fitting procedure are perhaps the most important part as they could allow the evaluation of this method with minimal alteration of current methods. Additional work to understand if this model can be expanded is currently in progress and further studies of similar compounds will be conducted to see whether other relations can be drawn from Racah parameters, crystal field terms, and magnetic behavior. Possibly, much of the remaining phenomenological nature of the fits is due to the lack of inclusion of the ^{4}P state. Future studies will attempt to corroborate the fit parameters with data from ab initio calculations as well as EPR and low-temperature spectroscopy.

The material in Chapter 3 of this dissertation is currently in preparation: Mantanona, A.J, Li, J., Gembicky, M., and Rinehart, J. D "Modeling the molecular magnetism of near-perfect octahedral Co(II) complexes with physically intuitive parameterization". The dissertation author is the primary author of this publication.

Appendix A

Definitions of the Stevens operators in terms of orbital angular momentum[17].

$$\widehat{O}_2^{-2} = \frac{-i}{2}\left(\hat{L}_+{}^2 - \hat{L}_-{}^2\right)$$

$$\widehat{O}_2^{-1} = \frac{-i}{4}\left(\hat{L}_z\left(\hat{L}_+ - \hat{L}_-\right) + \left(\hat{L}_+ - \hat{L}_-\right)\hat{L}_z\right)$$

$$\widehat{O}_2^{0} = 3\hat{L}_z{}^2 - \hat{L}^2$$

$$\widehat{O}_2^{+1} = \frac{1}{4}\left(\hat{L}_z\left(\hat{L}_+ - \hat{L}_-\right) + \left(\hat{L}_+ - \hat{L}_-\right)\hat{L}_z\right)$$

$$\widehat{O}_2^{+2} = \frac{1}{2}\left(\hat{L}_+{}^2 - \hat{L}_-{}^2\right)$$

$$\widehat{O}_4^{-4} = \frac{-i}{2}\left(\hat{L}_+{}^4 - \hat{L}_-{}^4\right)$$

$$\widehat{O}_4^{-3} = \frac{-i}{4}\left(\hat{L}_z\left(\hat{L}_+{}^3 - \hat{L}_-{}^3\right) + \left(\hat{L}_+{}^3 - \hat{L}_-{}^3\right)\hat{L}_z\right)$$

$$\widehat{O}_4^{-2} = \frac{-i}{4}\left(\left(7\hat{L}_z{}^2 - \hat{L}^2 - 5\right)\left(\hat{L}_+{}^2 - \hat{L}_-{}^2\right) + \left(\hat{L}_+{}^2 - \hat{L}_-{}^2\right)\left(7\hat{L}_z{}^2 - \hat{L}^2 - 5\right)\right)$$

$$\widehat{O}_4^{-1} = \frac{-i}{4}\left(\left(7\hat{L}_z{}^3 - 3\hat{L}^2\hat{L}_z - \hat{L}_z\right)\left(\hat{L}_+ - \hat{L}_-\right) + \left(\hat{L}_+ - \hat{L}_-\right)\left(7\hat{L}_z{}^3 - 3\hat{L}^2\hat{L}_z - \hat{L}_z\right)\right)$$

$$\widehat{O}_4^{0} = 35\hat{L}_z{}^4 - 30\hat{L}^2\hat{L}_z{}^2 + 25\hat{L}_z{}^2 + 3\hat{L}^{2\,2} - 6\hat{L}^2$$

$$\widehat{O}_4^{+1} = \frac{1}{4}\left(\left(7\hat{L}_z{}^3 - 3\hat{L}^2\hat{L}_z - \hat{L}_z\right)\left(\hat{L}_+ + \hat{L}_-\right) + \left(\hat{L}_+ + \hat{L}_-\right)\left(7\hat{L}_z{}^3 - 3\hat{L}^2\hat{L}_z - \hat{L}_z\right)\right)$$

$$\widehat{O}_4^{+2} = \frac{1}{4}\left(\left(7\hat{L}_z{}^2 - \hat{L}^2 - 5\right)\left(\hat{L}_+{}^2 + \hat{L}_-{}^2\right) + \left(\hat{L}_+{}^2 + \hat{L}_-{}^2\right)\left(7\hat{L}_z{}^2 - \hat{L}^2 - 5\right)\right)$$

$$\widehat{O}_4^{+3} = \frac{1}{4}\left(\hat{L}_z\left(\hat{L}_+{}^3 - \hat{L}_-{}^3\right) + \left(\hat{L}_+{}^3 + \hat{L}_-{}^3\right)\hat{L}_z\right)$$

$$\widehat{O}_4^{+4} = \frac{1}{2}\left(\hat{L}_+{}^4 + \hat{L}_-{}^4\right)$$

$$\widehat{O}_6^{-6} = \frac{-i}{2}\left(\hat{L}_+{}^6 - \hat{L}_-{}^6\right)$$

$$\widehat{O}_6^{-5} = \frac{-i}{4}\left(\left(\hat{L}_+{}^5 - \hat{L}_-{}^5\right)\hat{L}_z + \hat{L}_z\left(\hat{L}_+{}^5 - \hat{L}_-{}^5\right)\right)$$

$$\hat{O}_6^{-4} = \frac{-i}{4}\left(\left({\hat{L}_+}^4 - {\hat{L}_-}^4\right)\left(11{\hat{L}_z}^2 - \hat{L}^2 - 38\right) + \left(11{\hat{L}_z}^2 - \hat{L}^2 - 38\right)\left({\hat{L}_+}^4 - {\hat{L}_-}^4\right)\right)$$

$$\begin{aligned}\hat{O}_6^{-3} = \frac{-i}{4}\Big(&\left({\hat{L}_+}^3 - {\hat{L}_-}^3\right)\left(11{\hat{L}_z}^2 - 3\hat{L}^2\hat{L}_z - 59\hat{L}_z\right)\\ &+ \left(11{\hat{L}_z}^3 - 3\hat{L}^2\hat{L}_z - 59\hat{L}_z\right)\left({\hat{L}_+}^3 - {\hat{L}_-}^3\right)\Big)\end{aligned}$$

$$\begin{aligned}\hat{O}_6^{-2} = \frac{-i}{4}\Big(&\left({\hat{L}_+}^2 - {\hat{L}_-}^2\right)\left(33{\hat{L}_z}^4 - 18\hat{L}^2\hat{L}_z - 123{\hat{L}_z}^2 + {\hat{L}^2}^2 + 10\hat{L}^2 + 102\right)\\ &+ \left(33{\hat{L}_z}^4 - 18\hat{L}^2\hat{L}_z - 123{\hat{L}_z}^2 + {\hat{L}^2}^2 + 10\hat{L}^2 + 102\right)\left({\hat{L}_+}^2 - {\hat{L}_-}^2\right)\Big)\end{aligned}$$

$$\begin{aligned}\hat{O}_6^{-1} = \frac{-i}{4}\Big(&\left(\hat{L}_+ - \hat{L}_-\right)\left(33{\hat{L}_z}^5 - 30\hat{L}^2{\hat{L}_z}^3 + 15{\hat{L}_z}^3 + 5{\hat{L}^2}^2\hat{L}_z - 10\hat{L}^2\hat{L}_z + 12\hat{L}_z\right)\\ &+ \left(33{\hat{L}_z}^5 - 30\hat{L}^2{\hat{L}_z}^3 + 15{\hat{L}_z}^3 + 5{\hat{L}^2}^2\hat{L}_z - 10\hat{L}^2\hat{L}_z + 12\hat{L}_z\right)\left(\hat{L}_+ - \hat{L}_-\right)\Big)\end{aligned}$$

$$\begin{aligned}\hat{O}_6^{0} = {}& 231{\hat{L}_z}^6 - 315\hat{L}^2{\hat{L}_z}^4 + 735{\hat{L}_z}^4 + 105{\hat{L}^2}^2{\hat{L}_z}^2 - 525{\hat{L}^2}^2{\hat{L}_z}^2 + 294{\hat{L}_z}^2 - 5{\hat{L}^2}^3\\ &+ 40{\hat{L}^2}^2 - 60\hat{L}^2\end{aligned}$$

$$\begin{aligned}\hat{O}_6^{+1} = \frac{1}{4}\Big(&\left(\hat{L}_+ + \hat{L}_-\right)\left(33{\hat{L}_z}^5 - 30\hat{L}^2{\hat{L}_z}^3 + 15{\hat{L}_z}^3 + 5{\hat{L}^2}^2\hat{L}_z - 10\hat{L}^2\hat{L}_z + 12\hat{L}_z\right)\\ &+ \left(33{\hat{L}_z}^5 - 30\hat{L}^2{\hat{L}_z}^3 + 15{\hat{L}_z}^3 + 5{\hat{L}^2}^2\hat{L}_z - 10\hat{L}^2\hat{L}_z + 12\hat{L}_z\right)\left(\hat{L}_+ + \hat{L}_-\right)\Big)\end{aligned}$$

$$\begin{aligned}\hat{O}_6^{+2} = \frac{1}{4}\Big(&\left({\hat{L}_+}^2 + {\hat{L}_-}^2\right)\left(33{\hat{L}_z}^4 - 18\hat{L}^2\hat{L}_z - 123{\hat{L}_z}^2 + {\hat{L}^2}^2 + 10\hat{L}^2 + 102\right)\\ &+ \left(33{\hat{L}_z}^4 - 18\hat{L}^2\hat{L}_z - 123{\hat{L}_z}^2 + {\hat{L}^2}^2 + 10\hat{L}^2 + 102\right)\left({\hat{L}_+}^2 + {\hat{L}_-}^2\right)\Big)\end{aligned}$$

$$\begin{aligned}\hat{O}_6^{+3} = \frac{1}{4}\Big(&\left({\hat{L}_+}^3 + {\hat{L}_-}^3\right)\left(11{\hat{L}_z}^2 - 3\hat{L}^2\hat{L}_z - 59\hat{L}_z\right)\\ &+ \left(11{\hat{L}_z}^3 - 3\hat{L}^2\hat{L}_z - 59\hat{L}_z\right)\left({\hat{L}_+}^3 + {\hat{L}_-}^3\right)\Big)\end{aligned}$$

$$\hat{O}_6^{+4} = \frac{1}{4}\left(\left({\hat{L}_+}^4 + {\hat{L}_-}^4\right)\left(11{\hat{L}_z}^2 - \hat{L}^2 - 38\right) + \left(11{\hat{L}_z}^2 - \hat{L}^2 - 38\right)\left({\hat{L}_+}^4 + {\hat{L}_-}^4\right)\right)$$

$$\hat{O}_6^{+5} = \frac{1}{4}\left(\left({\hat{L}_+}^5 + {\hat{L}_-}^5\right)\hat{L}_z + \hat{L}_z\left({\hat{L}_+}^5 + {\hat{L}_-}^5\right)\right)$$

$$\hat{O}_6^{+6} = \frac{1}{2}\left({\hat{L}_+}^6 + {\hat{L}_-}^6\right)$$

References

1. Sessoli, R.; Tsai, H. L.; Schake, A. R.; Wang, S.; Vincent, J. B.; Folting, K.; Gatteschi, D.; Christou, G.; Hendrickson, D. N., High-spin molecules: [Mn12O12(O2CR)16(H2O)4]. *J. Am. Chem. Soc.* **1993,** *115* (5), 1804-1816.

2. Sessoli, R.; Gatteschi, D.; Caneschi, A.; Novak, M., Magnetic bistability in a metal-ion cluster. *Nature* **1993,** *365* (6442), 141.

3. Kahn, O., Molecular magnetism. *VCH Publishers, Inc.(USA), 1993* **1993**, 393.

4. Van Vleck, J. H., *The theory of electric and magnetic susceptibilities*. Oxford University Press: 1965.

5. Procopiu, S., Determining the Molecular Magnetic Moment by M. Planck's Quantum Theory. *Bulletin scientifique de l'Académie roumaine de sciences* **1913,** *1*, 151.

6. Heilbron, J. L.; Kuhn, T. S., The genesis of the Bohr atom. *Historical studies in the physical sciences* **1969,** *1*, vi-290.

7. Bunting, P. C., *Synthesis and Magnetic Properties of Two-Coordinate Transition Metal Complexes*. University of California, Berkeley: 2019.

8. Orchard, A. F., *Magnetochemistry*. Oxford University Press: Oxford, 2003.

9. Figures adapted from the following websites under the Creative Commons License.
https://en.wikipedia.org/wiki/File:Atomic_orbitals_n1234_m-eigenstates.png
https://en.wikipedia.org/wiki/File:D3M0.png
https://en.wikipedia.org/wiki/File:Dxz_orbital.png
https://en.wikipedia.org/wiki/File:Dyz_orbital.png
https://en.wikipedia.org/wiki/File:Dxy_orbital.png
https://en.wikipedia.org/wiki/File:Dx2-y2_orbital.png.

10. Boča, R., Zero-field splitting in metal complexes. *Coord. Chem. Rev.* **2004,** *248* (9), 757-815.

11. Gerloch, M., *Magnetism and ligand-field analysis*. CUP Archive: 1983.

12. Mulak, J.; Gajek, Z., *The effective crystal field potential*. Elsevier: 2000.

13. Newman, D.; Ng, B., The superposition model of crystal fields. *Rep. Prog. Phys.* **1989,** *52* (6), 699.

14. Schäffer, C. E.; Jørgensen, C. K., The angular overlap model, an attempt to revive the ligand field approaches. *Mol. Phys.* **1965,** *9* (5), 401-412.

15. Urland, W., On the ligand-field potential for f electrons in the angular overlap model. *Chem. Phys.* **1976,** *14* (3), 393-401.

16. Hutchings, M. T., Point-Charge Calculations of Energy Levels of Magnetic Ions in Crystalline Electric Fields**This work was supported by the U.S. Air Force, the U.K. Department of and Industrial Research, and the U.S. Atomic Energy Commission. In *Solid State Physics*, Seitz, F.; Turnbull, D., Eds. Academic Press: 1964; Vol. 16, pp 227-273.

17. Chilton, N. F.; Anderson, R. P.; Turner, L. D.; Soncini, A.; Murray, K. S., PHI: A powerful new program for the analysis of anisotropic monomeric and exchange-coupled polynuclear d-and f-block complexes. *J. Comput. Chem.* **2013,** *34* (13), 1164-1175.

18. Wybourne, B. G., Spectroscopic properties of rare earths. **1965**.

19. Stevens, K., Matrix elements and operator equivalents connected with the magnetic properties of rare earth ions. *Proceedings of the Physical Society. Section A* **1952,** *65* (3), 209.

20. Abragam, A.; Bleaney, B., *Electron paramagnetic resonance of transition ions*. Oxford University Press: 2012.

21. Edmonds, A. R., *Angular momentum in quantum mechanics*. Princeton university press: 2016.

22. Lloret, F.; Julve, M.; Cano, J.; Ruiz-García, R.; Pardo, E., Magnetic properties of six-coordinated high-spin cobalt (II) complexes: Theoretical background and its application. *Inorg. Chim. Acta* **2008,** *361* (12-13), 3432-3445.

23. Bethe, H., Termaufspaltung in kristallen. *Annalen der Physik* **1929,** *395* (2), 133-208.

24. Pauling, L., The nature of the chemical bond. Application of results obtained from the quantum mechanics and from a theory of paramagnetic susceptibility to the structure of molecules. *J. Am. Chem. Soc.* **1931,** *53* (4), 1367-1400.

25. Van Vleck, J., Theory of the variations in paramagnetic anisotropy among different salts of the iron group. *Physical Review* **1932,** *41* (2), 208.

26. Penney, W. G.; Schlapp, R., The influence of Crystalline Fields on the Susceptibilities of Salts of Paramagnetic Ions. I. The rare earths, especially Pr and Nd. *Physical Review* **1932,** *41* (2), 194.

27. Schlapp, R.; Penney, W. G., Influence of crystalline fields on the susceptibilities of salts of paramagnetic ions. II. The iron group, especially Ni, Cr and Co. *Physical Review* **1932,** *42* (5), 666.

28. Mulliken, R. S., The interpretation of band spectra part III. Electron quantum numbers and states of molecules and their atoms. *Reviews of modern physics* **1932,** *4* (1), 1.

29. Van Vleck, J., The group relation between the Mulliken and Slater-Pauling theories of valence. *The Journal of Chemical Physics* **1935,** *3* (12), 803-806.

30. Gerloch, M.; Slade, R. C., *Ligand-field parameters*. Cambridge University Press: 2009.

31. Figgis, B. N., Ligand field theory. *Comprehensive Coordination Chemistry* **1987,** *1*, 213-279.

32. Racah, G., Theory of complex spectra. II. *Physical Review* **1942,** *62* (9-10), 438.

33. Condon, E. U.; Condon, E.; Shortley, G. H., *The theory of atomic spectra*. Cambridge University Press: 1935.

34. Rechkemmer, Y., Spectroscopic investigations of the magnetic anisotropy of lanthanide- and cobalt-based molecular nanomagnets. **2016**.

35. Tanabe, Y.; Sugano, S., On the Absorption Spectra of Complex Ions II. *J. Phys. Soc. Jpn.* **1954,** *9* (5), 766-779.

36. Tanabe-Sugano Diagrams.

37. Pryce, M.; Runciman, W., The absorption spectrum of vanadium corundum. *Discussions of the Faraday Society* **1958,** *26*, 34-42.

38. Griffith, J. S., *The theory of transition-metal ions*. Cambridge University Press: 1964.

39. Yeung, Y. Y.; Rudowicz, C., Ligand field analysis of the 3dN ions at orthorhombic or higher symmetry sites. *Computers & chemistry* **1992,** *16* (3), 207-216.

40. Ballhausen, C. J., Introduction to Ligand Field Theory Mc-Graw Hill Ed. Wiley-VCH: New York: 1962.

41. Sharma, R.; Das, T.; Orbach, R., Zero-field splitting of S-state ions. I. Point-multipole model. *Physical Review* **1966,** *149* (1), 257.

42. Wan-Lun, Y.; Min-Guang, Z., Spin-Hamiltonian parameters of state 6 ions. *Physical Review B* **1988,** *37* (16), 9254.

43. Morrison, C. A., *Crystal fields for transition-metal ions in laser host materials*. Springer Science & Business Media: 2012.

44. Yang, Z.-Y.; Wei, Q., On the relations between the crystal field parameter notations in the “Wybourne” notation and the conventional ones for 3dN ions in axial symmetry crystal field. *Physica B: Condensed Matter* **2005,** *370* (1-4), 137-145.

45. Harris, D. C.; Bertolucci, M. D., *Symmetry and spectroscopy: an introduction to vibrational and electronic spectroscopy*. Courier Corporation: 1989.

46. Skomski, R., *Simple models of magnetism*. Oxford University Press on Demand: 2008.

47. Bean, C.; Livingston, u. D., Superparamagnetism. *J. Appl. Phys.* **1959,** *30* (4), S120-S129.

48. Néel, L., Théorie du traînage magnétique des ferromagnétiques en grains fins avec applications aux terres cuites. *Ann. géophys.* **1949,** *5*, 99-136.

49. Milios, C. J.; Vinslava, A.; Wernsdorfer, W.; Moggach, S.; Parsons, S.; Perlepes, S. P.; Christou, G.; Brechin, E. K., A record anisotropy barrier for a single-molecule magnet. *J. Am. Chem. Soc.* **2007,** *129* (10), 2754-2755.

50. Layfield, R. A., Organometallic single-molecule magnets. *Organometallics* **2014,** *33* (5), 1084-1099.

51. Ishikawa, N.; Sugita, M.; Ishikawa, T.; Koshihara, S.-y.; Kaizu, Y., Lanthanide Double-Decker Complexes Functioning as Magnets at the Single-Molecular Level. *J. Am. Chem. Soc.* **2003,** *125* (29), 8694-8695.

52. Rinehart, J. D.; Long, J. R., Exploiting single-ion anisotropy in the design of f-element single-molecule magnets. *Chemical Science* **2011,** *2* (11), 2078-2085.

53. Guo, F.-S.; Day, B. M.; Chen, Y.-C.; Tong, M.-L.; Mansikkamäki, A.; Layfield, R. A., Magnetic hysteresis up to 80 kelvin in a dysprosium metallocene single-molecule magnet. *Science* **2018,** *362* (6421), 1400-1403.

54. Goodwin, C. A.; Ortu, F.; Reta, D.; Chilton, N. F.; Mills, D. P., Molecular magnetic hysteresis at 60 kelvin in dysprosocenium. *Nature* **2017,** *548* (7668), 439-442.

55. Guo, F. S.; Day, B. M.; Chen, Y. C.; Tong, M. L.; Mansikkamäki, A.; Layfield, R. A., A dysprosium metallocene single-molecule magnet functioning at the axial limit. *Angew. Chem.* **2017,** *129* (38), 11603-11607.

56. Gomez-Coca, S.; Cremades, E.; Aliaga-Alcalde, N.; Ruiz, E., Mononuclear single-molecule magnets: tailoring the magnetic anisotropy of first-row transition-metal complexes. *J. Am. Chem. Soc.* **2013,** *135* (18), 7010-7018.

57. Zadrozny, J. M.; Xiao, D. J.; Atanasov, M.; Long, G. J.; Grandjean, F.; Neese, F.; Long, J. R., Magnetic blocking in a linear iron (I) complex. *Nature chemistry* **2013,** *5* (7), 577.

58. Yao, X.-N.; Du, J.-Z.; Zhang, Y.-Q.; Leng, X.-B.; Yang, M.-W.; Jiang, S.-D.; Wang, Z.-X.; Ouyang, Z.-W.; Deng, L.; Wang, B.-W.; Gao, S., Two-Coordinate Co(II) Imido Complexes as Outstanding Single-Molecule Magnets. *J. Am. Chem. Soc.* **2017,** *139* (1), 373-380.

59. Bunting, P. C.; Atanasov, M.; Damgaard-Møller, E.; Perfetti, M.; Crassee, I.; Orlita, M.; Overgaard, J.; van Slageren, J.; Neese, F.; Long, J. R., A linear cobalt (II) complex with maximal orbital angular momentum from a non-Aufbau ground state. *Science* **2018,** *362* (6421), eaat7319.

60. Dhers, S.; Feltham, H. L. C.; Brooker, S., A toolbox of building blocks, linkers and crystallisation methods used to generate single-chain magnets. *Coord. Chem. Rev.* **2015,** *296*, 24-44.

61. Sun, H.-L.; Wang, Z.-M.; Gao, S., Strategies towards single-chain magnets. *Coord. Chem. Rev.* **2010,** *254* (9), 1081-1100.

62. Caneschi, A.; Gatteschi, D.; Lalioti, N.; Sangregorio, C.; Sessoli, R.; Venturi, G.; Vindigni, A.; Rettori, A.; Pini, M. G.; Novak, M. A., Cobalt (II)-nitronyl nitroxide chains as molecular magnetic nanowires. *Angew. Chem. Int. Ed.* **2001,** *40* (9), 1760-1763.

63. Crabtree, R. H., *The organometallic chemistry of the transition metals*. John Wiley & Sons: 2009.

64. Hopkinson, M. N.; Richter, C.; Schedler, M.; Glorius, F., An overview of N-heterocyclic carbenes. *Nature* **2014,** *510* (7506), 485.

65. Melaimi, M.; Jazzar, R.; Soleilhavoup, M.; Bertrand, G., Cyclic (Alkyl)(amino)carbenes (CAACs): Recent Developments. *Angew. Chem. Int. Ed.* **2017,** *56* (34), 10046-10068.

66. Crabtree, R. H., Abnormal, mesoionic and remote N-heterocyclic carbene complexes. *Coord. Chem. Rev.* **2013,** *257* (3-4), 755-766.

67. Guisado-Barrios, G.; Soleilhavoup, M.; Bertrand, G., 1H-1,2,3-Triazol-5-ylidenes: Readily Available Mesoionic Carbenes. *Acc. Chem. Res.* **2018,** *51* (12), 3236-3244.

68. Vivancos, A. n.; Segarra, C.; Albrecht, M., Mesoionic and related less heteroatom-stabilized N-heterocyclic carbene complexes: synthesis, catalysis, and other applications. *Chem. Rev.* **2018,** *118* (19), 9493-9586.

69. Schweinfurth, D.; Hettmanczyk, L.; Suntrup, L.; Sarkar, B., Metal Complexes of Click-Derived Triazoles and Mesoionic Carbenes: Electron Transfer, Photochemistry, Magnetic Bistability, and Catalysis. *Z. Anorg. Allg. Chem.* **2017,** *643* (9), 554-584.

70. Andrada, D. M.; Holzmann, N.; Hamadi, T.; Frenking, G., Direct estimate of the internal π-donation to the carbene centre within N-heterocyclic carbenes and related molecules. *Beilstein journal of organic chemistry* **2015,** *11* (1), 2727-2736.

71. Murrie, M., Cobalt (II) single-molecule magnets. *Chem. Soc. Rev.* **2010,** *39* (6), 1986-1995.

72. Bianchini, C.; Mantovani, G.; Meli, A.; Migliacci, F.; Laschi, F., Selective Oligomerization of Ethylene to Linear α-Olefins by Tetrahedral Cobalt(II) Complexes with 6-(Organyl)-2-

(imino)pyridyl Ligands: Influence of the Heteroatom in the Organyl Group on the Catalytic Activity. *Organometallics* **2003,** *22* (13), 2545-2547.

73. van der Meer, M.; Rechkemmer, Y.; Peremykin, I.; Hohloch, S.; van Slageren, J.; Sarkar, B., (Electro)catalytic C–C bond formation reaction with a redox-active cobalt complex. *Chem. Commun.* **2014,** *50* (76), 11104-11106.

74. Fataftah, M. S.; Coste, S. C.; Vlaisavljevich, B.; Zadrozny, J. M.; Freedman, D. E., Transformation of the coordination complex [Co(C3S5)2]2− from a molecular magnet to a potential qubit. *Chemical Science* **2016,** *7* (9), 6160-6166.

75. Sieklucka, B.; Pinkowicz, D., *Molecular magnetic materials: concepts and applications*. John Wiley & Sons: 2017.

76. Rechkemmer, Y.; Breitgoff, F. D.; Van Der Meer, M.; Atanasov, M.; Hakl, M.; Orlita, M.; Neugebauer, P.; Neese, F.; Sarkar, B.; Van Slageren, J., A four-coordinate cobalt (II) single-ion magnet with coercivity and a very high energy barrier. *Nature communications* **2016,** *7*, 10467.

77. Fataftah, M. S.; Zadrozny, J. M.; Rogers, D. M.; Freedman, D. E., A mononuclear transition metal single-molecule magnet in a nuclear spin-free ligand environment. *Inorg. Chem.* **2014,** *53* (19), 10716-10721.

78. Zadrozny, J. M.; Telser, J.; Long, J. R., Slow magnetic relaxation in the tetrahedral cobalt(II) complexes [Co(EPh)4]2− (EO, S, Se). *Polyhedron* **2013,** *64*, 209-217.

79. Saber, M. R.; Dunbar, K. R., Ligands effects on the magnetic anisotropy of tetrahedral cobalt complexes. *Chem. Commun.* **2014,** *50* (82), 12266-12269.

80. Šebová, M.; Jorík, V.; Moncoľ, J.; Kožíšek, J.; Boča, R., Structure and magnetism of Co (II) complexes with bidentate heterocyclic ligand Hsalbim derived from benzimidazole. *Polyhedron* **2011,** *30* (6), 1163-1170.

81. Gómez-Coca, S.; Urtizberea, A.; Cremades, E.; Alonso, P. J.; Camón, A.; Ruiz, E.; Luis, F., Origin of slow magnetic relaxation in Kramers ions with non-uniaxial anisotropy. *Nature communications* **2014,** *5*, 4300.

82. Carl, E.; Demeshko, S.; Meyer, F.; Stalke, D., Triimidosulfonates as Acute Bite-Angle Chelates: Slow Relaxation of the Magnetization in Zero Field and Hysteresis Loop of a CoII Complex. *Chemistry–A European Journal* **2015,** *21* (28), 10109-10115.

83. van der Meer, M.; Glais, E.; Siewert, I.; Sarkar, B., Electrocatalytic dihydrogen production with a robust mesoionic pyridylcarbene cobalt catalyst. *Angew. Chem. Int. Ed.* **2015,** *54* (46), 13792-13795.

84. Meng, Y.-S.; Mo, Z.; Wang, B.-W.; Zhang, Y.-Q.; Deng, L.; Gao, S., Observation of the single-ion magnet behavior of d8 ions on two-coordinate Co(i)–NHC complexes. *Chemical Science* **2015,** *6* (12), 7156-7162.

85. Poulten, R. C.; Page, M. J.; Algarra, A. G.; Le Roy, J. J.; López, I.; Carter, E.; Llobet, A.; Macgregor, S. A.; Mahon, M. F.; Murphy, D. M.; Murugesu, M.; Whittlesey, M. K., Synthesis, Electronic Structure, and Magnetism of [Ni(6-Mes)2]+: A Two-Coordinate Nickel(I) Complex Stabilized by Bulky N-Heterocyclic Carbenes. *J. Am. Chem. Soc.* **2013,** *135* (37), 13640-13643.

86. Mondal, K. C.; Samuel, P. P.; Roesky, H. W.; Carl, E.; Herbst-Irmer, R.; Stalke, D.; Schwederski, B.; Kaim, W.; Ungur, L.; Chibotaru, L. F.; Hermann, M.; Frenking, G., Stabilization of a Cobalt–Cobalt Bond by Two Cyclic Alkyl Amino Carbenes. *J. Am. Chem. Soc.* **2014,** *136* (5), 1770-1773.

87. Samuel, P. P.; Mondal, K. C.; Amin Sk, N.; Roesky, H. W.; Carl, E.; Neufeld, R.; Stalke, D.; Demeshko, S.; Meyer, F.; Ungur, L.; Chibotaru, L. F.; Christian, J.; Ramachandran, V.; van Tol, J.; Dalal, N. S., Electronic Structure and Slow Magnetic Relaxation of Low-Coordinate Cyclic Alkyl(amino) Carbene Stabilized Iron(I) Complexes. *J. Am. Chem. Soc.* **2014,** *136* (34), 11964-11971.

88. Samuel, P. P.; Mondal, K. C.; Roesky, H. W.; Hermann, M.; Frenking, G.; Demeshko, S.; Meyer, F.; Stückl, A. C.; Christian, J. H.; Dalal, N. S., Synthesis and Characterization of a Two-Coordinate Manganese Complex and its Reaction with Molecular Hydrogen at Room Temperature. *Angew. Chem. Int. Ed.* **2013,** *52* (45), 11817-11821.

89. Samuel, P. P.; Neufeld, R.; Chandra Mondal, K.; Roesky, H. W.; Herbst-Irmer, R.; Stalke, D.; Demeshko, S.; Meyer, F.; Rojisha, V. C.; De, S.; Parameswaran, P.; Stückl, A. C.; Kaim, W.; Christian, J. H.; Bindra, J. K.; Dalal, N. S., Cr(i)Cl as well as Cr+ are stabilised between two cyclic alkyl amino carbenes. *Chemical Science* **2015,** *6* (5), 3148-3153.

90. Chakraborty, U.; Demeshko, S.; Meyer, F.; Rebreyend, C.; de Bruin, B.; Atanasov, M.; Neese, F.; Mühldorf, B.; Wolf, R., Electronic Structure and Magnetic Anisotropy of an Unsaturated Cyclopentadienyl Iron (I) Complex with 15 Valence Electrons. *Angew. Chem. Int. Ed.* **2017,** *56* (27), 7995-7999.

91. Massard, A.; Braunstein, P.; Danopoulos, A. A.; Choua, S.; Rabu, P., Studies on Three-Coordinate [Co{N(SiMe3)2}2L] Complexes, L = N-Heterocyclic Carbene. *Organometallics* **2015,** *34* (11), 2429-2438.

92. Pangborn, A. B.; Giardello, M. A.; Grubbs, R. H.; Rosen, R. K.; Timmers, F. J., Safe and Convenient Procedure for Solvent Purification. *Organometallics* **1996,** *15* (5), 1518-1520.

93. Dolomanov, O. V.; Bourhis, L. J.; Gildea, R. J.; Howard, J. A. K.; Puschmann, H., OLEX2: a complete structure solution, refinement and analysis program. *J. Appl. Crystallogr.* **2009,** *42* (2), 339-341.

94. Sheldrick, G., SHELXT - Integrated space-group and crystal-structure determination. *Acta Crystallographica Section A* **2015,** *71* (1), 3-8.

95. Sheldrick, G., Crystal structure refinement with SHELXL. *Acta Crystallographica Section C* **2015,** *71* (1), 3-8.

96. Bain, G. A.; Berry, J. F., Diamagnetic corrections and Pascal's constants. *J. Chem. Educ.* **2008,** *85* (4), 532.

97. Bouffard, J.; Keitz, B. K.; Tonner, R.; Guisado-Barrios, G.; Frenking, G.; Grubbs, R. H.; Bertrand, G., Synthesis of highly sTable 1, 3-diaryl-1 H-1, 2, 3-triazol-5-ylidenes and their applications in ruthenium-catalyzed olefin metathesis. *Organometallics* **2011,** *30* (9), 2617-2627.

98. Iannuzzi, T. E.; Gao, Y.; Baker, T. M.; Deng, L.; Neidig, M. L., Magnetic circular dichroism and density functional theory studies of electronic structure and bonding in cobalt(ii)–N-heterocyclic carbene complexes. *Dalton Transactions* **2017,** *46* (39), 13290-13299.

99. Przyojski, J. A.; Arman, H. D.; Tonzetich, Z. J., NHC Complexes of Cobalt(II) Relevant to Catalytic C–C Coupling Reactions. *Organometallics* **2013,** *32* (3), 723-732.

100. Reineke, M. H.; Sampson, M. D.; Rheingold, A. L.; Kubiak, C. P., Synthesis and structural studies of nickel (0) tetracarbene complexes with the introduction of a new four-coordinate geometric index, τδ. *Inorg. Chem.* **2015,** *54* (7), 3211-3217.

101. Suturina, E. A.; Maganas, D.; Bill, E.; Atanasov, M.; Neese, F., Magneto-structural correlations in a series of pseudotetrahedral [CoII (XR) 4] 2–single molecule magnets: An ab initio ligand field study. *Inorg. Chem.* **2015,** *54* (20), 9948-9961.

102. Ghadwal, R. S.; Lamm, J.-H.; Rottschäfer, D.; Schürmann, C. J.; Demeshko, S., Facile routes to abnormal-NHC-cobalt(ii) complexes. *Dalton Transactions* **2017,** *46* (24), 7664-7667.

103. Krzystek, J.; Zvyagin, S. A.; Ozarowski, A.; Fiedler, A. T.; Brunold, T. C.; Telser, J., Definitive Spectroscopic Determination of Zero-Field Splitting in High-Spin Cobalt(II). *J. Am. Chem. Soc.* **2004,** *126* (7), 2148-2155.

104. Kato, H.; Akimoto, K., Magnetic circular dichroism spectra of some tetrahedral cobalt (II) complexes. *J. Am. Chem. Soc.* **1974,** *96* (5), 1351-1357.

105. Lever, A. B. P., Electronic spectra of some transition metal complexes: Derivation of Dq and B. *J. Chem. Educ.* **1968,** *45* (11), 711.

106. Simo, C.; Holt, S., Polarized spectrum of dichlorobis (triphenylphosphine) cobalt (II). *Inorg. Chem.* **1968,** *7* (12), 2655-2657.

107. Zein, S.; Duboc, C.; Lubitz, W.; Neese, F., A systematic density functional study of the zero-field splitting in Mn (II) coordination compounds. *Inorg. Chem.* **2008,** *47* (1), 134-142.

108. Ye, S.; Neese, F., How Do Heavier Halide Ligands Affect the Signs and Magnitudes of the Zero-Field Splittings in Halogenonickel(II) Scorpionate Complexes? A Theoretical Investigation Coupled to Ligand-Field Analysis. *Journal of Chemical Theory and Computation* **2012,** *8* (7), 2344-2351.

109. Karunadasa, H. I.; Arquero, K. D.; Berben, L. A.; Long, J. R., Enhancing the Magnetic Anisotropy of Cyano-Ligated Chromium (II) and Chromium (III) Complexes via Heavy Halide Ligand Effects. *Inorg. Chem.* **2010,** *49* (11), 4738-4740.

110. Brazzolotto, D.; Gennari, M.; Yu, S.; Pécaut, J.; Rouzières, M.; Clérac, R.; Orio, M.; Duboc, C., An experimental and theoretical investigation on pentacoordinated cobalt (III) complexes with an intermediate S= 1 spin state: how halide ligands affect their magnetic anisotropy. *Chemistry–A European Journal* **2016,** *22* (3), 925-933.

111. Smolko, L.; Černák, J.; Kuchár, J.; Rajnák, C.; Titiš, J.; Boča, R., Field-Induced Slow Magnetic Relaxation in Mononuclear Tetracoordinate Cobalt (II) Complexes Containing a Neocuproine Ligand. *Eur. J. Inorg. Chem.* **2017,** *2017* (24), 3080-3086.

112. Vaidya, S.; Singh, S. K.; Shukla, P.; Ansari, K.; Rajaraman, G.; Shanmugam, M., Role of Halide Ions in the Nature of the Magnetic Anisotropy in Tetrahedral CoII Complexes. *Chemistry–A European Journal* **2017,** *23* (40), 9546-9559.

113. Korchagin, D. V.; Shilov, G. V.; Aldoshin, S. M.; Morgunov, R. B.; Talantsev, A. D.; Yureva, E. A., Halogen atom effect on the magnetic anisotropy of pseudotetrahedral Co (II) complexes with a quinoline ligand. *Polyhedron* **2015,** *102*, 147-151.

114. Liu, J.-J.; Meng, Y.-S.; Hlavička, I.; Orlita, M.; Jiang, S.-D.; Wang, B.-W.; Gao, S., Determination of zero-field splitting in Co2+ halide complexes with magnetic and far-IR measurements. *Dalton Transactions* **2017,** *46* (23), 7408-7411.

115. Mondal, A. K.; Sundararajan, M.; Konar, S., A new series of tetrahedral Co (ii) complexes [CoLX 2](X= NCS, Cl, Br, I) manifesting single-ion magnet features. *Dalton Transactions* **2018,** *47* (11), 3745-3754.

116. Bone, A. N.; Widener, C. N.; Moseley, D. H.; Liu, Z.; Lu, Z.; Cheng, Y.; Daemen, L. L.; Ozerov, M.; Telser, J.; Thirunavukkuarasu, K., Applying Unconventional Spectroscopies to the Single-Molecule Magnets, Co (PPh3) 2X2 (X= Cl, Br, I): Unveiling Magnetic Transitions and Spin-Phonon Coupling. *Chemistry–A European Journal* **2021,** *27* (43), 11110-11125.

117. Bar, A. K.; Pichon, C.; Sutter, J.-P., Magnetic anisotropy in two- to eight-coordinated transition–metal complexes: Recent developments in molecular magnetism. *Coord. Chem. Rev.* **2016,** *308*, 346-380.

118. Benelli, C.; Gatteschi, D., *Introduction to molecular magnetism: From transition metals to lanthanides*. John Wiley & Sons: 2015.

119. Rudowicz, C.; Karbowiak, M., Disentangling intricate web of interrelated notions at the interface between the physical (crystal field) Hamiltonians and the effective (spin) Hamiltonians. *Coord. Chem. Rev.* **2015,** *287*, 28-63.

120. Figgis, B. N.; Hitchman, M. A., Ligand field theory and its applications. **1999**.

121. Figgis, B. N.; Gerloch, M.; Lewis, J.; Mabbs, F. E.; Webb, G. A., The magnetic behaviour of cubic-field 4 T 1g terms in lower symmetry. *Journal of the Chemical Society A: Inorganic, Physical, Theoretical* **1968**, 2086-2093.

122. Lines, M. E., Magnetic Properties of Co Cl 2 and Ni Cl 2. *Physical Review* **1963,** *131* (2), 546.

123. Sakiyama, H.; Sudo, R.; Abiko, T.; Yoshioka, D.; Mitsuhashi, R.; Omote, M.; Mikuriya, M.; Yoshitake, M.; Koikawa, M., Magneto-structural correlation of hexakis-dmso cobalt (II) complex. *Dalton Transactions* **2017,** *46* (46), 16306-16314.

124. Heintz, R. A.; Smith, J. A.; Szalay, P. S.; Weisgerber, A.; Dunbar, K. R., *Useful Reagents and Ligands*. Wiley: 2002; Vol. 33, p 75-107.

125. Saber, M. R.; Singh, M. K.; Dunbar, K. R., Geometrical control of the magnetic anisotropy in six coordinate cobalt complexes. *Chem. Commun.* **2020,** *56* (60), 8492-8495.

126. SUDO, R.; YOSHIOKA, D.; MIKURIYA, M.; SAKIYAMA, H., Structural Feature of a Hexa-DMSO Cobalt (II) Complex: Pseudo-S6 Symmetry and Pseudo-C2v Deformation. *X-ray Structure Analysis Online* **2012,** *28*, 71-72.

127. Cirera, J.; Ruiz, E.; Alvarez, S., Shape and Spin State in Four-Coordinate Transition-Metal Complexes: The Case of the d6 Configuration. *Chemistry–A European Journal* **2006,** *12* (11), 3162-3167.

128. Casanova, D.; Cirera, J.; Llunell, M.; Alemany, P.; Avnir, D.; Alvarez, S., Minimal distortion pathways in polyhedral rearrangements. *J. Am. Chem. Soc.* **2004,** *126* (6), 1755-1763.

129. Pinsky, M.; Avnir, D., Continuous symmetry measures. 5. The classical polyhedra. *Inorg. Chem.* **1998,** *37* (21), 5575-5582.

130. Banci, L.; Bencini, A.; Benelli, C.; Gatteschi, D.; Zanchini, C., Spectral-structural correlations in high-spin cobalt (II) complexes. In *Structures versus Special Properties*, Springer: 1982; pp 37-86.